UNIVERSITÀ DEGLI STUDI DI PADOVA
FACOLTA' DI INGEGNERIA
DIPARTIMENTO DI PRINCIPI E IMPIANTI DI
INGEGNERIA CHIMICA "I. SORGATO"

ÅBO AKADEMI UNIVERSITY
DIVISION FOR NATURAL SCIENCES AND TECHNOLOGY
DEPARTMENT OF CHEMICAL ENGINEERING

TESI DI LAUREA MAGISTRALE IN
INGEGNERIA CHIMICA E DEI PROCESSI INDUSTRIALI

MODELING OF A TRICKLE-BED REACTOR FOR L-ARABINOSE HYDROGENATION

Relatore: Ch.mo prof. Paolo Canu

Correlatore: Professor Tapio Salmi

Laureando: Davide Durante

Anno Accademico 2010-2011

Riassunto

Il presente lavoro di Tesi è stato svolto presso le strutture del Laboratorio di Chimica Industriale e Ingegneria delle Reazioni Chimiche, Dipartimento di Ingegneria Chimica - Åbo Akademi (FI). Gli obiettivi possono essere così riassunti:

- sviluppo di modelli matematici da risolvere numericamente per la simulazione di un reattore trickle-bed di laboratorio, con particolare attenzione alla descrizione dei vari stadi di trasporto interfase delle specie chimiche coinvolte;
- sviluppo di codici per la risoluzione numerica dei modelli, applicando il Metodo delle Linee (Schiesser, 1991);
- conduzione di analisi di sensitività sui modelli, per indagare le prestazioni del reattore in diverse condizioni operative; la reazione modello considerata è l'idrogenazione catalitica del monosaccaride L-arabinosio a L-arabitolo;
- comparazione delle predizioni di uno dei modelli sviluppati con dati sperimentali relativi alla reazione di idrogenazione di L-arabinosio condotta in un reattore trickle-bed di laboratorio.

Dalle simulazioni si è osservato che il trasporto di specie chimica interfase gas-liquido limita significativamente la prestazione del reattore, cosiccome il trasporto diffusivo all'interno delle particelle di catalizzatore, se queste hanno dimensioni caratteristiche maggiori od uguali ad 1 mm. La diluizione del letto catalitico con inerti da 200-250 μm garantisce una buona bagnatura del letto catalitico e limitato backmixing in fase liquida.

Sperimentalmente si è osservato che il catalizzatore è soggetto a disattivazione, aspetto che ha richiesto di modellare questo fenomeno inserendolo nel modello di reattore.

Indagini sperimentali più approfondite sono necessarie per la quantificazione accurata dei coefficienti di mass-transfer nel trickle-bed reactor, dato il forte grado di disaccordo riscontrato dalle correlazioni di letteratura.

Summary

Introduction

The objectives of this work of Thesis can be resumed in 3 main points:

- develop mathematical models for the description and simulation of a small-scale laboratory trickle-bed reactor, focusing on the description of several mass transfer steps;
- perform numerical simulations of the reactor, assessing the performance of the reactor in the catalytic hydrogenation of L-arabinose to L-arabitol;
- try to compare model predictions with available experimental results from L-arabinose hydrogenation reaction.

Trickle-bed reactors (TBR) are considered the most widely used three-phase reactors in industrial practice (Al Dahhan et al. (1997), Sie and Krishna (1998)) with applications in the refining, petrochemical and chemical industries. They consist in a fixed bed of particles through which gas and liquid phases flow downward cocurrently; what make them complicated to operate and model is the strong interaction between hydrodynamics, mass transfer and kinetics. Moreover, several flow regimes are also possible, depending on liquid, gas flowrates, size of particles, physical properties of liquid and gas and pressure. These are commonly classified in low and high interaction regimes.

Small-scale TBR are useful to generate kinetic data, to evaluate alternative feedstocks for an already developed process and test newer catalyst with sensible economic advantages. Scaling down problems such as incomplete wetting of the catalyst, deviations from plug flow, channelling and enhanced backmixing in liquid phase, that undermine the meaningfulness of experimental data, can be prevented by means of catalyst dilution with nonporous, inert fines. These fines limit hydrodynamics drawbacks, while catalytic phenomena are still governed by the catalyst particles of same size and shape as used in commercial units.

Reaction model considered was the catalytic hydrogenation of the monosaccharide L-arabinose to the corresponding sugar alcohol L-arabitol, using as catalyst ruthenium on activated carbon, a process studied in the Laboratory of Industrial Chemistry and Reaction Engineering of Åbo Akademi University (FI). Typical operation conditions for this reaction are pressure up to 60 bar and moderate temperatures, around 100°C.

The system we decided to model and study is a small-scale laboratory TBR of i.d. 10mm, mass of catalyst used less than 1g, with a bulk density of 0.4 g/cm^3, catalyst both of commercial size, 1mm of equivalent diameter, and crushed, while silicon carbide inert fines used to dilute the bed have an average size of 200-250 μm. Liquid superficial velocity was varied in the range 0.01-0.1cm/s, gas velocity between 1 and 10cm/s.

Several reactor models were considered, taking into account axial dispersion, gas-liquid and liquid-solid mass transfer, internal mass transfer, catalyst deactivation and heat effects. The numerical Method of Lines was used to solve reactor models in *MatLab* 7.1.

Capitolo 1

Panoramica sui reattori a tre fasi

In questo capitolo si descrivono brevemente le principali caratteristiche dei più diffusi reattori a tre fasi, gas-liquido-solido, in uso nell'ambito della ricerca e dell'industria. Essi possono essere classificati in due famiglie: reattori "slurry" con catalizzatore solido in movimento e reattori a letto catalitico fisso (Gianetto and Silveston, 1986; Ramachandran and Chaudhari, 1983; Shah, 1979).

Il reattore "slurry" agitato e il reattore trickle-bed sono descritti con maggiore dettaglio: nel primo la fase continua che può occupare fino all'80% del volume del reattore è il liquido, nel quale il catalizzatore è mantenuto in sospensione mediante agitazione meccanica; può operare in modalità semibatch o continua. Vantaggi di questa configurazione di reattore sono l'elevata inerzia termica assicurata dall'elevato hold-up liquido, scambio di materia ed energia efficaci grazie all'agitazione meccanica, possibilità di utilizzo di particelle catalitiche fini con conseguente minore influenza del mass transfer intraparticellare sulla cinetica. Gli svantaggi sono dovuti alla necessità di separare mediante filtrazione il catalizzatore dalla fase liquida in uscita, consumi energetici elevati a causa dell'agitazione, possibili reazioni parassite nella fase liquida, dato il significativo hold-up, elevato backmixing.

Il reattore trickle-bed è un reattore a letto catalitico fisso, in cui liquido e gas fluiscono in equicorrente verso il basso. Diversi regimi idrodinamici sono possibili, a seconda delle velocità di gas, liquido, caratteristiche del letto e proprietà fisiche dei fluidi. In regime di *trickle flow* la fase gas è continua, mentre il liquido scorre sottoforma di gocce o film sottili che lambiscono le particelle. L'assenza di parti meccaniche in movimento, la maggiore quantità di catalizzatore utilizzabile rispetto allo slurry, l'assenza di flooding sono tipici vantaggi di questa configurazione. Bagnatura incompleta del catalizzatore, difficile controllo della temperatura per il ridotto hold-up liquido e limitazioni da mass transfer interno a causa della maggiori dimensioni delle particelle cataliche, sono alcuni degli svantaggi.

Chapter 1

Overview of three-phase reactors

In this chapter, a brief review of the most important three-phase reactors used in research and in industry is presented. These reactors can be mainly classified in two categories: slurry reactors with moving solid catalyst and fixed bed reactors with a fixed bed of catalyst (Gianetto and Silveston, 1986; Ramachandran and Chaudhari, 1983; Shah, 1979). The following brief review focuses only on three-phase reactors, in which the solid phase is a catalyst. In Tab. 1 an overview of some important industrial three-phase processes is reported (Salmi et al., 2010).

1.1 Slurry reactors

In three-phase slurry reactors (Fig. 1), the catalyst particles are suspended either by mechanical stirring, by the turbulence created by the upcoming gas-phase or by the dragging effect of the upcoming liquid phase. Depending on the different modality of suspension of the particles, these reactors can be divided in three main typologies: mechanically agitated slurry reactors, bubble column slurry reactors and fluidized-bed three-phase reactors (Ramachandran and Chaudhari, 1983).

1.1.1 Mechanically agitated slurry reactors

In a mechanically agitated slurry reactor, the liquid is the continuous phase continuously agitated by a mechanical stirrer, while the gas is blown from the bottom through a gas distributor and bubbles through the liquid. Typical values of liquid hold-up are around 0.8 (Gianetto and Silveston, 1986). Catalyst particles are kept suspended by means of mechanical stirring and turbulence created by the gas bubbles. Catalyst loading is low and the particle size is around 0.1 mm (Gianetto and Silveston, 1986). Slurry reactors can operate both in a semibatch mode, where the liquid is a stationary phase while the gas flows continuously through the reactor, or in a continuous mode. The height-to-diameter ratio is low. Typical advantages of mechanical stirred slurry reactors are the following:

Tab. 1. Three-phase processes and reactor types (adapted from Salmi et al., 2010).

process	reactor type
Hydrogenation of fatty acids	Bubble column and stirred tank reactor
Hydrodesulfurization	Trickle bed or fluidized bed
Hydrocracking	Trickle bed
Fischer-Tropsch synthesis	Bubble column reactor
Hydrogenation of aromatic compounds	Trickle bed and slurry reactor
Methanol syntesis	Slurry reactor
Hydrogenation of sugars to sugar alcohols	Slurry reactor, trickle bed reactor, monolithic reactor

- large heat capacity due to the presence of high liquid hold-up, that ensures an easier temperature control and accordingly a higher selectivity and longer catalyst life;
- generally faster mass and heat transfer rates, since smaller particles are used compared to fixed bed reactors;
- intraparticle mass transfer is more effective due to the smaller size of particles, leading to higher rate of reaction per unit weight (or surface) of catalyst than fixed bed reactors;
- possibility of handling viscous fluids, while still ensuring high mass and heat transfer rates, since these could be enhanced by means of mechanical agitation.

They present the following disadvantages:

- catalyst separation from the liquid phase can be difficult (it requires the use of filters) and this can lead to significant catalyst losses and pollution of the product;
- higher energy consumption than fixed bed due to mechanical stirring;
- sealing problems may arise in pressurized operations since external stirring devices are present;
- low catalyst loading involves lower reaction rate per unit volume of reactor, if the reactor operates in the chemical regime;
- high liquid hold up may lead to homogenous side reactions, if these are possible;
- high backmixing of the liquid phase generally reduces the reactor performance.

1.1.2 Bubble column slurry reactors

In these reactors the feeding modes of the gas and liquid phases are similar to the previous ones. The catalyst particles are kept suspended only by the turbulence created by the raising gas bubbles, hence the shear between the two phases is less than that in the stirred reactor. Particles are approximately of the same size as mentioned before; they differ from the particles in agitated slurry

since mass and heat transfer are less efficient (mixing is less intensive) and because they usually operate in a continuous mode. Values of the liquid hold-up are approximately the same.
Bubble column reactors have higher height-to-diameter ratio than the agitated slurry reactors.

1.1.3 Fluidized-bed three phase reactors

Liquid is still the continuous phase and gas rises in bubbles from the bottom. The ratio of the gas-to-liquid flowrates in these reactors is lower than in the previous typology. The higher liquid throughput is the main responsible factor for the suspension of catalyst particles, which are normally larger than mentioned before. The superficial velocity of the liquid must be lower than particle settling velocity, to avoid catalyst losses. Their hydrodynamics and mass transfer rates are similar to that of the bubble column.

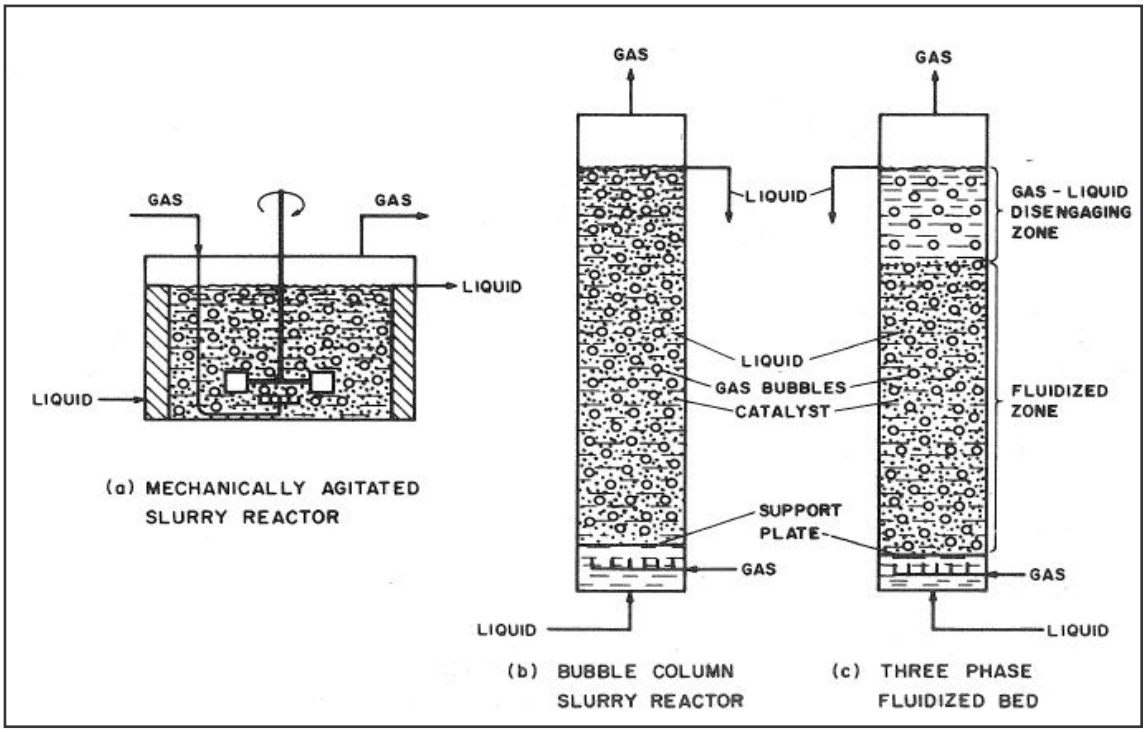

Fig. 1. Three-phase slurry reactors (Ramachandran and Chaudhari, 1983).

1.2 Fixed bed reactors

In three-phase fixed bed reactors (Fig. 2), the catalyst particles are stationary and their size is larger, ranging from 1-5 mm in pilot plant units or of a few cm in industrial reactors. The main differences among fixed bed reactors arise from the different location of the liquid and gas feeding. We can classify them to trickle bed reactors, submerged packed bed reactors (or packed bubble-bed reactors) and packed beds with countercurrent flow of liquid and gas.

1.2.1 Trickle bed reactors

In these reactors, the liquid and gas phases flow downward cocurrently. Different hydrodynamics regimes are possible, depending mainly on the values of gas and liquid flowrates, and they strongly influence the reactor performances. For low values of both flowrates, the gas is the continuous phase, while the liquid flows in form of droplets, rivulets or thin film; this flow regime is called the *trickling flow regime*. Pockets of stagnant liquid also form among particles. In pilot plants 0.01-0.3 cm/s is a typical range for the liquid superficial velocity u_L, while the gas velocity u_G is about 2 orders of magnitude higher (Ramachandran and Chaudhari, 1983).

Typical advantages of trickle-bed reactors are:

- absence of mechanical moving parts, which implies less expensive construction, maintenance and possibility to work at high pressure without sealing problems;
- low pressure drop compared to the packed bubble-bed reactor;
- low liquid hold-up, typically around 0.2 (Gianetto and Silveston, 1986), that implies less risk of homogenous reactions to occur;
- high catalyst loading, which involves higher reaction rate per unit volume of reactor, if the reactor operates in kinetic regime;
- ease to operate continuously, without the need to separate catalyst from liquid phase at the outflow.

The main disadvantages are:

- partial wetting of the catalyst surface could lead to hot spots and temperature run away if the reaction is strongly exothermic;
- temperature control and heat transfer are less effective than in slurry or packed bubble-bed reactors, due to the low liquid hold up;
- lower catalyst effectiveness factor, since particles are larger than in slurry reactors and thus intraparticle mass transfer resistances become important;
- difficult operations if the reaction network leads to significant deposition of non-volatile by-products which can obstruct the fixed bed, increasing pressure drop and requiring a frequent extraction and regeneration of the catalyst.

1.2.2 Packed bubble-bed reactors

In these kind of fixed bed reactors, also called *submerged fixed bed reactors*, liquid and gas flow upward cocurrently. The liquid is the continuous phase and the catalyst is completely wetted. The gas raises in form of bubbles. The particle diameter range is the same as for the trickle bed reactors; heat transfer and temperature control is more effective owing to the better mixing and the larger

liquid hold-up (around 0.4 (Gianetto and Silveston, 1986)). The pressure drop is higher than in downflow operation as well as the degree of backmixing, that generally lowers the conversion.

1.2.3 Fixed bed with countercurrent of liquid and gas

Normally used as absorption towers for pollution control purposes, these reactors see the liquid phase flowing downward forming thin liquid film on the particle bed, and the gas phase raising as a continuous phase from the bottom. The particles are used mainly to enhance the contact between the two phases and hence are not involved in the reaction.

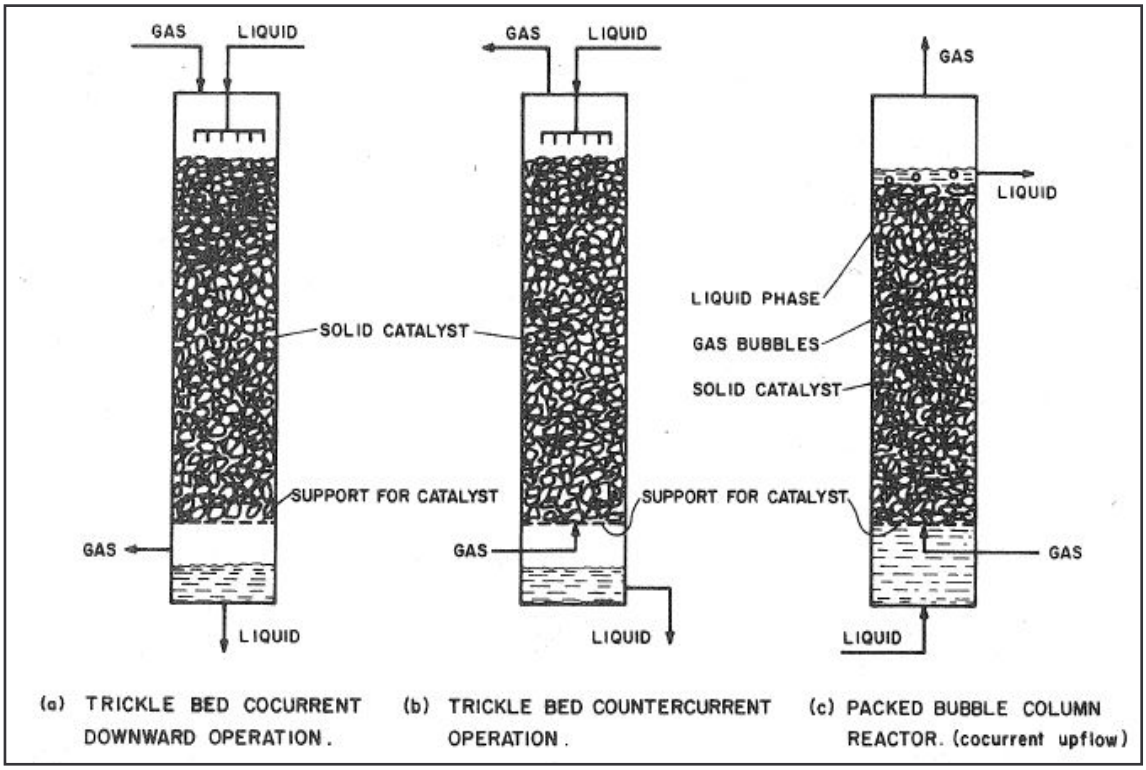

Fig. 2. Three-phase fixed bed reactors (Ramachandran and Chaudhari, 1983).

Capitolo 2

Reattori trickle-bed: idrodinamica e mass transfer

Le prestazioni dei reattori trickle-bed, letti fissi con flusso equicorrente verso il basso di liquido e gas, sono molto sensibili alle condizioni idrodinamiche determinate dai flussi di gas e liquido, dalle caratteristiche del letto (porosità) e dalle proprietà fisiche dei fluidi (densità, viscosità, tensione superficiale del liquido).

Il capitolo riporta dapprima i principali criteri per la definizione del regime idrodinamico nel reattore, quindi si concentra sul regime di *trickle flow*, caratterizzato da bassi valori dei flussi liquido e gas.

Sono descritte le correlazioni più comuni per il calcolo di perdite di carico nel letto, dell'hold-up liquido e del grado di bagnatura del catalizzatore, accennando ai modelli fenomenologici su cui basano. Si riporta anche una panoramica sui più comuni problemi idrodinamici di reattori trickle-bed di piccola taglia e su come sia possibile fronteggiarli diluendo il letto con particelle inerti fini.

Sono quindi riportati i risultati di un'approfondita ricerca in letteratura e di un confronto critico tra le principali correlazioni per la stima dei coefficienti di mass transfer gas-liquido, che ha evidenziato un forte grado di disaccordo tra le varie correlazioni suggerendo la necessità di condurre esperimenti sul proprio sistema per la definizione di questo parametro.

E' riportata infine una rassegna delle più comuni correlazioni per la valutazione del coefficiente di mass transfer liquid-solido.

Chapter 2

Trickle bed reactors: hydrodynamics and mass-transfer

Trickle bed reactors (TBR) are three-phase fixed bed reactors in which liquid and gas flow downward cocurrently. They are widely used in the petroleum and petrochemical industries, such as in hydrocracking, hydrodesulfurization, hydrodemetallization refining processes and in various hydrogenations in the alimentary industry. These reactors are very sensible to the hydrodynamics, i.e. the flow of the gas and liquid phase through the bed of catalyst particles, which influences the mass and heat transfer, as well as the degree of wetting of the catalyst and the pressure drop. In this chapter we first consider the different flow regimes that one can encounter in fixed bed reactors with downflow of gas and liquid, then we focus mainly on the trickling flow regime and review the main correlations considered and used for the estimation of parameters that are vital for the simulation of a trickle bed reactor. We also try to focus on the hydrodynamic problems that can arise in small-scale trickle bed reactors and their possible solutions; these shortcomings usually arise because of the dramatic difference in the liquid and gas superficial velocities between commercial and laboratory units necessary to ensure the same liquid residence time (or space velocity, SV) and when using catalyst particles of the same size of those used in commercial units.

2.1 Flow regimes

While in single phase fixed bed reactors, only two flow regimes are possible, laminar and turbulent, in multiphase fixed bed with cocurrent gas and liquid flow multiple flow regimes exist, ranging from gas-continuous to liquid continuous. They depend on the velocities of the two phases, their physical properties, such as viscosity and density, and from the bed properties, such as porosity and

size of the particles. The knowledge of the flow regime in which a TBR works is fundamental since it influences the hydrodynamics as well as the mass transfer parameters.

Fig. 3 displays the flowmap according to Fukushima and Kusaka (1977a), where a number of different flow regimes are shown as well as the transition boundaries. On the y-axis, a modified Re number Re^*_G for the gas phase is plotted against the similar Re^*_L for the liquid phase; it is defined as follows:

$$\mathrm{Re}^* = \frac{\rho u d_{pe}}{\mu}$$
$$d_{pe} = \frac{2}{3}\frac{d_p \varepsilon_B}{1-\varepsilon_B} \tag{1}$$

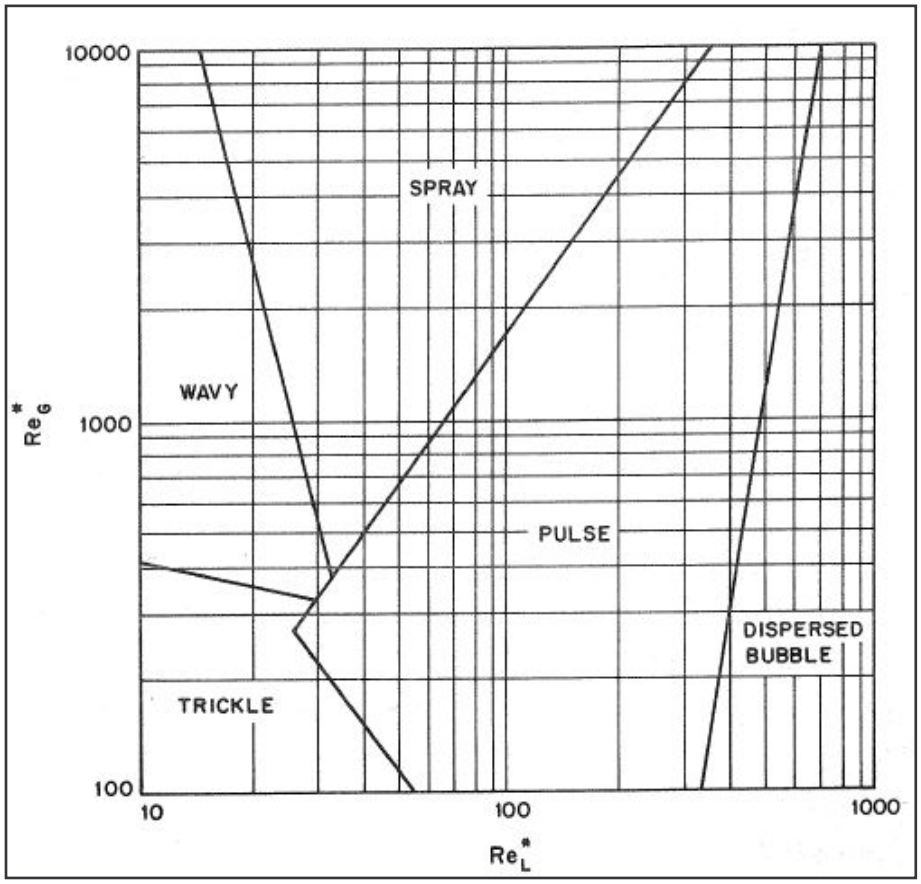

(2)

Fig. 3. Flowmap of Fukushima and Kusaka (1977) (Ramachandran and Chaudhari, 1983).

where ρ (kg/m^3) is the density, u the superficial velocity (m/s), d_{pe} (m) the equivalent diameter of particle as defined, μ (Pa·s) the dynamic viscosity, d_p (m) the diameter of the particle and ε_B (-) the bed porosity. Here we report only the equation that predicts the transition between the trickle and pulse flow regimes:

$$\phi_s^{-0.2}\,\mathrm{Re}^*_L{}^{0.27}\,\mathrm{Re}^*_G{}^{0.2}\left(\frac{d_p}{d_R}\right)^{-0.5} = 18 \tag{3}$$

where ϕ_s (-) is the surface shape factor of the packing, defined as the ration between the geometric surface area of the packing and the square of the packing diameter, and d_R (m) is the diameter of the reactor.

For low Re_G and Re_L numbers the flow regime is called *trickle flow*, which is characterized by the flow of a continuous gas phase and the trickling of liquid in form of droplets or rivulets, with a low interaction between the two phases (this regime is also called *low interaction regime*). Increasing the liquid flow rate while keeping the gas flow rate constant, the liquid starts to flow as pulses, alternate to gas slugs, giving a periodic flow called *pulse flow regime*, in which higher interaction and mixing between the phases occurs. Increasing again the liquid flowrate, the liquid becomes the continuous phase and the gas flows as dispersed bubbles, giving the *dispersed bubble regime*. Increasing the gas flowrate at fixed liquid flowrate, leads to a *spray flow regime*, where liquid flows as a mist, or to a pulsing flow. The boundaries shown in Fig. 3 are calculated by the authors from equations that predict the transition between the different regimes. Practically, the most important hydrodynamics transition is that between the trickle and the pulse flow regimes, in which most of the existing plants operate, due to a trade-off between effectiveness of the mass transfer steps and cost related to pressure drop (van der Merwe, 2007); Fig. 4 from Sie and Krishna (1998) shows how laboratory units, pilot plants and industrial units usually operate in different flow regimes, due to difference in geometry and operating conditions mainly (liquid and gas velocities), this is important to know, since the operating conditions of laboratory reactors must be optimized to obtain meaningful results that can be useful for operating an industrial unit.

A number of equations predicting the flow regime transitions by different authors are reported by Ramachandran and Chaudhari (1983).

An interesting review of the studies on the effect of pressure on the trickle bed hydrodynamics and particularly on transition boundaries has been done by Al Dahhan et al. (1997). The pressure in trickle bed could be as high as 30 MPa (Al Dahhan et al., 1997) to increase the reactant gas solubility in the liquid phase and in case to compensate for the opposite effect of increasing temperature when exothermic reactions occur. The effect of the gas phase on the hydrodynamics is double, due to the superficial velocity and to the density, on which the pressure effect is evident. From experimental studies is concluded that:

- the flow regime transition studied using gases of different molecular weights, occurs at the same gas and liquid velocity if the pressure has been set so that gas densities are the same; in practice, one can study the flow regime transition in a TBR that operates at a high hydrogen pressure, simply by using nitrogen at nearly atmospheric pressure;

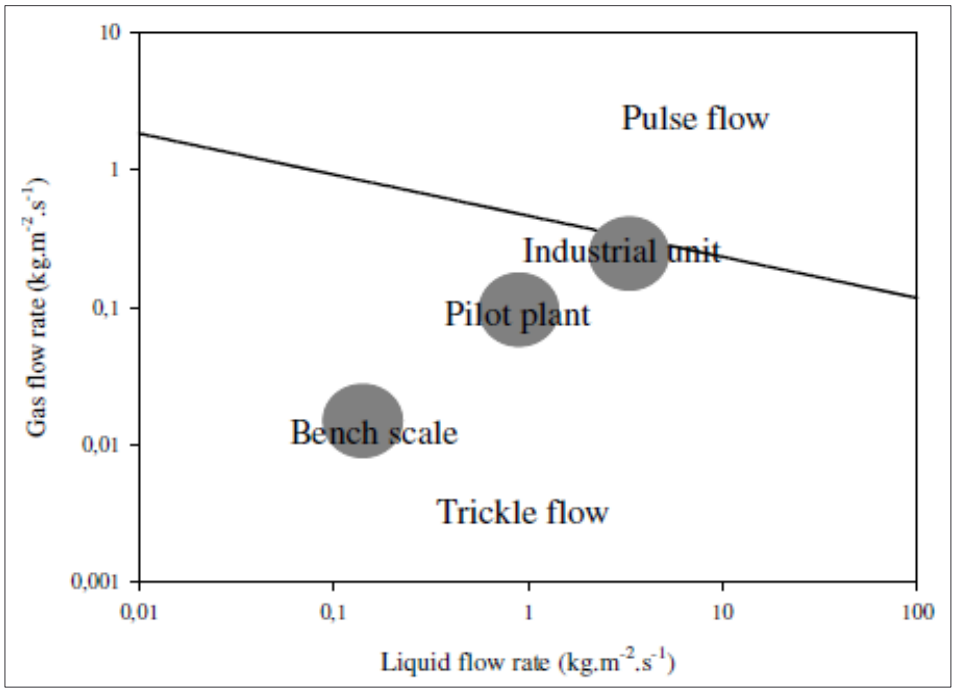

Fig. 4. Typical hydrodynamic flow regimes in trickle bed reactors of different scales (Sie and Krishna, 1998).

- the pressure does not affect the trickle-pulse flow transition as long as the gas density is less than 2.3 kg/m^3;
- for gas density higher than 2.3 kg/m^3, the higher is the pressure, the more the transition boundary, at a given liquid flowrate, shifts towards higher gas velocities. The same happens keeping fixed the gas flowrate and enhancing the liquid throughput; that means that high pressure leads to an enlargement of the trickle flow regime.

An empirical correlation of Larachi et al. (1991) for the prediction of trickle to pulse transition flow regime at high pressure is reported in Eq. (4) for non-foaming liquids; Aydin and Larachi (2005) showed its capability to predict the flow regime transition even at high temperatures:

$$\frac{L\lambda\psi\Phi}{G} = \left(\frac{G}{\lambda}\right)^{-1.25} \tag{4}$$

$$\lambda = \sqrt{\frac{\rho_G \rho_L}{\rho_a \rho_w}}, \psi = \frac{\sigma_w}{\sigma_L}\left(\frac{\mu_L}{\mu_w}\right)^{1/3}\left(\frac{\rho_w}{\rho_L}\right)^{2/3}, \Phi = \frac{1}{4.76 + 0.75\frac{\rho_G}{\rho_a}} \tag{5}$$

where L (kg/m^{2}s) is liquid mass flux, G (kg/m^{2}s) is gas mass flux, ρ_a (kg/m^3) is air density and ρ_w (kg/m^3), μ_w (kg/m^3) and σ_w (N/m) are water density, dynamic viscosity and surface tension respectively. If $(L\lambda\psi\Phi/G) \leq (G/\lambda)^{-1.25}$ then the system is operating in trickle flow regime, in the opposite case it operates in pulse flow; SI units must be used in the equations, since coefficients in the expression of Φ are dimensional.

2.2 Pressure drop

An important aspect of the hydrodynamics in fixed-bed multiphase reactors is the pressure drop, directly related to the energy expense of compressing the recycling gas stream and of pumping the liquid phase through the bed. The scheme of Gianetto and Silveston (1986) in Fig. 5 is interesting since it shows that reactors with a cocurrent downflow of gas and liquid do not suffer of the problem of flooding. The different slopes of the graph are related to the different flow regimes that succeed increasing G, the gas load ($kg/m^2 \cdot s$).

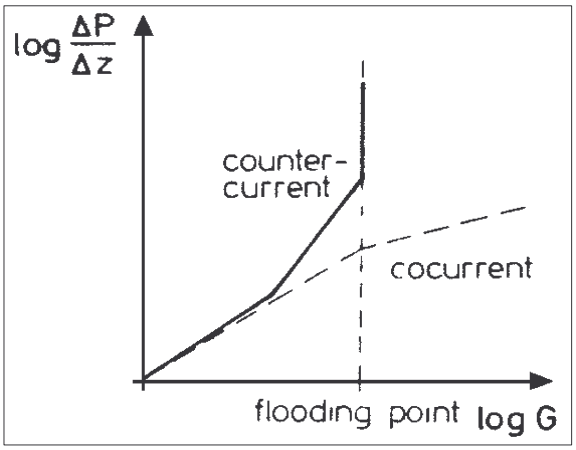

Fig. 5. Influence of gas load on the pressure drop for cocurrent and countercurrent reactors (adapted from Gianetto and Silveston, 1986).

Correlations for the two-phase pressure drop Δp can be given in terms of the Lockhart-Martinelli parameter χ ($\chi = [(\Delta p/z)_L/(\Delta p/z)_G]^2$) where $\Delta p/z$ is the pressure gradient), as discussed by Midoux et al. (1976), which proposed the following equation, valid for non-foaming liquids in the entire hydrodynamics region, while for foaming liquids only in the trickle flow regime:

$$\left(\frac{\frac{\Delta p_{2P}}{z}}{\frac{\Delta p_L}{z}} \right)^2 = 1 + \frac{1}{\chi} + \frac{1.14}{\chi^{0.54}} \qquad \text{for } 0.1 < \chi < 80 \tag{6}$$

where subscript *2P* stands for two-phase. This approach to the calculation of the pressure drop requires the estimation of the single-phase pressure drop for both liquid and gas in the same fixed bed, that can be done by means of the Ergun equation, as suggested by Ramachandran and Chaudhari (1983):

$$\frac{\Delta p}{z} = \frac{150(1-\varepsilon_B)^2}{\varepsilon_B{}^3} \cdot \frac{\mu u}{d_P{}^2} + \frac{1.75(1-\varepsilon_B)}{\varepsilon_B{}^3} \cdot \frac{\rho u^2}{d_P} \tag{7}$$

Other correlations of this type are those of Larkins et al. (1961) and Sato et al. (1973a), as reported in Ramachandran and Chaudhari (1983) and Shah (1979).

The other approach is the one used by Turpin and Huntington (1967), whom correlated the friction factor for two-phase flow to the ratio of the Re numbers of the gas and liquid phases:

$$Z=\frac{\mathrm{Re}_G^{1.167}}{\mathrm{Re}_L^{0.767}}$$
$$\ln f_{2P} = 7.96 - 1.34\ln Z + 0.0021(\ln Z)^2 + 0.0078(\ln Z)^3 \quad (8)$$
$$f_{2P} = \frac{\frac{\Delta p_{2P}}{z} d_{pe}}{2\rho_G u_G^{\,2}}$$

where f_{2P} (-) is the two-phase friction factor.

The review of Al Dahhan et al. (1997) reports some empirical and phenomenological models for the calculation of the pressure drop in high pressure trickle-beds, which have been derived and tested on high pressure data collections. Larachi et al. (1991) proposed the following correlation for the trickle flow regime and non-foaming liquids, derived for pressure in the range 0.2-8.1 MPa:

$$f = \frac{1}{\left(\mathrm{X}_G\left(\mathrm{Re}_L\mathrm{We}_L\right)^{1/4}\right)^{3/2}}\left[31.3 + \frac{17.3}{\sqrt{\mathrm{X}_G\left(\mathrm{Re}_L\mathrm{We}_L\right)^{1/4}}}\right]$$
$$f = \frac{\frac{\Delta p_{2P}}{z} d_k \rho_G}{2G^2} \quad (9)$$
$$\mathrm{X}_G = \frac{u_G}{u_L}\sqrt{\frac{\rho_G}{\rho_L}}$$
$$\mathrm{We}_L = \frac{\rho_L u_L^{\,2} d_P}{\sigma_L}$$

where X_G (-) is the modified Lockhart-Martinelli parameter, We_L (-) is Weber number for the liquid phase and d_k (m) is the hydraulic diameter of Krischer-Kast defined as $d_p{\cdot}(16\varepsilon_B^3/9\pi(1-\varepsilon_B)^2)^{1/3}$. This correlation follows the five limiting cases defined by the phenomenological analysis of Al Dahhan and Dudukovic (1995) which considers the effect of pressure and gas velocity on the hydrodynamics and mass transfer parameters in TBRs at high pressures. Briefly, these five cases are:

1. NO GAS FLOW, ANY PRESSURE: the reactor pressure is not important, the hydrodynamics of the TBR is completely determined by liquid flow rate, physical properties and bed characteristics. For a certain liquid flowrate, the liquid hold-up is the largest, the gas-to-liquid (in the following G/L) mass transfer coefficient and wetting efficiency of the bed are the smallest (the latter is the fraction of external area of the catalyst wetted by the liquid);
2. LOW GAS SUPERFICIAL VELOCITY, LOW PRESSURE ($u_G < 2cm/s$, $p < 3.5bar$): small effect of the pressure and the gas velocity on the hydrodynamics. The pressure drop can still be neglected;

3. HIGH GAS SUPERFICIAL VELOCITY, LOW PRESSURE ($u_G > 2cm/s,\ p < 3.5bar$): interfacial drag between the gas and liquid is enhanced, leading to a better spreading of liquid on the catalyst surface, and so to a higher wetting efficiency and G/L interfacial area (and so G/L mass transfer). The liquid hold-up decreases, while pressure drop increases;
4. LOW GAS SUPERFICIAL VELOCITY, HIGH PRESSURE ($u_G < 2cm/s,\ p > 3.5bar$): a higher pressure means a higher gas density, accordingly, the pressure drop increases. The liquid hold-up, the wetting efficiency and the G/L mass transfer behave like in the previous case, but their variation is less significant than before. The hydrodynamics in the TBR is more sensible to the gas velocity than the pressure;
5. HIGH GAS SUPERFICIAL VELOCITY, HIGH PRESSURE ($u_G > 2cm/s,\ p > 3.5bar$): the effect of the pressure and the gas velocity on the hydrodynamics and mass transfer is at its best; wetting efficiency, G/L interfacial area and pressure drop increase rapidly with p and u_G.

2.3 Liquid hold-up

The liquid hold-up, ε_L, is the ratio of volume of liquid contained in the reactor and the total volume of the reactor. In case of a porous particle, we can identify an internal and an external liquid hold-up (Ramachandran and Chaudhari, 1983; Gianetto and Silveston, 1986). The internal hold-up $\varepsilon_{L,i}$ is due to the liquid inside the catalyst pores, while the external is either dynamic $\varepsilon_{L,d}$ (fraction of liquid which is collected at the bottom of the reactor when this is drained) or stagnant $\varepsilon_{L,s}$ (fraction that remains in the bed made of non-porous particle after drainage). So,

$$\varepsilon_L = \varepsilon_{L,i} + \varepsilon_{L,d} + \varepsilon_{L,s} \tag{10}$$

The major parameters or operating conditions that influence the liquid hold-up are:

1. liquid flow rate and properties, such as viscosity;
2. gas flow rate and pressure, as described in Section 2.2;
3. bed characteristics.

In literature, there are correlations for the total liquid hold-up (ε_L) as well as for the dynamic liquid hold-up ($\varepsilon_{L,d}$), which correlates the liquid hold-up in terms of the Lockhart-Martinelli parameter χ (see Section 2.2) or in terms of Re and Ga, Galileo number (Gianetto and Silveston, 1986) defined as:

$$\mathrm{Ga} = \frac{\rho^2 d_p{}^3 g}{\mu^2} \tag{11}$$

Among those derived for TBRs at atmospheric pressure, we reported the correlation by Midoux et al. (1976) for ε_L, Eq. (12), and the correlation for the low interaction regime by Specchia and Baldi (1977) for $\varepsilon_{L,d}$, Eq. (13) :

$$\varepsilon_L=\varepsilon_B \frac{0.66\chi^{0.81}}{1+0.66\chi^{0.81}} \qquad for\ 0.1<\chi<80 \tag{12}$$

$$\varepsilon_{L,d}=\varepsilon_B \cdot 3.86\,\mathrm{Re}_L^{\,0.545}(\mathrm{Ga}^*)^{-0.42}\left(\frac{a_p d_p}{\varepsilon_B}\right)^{0.65} \qquad for\ 3<\mathrm{Re}_L<470 \tag{13}$$

$$\mathrm{Ga}^* = \frac{d_p^{\,3}\rho_L(\rho_L g+\frac{\Delta p_{GL}}{z})}{\mu_L^{\,2}}$$

where a_p (1/m) is the external surface of particles per unit volume of bed and g (m/s^2) is the gravitational acceleration.

Al Dahhan et al. (1997) present correlations derived for TBRs at high pressures. Among these, Larachi et al. (1991) have proposed empirical correlation for non-foaming liquids, Eq. (14), which respects the trend of the five limiting cases described above:

$$\varepsilon_L=\varepsilon_B(1-10^{-\Gamma})$$
$$\Gamma = 1.22\frac{\mathrm{We}_L^{\,0.15}}{\mathrm{X}_G^{\,0.15}\,\mathrm{Re}_L^{\,0.20}} \tag{14}$$

2.4 Wetting efficiency

Catalyst wetting is an important hydrodynamic parameter of TBR, influencing the liquid-solid (L/S) mass transfer. It has different effects whether the reaction is liquid-limited, i.e. the limiting reactant is the one carried by the liquid phase, or gas-limited, i.e. the limiting reactant is the one carried by the gas phase. In the 1st case, if the liquid reactant volatility is negligible, a higher wetting efficiency (η_{CE}) of the catalyst leads to an enhancement of the conversion, since the L/S mass transfer interfacial area is higher, while if reaction is gas-limited, higher η_{CE} normally gives a decrease in the conversion (Al Dahhan, Dudukovic (1995)).

Two kinds of catalyst wetting appear in the case of porous particles: *internal wetting*, or pore filling, which is normally complete, due to capillary effects, and *external wetting*, which depends on liquid and gas flow rates, liquid viscosity, bed characteristics, pressure (or gas density) and pre-wetting methods (Mary et al., 2009). The dependence of the wetting efficiency on the gas flow rate and pressure has been outlined in Section 2.2, while it increases with the liquid flow rate. Looking at the earlier literature, one of the first correlations given for the wetting efficiency η_{CE}, defined as the fraction of the external area of the catalyst wetted by the liquid, was that of Puranik and Vogelpohl (1974); by the way, it was derived at atmospheric pressure, and it does not include the effect of the gas superficial velocity on η_{CE}, which is negligible at low pressure.

Based on the phenomenological model developed by Holub et al. (1992) and modified by Al Dahhan and Dudukovic (1995), it results that increasing either gas superficial velocity or pressure (i.e., gas density), shear stresses at the G/L interface increases, reducing the thickness of the liquid film, enhancing the spreading of liquid and so the wetting efficiency (see the five limiting cases described in Section 2.2). Al Dahhan and Dudukovic (1995) proposed the following correlation which takes into account these effects:

$$\eta_{CE} = 1.104\,\mathrm{Re}_{L,m}^{1/3}\left[\frac{1+\dfrac{\Delta p_{2P}}{\dfrac{z}{\rho_L g}}}{\mathrm{Ga}_{L,m}}\right]^{1/9}$$

$$\mathrm{Re}_{L,m} = \frac{\rho_L u_L d_p}{\mu_L(1-\varepsilon_B)} \qquad (15)$$

$$\mathrm{Ga}_{L,m} = \frac{d_p^{\,3}\rho_L^{\,2} g \varepsilon_B^{\,3}}{\mu_L^{\,2}(1-\varepsilon_B)^3}$$

The range of liquid and gas mass fluxes on which it has been derived are respectively *6.64e-3<G<4.03* and *0.42<L<2.7* kg/m^{2}s and for pressure in the range *0.31<p<5* MPa.

In a recent review of Mary et al. (2009) a simple criterion is given to assess the assumption of complete wetting in a laboratory small-scale trickle bed unit; it links the viscous and the gravity forces and has been determined on an extensive amount of experimental data. The dimensionless wetting number W defined as:

$$\mathrm{W} = \frac{\mu_L u_L}{\rho_L d_p^{\,2} g} \qquad (16)$$

should be higher than $5\cdot10^{-6}$ in order to ensure adequate catalyst wetting. As a rule of thumb, the smaller is the diameter of the smallest particles, the shorter can be the length of the catalyst bed to achieve good catalyst wetting.

2.5 Catalyst bed dilution

The technique of diluting the catalyst bed with fines, small non-porous, inert particles of about 1/10 of catalyst diameter, if the catalyst is of a few mm sizes, has found large applications as a tool to obtain reliable results in small-scale laboratory trickle-bed reactors used for testing of new catalysts or alternative feedstocks, while using commercially available catalyst particle sizes; the use of fines dispersed among the catalyst particles limits or totally eliminates hydrodynamic shortcomings typical of this kind of small-scale units due to the very low liquid velocities needed to ensure the

same space velocity (SV) of an industrial unit. To understand the dramatic changes in the bed characteristics and the liquid velocity with the scale-up or scale-down of trickle bed units, we report Tab. 2 adapted from Sie (1991), regarding hydrotreating units, for SV = $21h^{-1}$ and d_p=0.15cm.

The very low liquid velocities in the laboratory units ensure to operate within the trickle flow regime (as shown by Fig. 4), but give rise to problems such as incomplete catalyst wetting and so partial catalyst utilization and enhance liquid axial dispersion. Moreover, when in laboratory reactors commercial catalyst sizes are used, the empirical criterion $d_R/d_p \geq 20$ which assures good and uniform liquid distribution is difficult to fulfil.

Tab. 2. Typical hydrotreating data for different sizes of TBR (adapted from Sie (1991)).

specification	commercial	pilot plant	bench-scale	microflow
catalyst volume (L)	$1 \cdot 10^5$	10	0.15	0.008
diameter (cm)	250	4	2	1
length (cm)	2000	800	50	10
u_L (cm/s)	1.1	0.4	0.03	0.006

In fact for lower d_R/d_p, the bed porosity at the wall is higher, leading to channelling phenomena and contributing as well to poor catalyst wetting.

In the articles of Al Dahhan and Dudukovic (1996), as well as Metaxas and Papayannakos (2006, 2008), it is recommended to dilute the catalyst bed with inert fines in order to overcome the problems of liquid maldistribution, deviations from plug flow conditions and poor wetting efficiency due to low liquid and gas velocities and low ratios d_R/d_p in the laboratory-scale trickle-bed reactors. The fines create more solid-solid contact points and area over which liquid flows, reducing the bed voidage especially along the reactor wall (Al Dahhan and Dudukovic, 1996). In this way, the hydrodynamics is largely determined by these small particles, whereas catalytic phenomena depend on the catalyst particles, which are of the same shape and size of the commercial ones. Al Dahhan and Dudukovic (1996) call this a real "decoupling of hydrodynamics and kinetics", which allows to perform reliable experiments on these small-scale reactors. Their experiments showed that in diluted beds, the wetting efficiency increases significantly, as well as happens for the pressure drop, because the bed voidage is lower, and the liquid holdup, due to the higher number of solid-solid contact points that increases external hold-up.

Concerning the axial dispersion, in the review of Mary et al. (2009) on small-scale trickle-bed reactors, two widely accepted empirical criteria are proposed to check whether axial mixing can be neglected:

$$\frac{L_B}{d_p} \geq 100$$
$$\frac{d_R}{d_p} \geq 10 \qquad (17)$$

where L_B is the bed length (m). It is clear that the larger the particle diameter, the longer has to be the bed in order to avoid consistent axial mixing. Dilution of the bed is therefore a practical way to reduce backmixing (Mary et al., 2009).

2.6 Gas-to-liquid mass transfer

In three-phase catalytic reactors, several mass transfer steps are involved in defining the overall reaction rate. If we consider the reactant A carried by the gas phase, the A-molecules have to move from the gas to the liquid phase, then from liquid bulk to the catalyst surface and finally inside the porous particles. The simplest way to describe the external gas-to-liquid (G/L) mass transfer is based on the film-theory; according to this, mass-transfer rate of A from the gas to the liquid phase is defined as (given by Ramachandran and Chaudhari, 1983):

$$R_A = k_{A,GL} a_{GL} \left(c_{A,L}^{\ *} - c_{A,L} \right) \qquad (18)$$

where $k_{A,GL}$ (m/s) is the G/L mass transfer coefficient, a_{GL} (1/m) is the G/L interfacial area per unit reactor volume (in the following of the section we refer to it simply as a) and $c_{A,L}^{\ *}$ and $c_{A,L}$ (mol/m^3) are the saturation concentration of A in liquid phase and the actual liquid concentration of A, respectively. The product of the G/L mass transfer coefficient and the interfacial area, is related to gas-side and liquid-side mass transfer coefficient:

$$k_{GL}a = \left(\frac{H_A}{k_G a} + \frac{1}{k_L a} \right)^{-1} \qquad (19)$$

where H_A ((mol$_A$/m$^3_{liq}$)·(m$^3_{gas}$/mol$_A$)) is the Henry's constant that defines the solubility of A in liquid ($H_A = c_{A,L}^{\ *}/c_{A,G}$), $k_G a$ and $k_L a$ (1/s) are the gas-side and liquid-side mass transfer coefficients multiplied by the interfacial area. As stated by Ramachandran and Chaudhari (1983), if the gas phase consists of pure A and A is scarcely soluble in liquid (meaning that H_A is small), the gas-side mass transfer can be neglected, so that the overall G/L mass transfer coefficient reduces to liquid-side one. This is affected by both the gas and the liquid flowrates, the physical properties of the liquid (density, viscosity, surface tension and foaming) and the bed characteristics (Gianetto and Silveston). In literature there is an abundance of correlations for the liquid-side mass transfer coefficient evaluated for TBR operating at atmospheric pressure, as reported by Al Dahhan et al.

(1997); in the following, we discuss some of the most cited correlations for the estimation of the volumetric liquid-side mass transfer coefficient k_La.

Eq. (20) is the correlation of Goto and Smith (1975a) valid for the low interaction regime:

$$\frac{k_L a}{D} = \alpha_L \left(\frac{\rho_L u_L}{\mu_L} \right)^n \left(\frac{\mu_L}{\rho_L D} \right)^{0.5} \tag{20}$$

where D (m^2/s) is the liquid-phase diffusion coefficient for the component transferred from gas to liquid, α_L and n are parameters varying with the particle geometry (original paper of Goto and Smith reports values for glass beads and CuO/ZnO particles, which are shown in Tab. 3); attention must be paid to α_L, which is a parameter with specific dimensions and to the fact that the original correlation is expressed in cgs units. This correlation does not consider the influence of gas flowrate on the mass transfer coefficient. Identical to Eq. (20) is the correlation of Mahajani and Sharma (1979) for the trickle flow regime, but the values for α_L and n are 8.08 and 0.40 respectively; again the correlation is given in cgs units.

Turek and Lange (1981) measured k_La for very low liquid velocities and proposed the following correlation in cgs units:

$$\frac{k_L a}{D} = 16.8 \mathrm{Ga}_L^{-0.22} \mathrm{Re}_L^{0.25} \mathrm{Sc}_L^{0.5} \tag{21}$$

where Sc_L (-) is Schmidt number for liquid ($\mathrm{Sc}_L=\mu_L/\rho_L D$) and the coefficient 16.8 is dimensional ($1/cm^2$). Fukushima and Kusaka (1977b) proposed the following correlation for the trickle flow regime:

$$\frac{k_L a d_p^{\,2}}{D\left(1-\frac{\varepsilon_L}{\varepsilon_B}\right)} = 2\left(\frac{S_p}{d_p^{\,2}}\right)^{0.2} \mathrm{Re}_L^{0.73} \mathrm{Re}_G^{0.2} \mathrm{Sc}_L^{0.5} \left(\frac{d_p}{d_R}\right)^{0.2} \tag{22}$$

where S_p (m^2) is the particle geometrical surface area. Here a certain dependence on gas flowrate is comprised, as well as on density of gas.

The correlation of Ellman (1988) has been recommended by Gianetto and Specchia (1992), since it is based on a very large amount of data obtained with different gas-liquid systems in a wide range of operating conditions:

$$\frac{k_L a d_k^{\,2}}{D} = \Omega \mathrm{X}_G^{\,a} \mathrm{Re}_L^{\,b} \mathrm{We}_L^{\,c} \mathrm{Sc}_L^{\,d} \left(\frac{a_s d_k}{1-\varepsilon_B}\right)^e \tag{23}$$

Parameters Ω, a, b, c, d and e are given in Tab. 5. This correlation contains a dependence of k_La on liquid velocity, gas velocity and pressure (inside $\mathrm{X_G}$).

As reported by Al Dahhan et al. (1997), the G/L mass transfer is enhanced by high pressures, at given gas and liquid superficial velocities, besides the gas flowrate, especially at high pressure and high liquid flowrates; this has been confirmed by the experimental work of Larachi et al. (1998),

where it is highlighted in particular that it is mainly the G/L interfacial area to increase with pressure, rather than the coefficient k_L. Two phenomenological models have been proposed to explain these results, the first one being the one of Al Dahhan and Dudukovic (1995), already cited above, that attributes the increase in mass transfer to the enhanced spreading of liquid on the catalyst, due to the higher shear stress between phases, thus increasing the G/L as well as the L/S contacting area. The second one is the Larachi et al. (1998), that explains the enhanced mass transfer not only for the spreading of liquid film due to higher interfacial shear, but also to the entrainment of gas bubbles in the liquid film, happening at $u_G > 2cm/s$ (see Section 2.2) and high pressure, that increases sensibly the G/L interfacial area.

Accordingly at high pressure, the model of Larachi et al. (1998) considers two contributions to the G/L mass transfer, a macroscopic contribution due to the mass transfer that takes place at the interfacial area between the liquid film and the continuous gas phase (taking into account the enhanced spreading of the liquid), and a microscopic contribution, due to the mass transfer at the surface of gas bubbles trapped in the liquid film (see Fig. 6). Correlation of Larachi et al. (1998) for both the trickle flow regime and the transition region between trickle and pulse flow is reported in Eq. (24):

$$k_L a = \left(k_L a\right)^\circ \frac{\eta_{CE}}{\eta_{CE}^\circ} + k_L^{(\mathrm{Sh}=2)} \left(a - a^\circ\right) \tag{24}$$

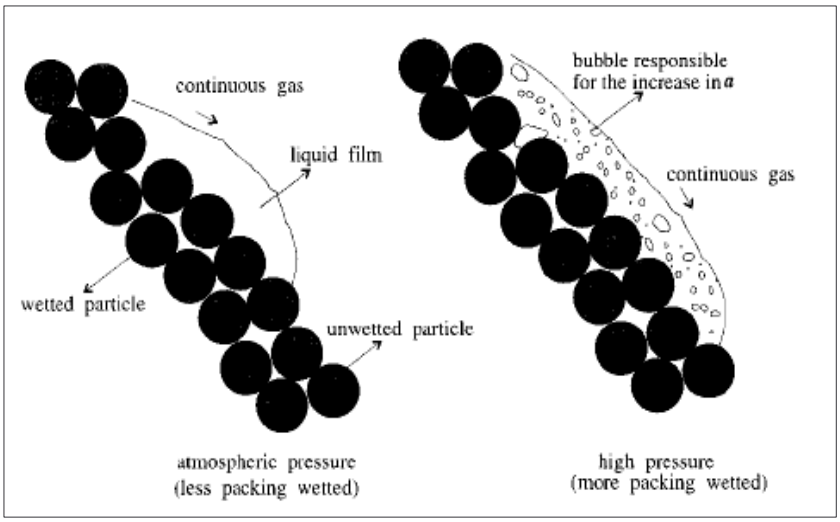

Fig. 6. Improved spreading of liquid phase and entrainment of the gas bubbles in the liquid film as an effect of high pressure (Larachi et al., 1998).

where each of the two addends represents one of the two different contributions to the G/L mass transfer coefficient at high pressure as described previously. The notation ° points out parameters referred to atmospheric pressure, the difference a-a° in the second addend defines exactly the surface area of bubbles entrained in the liquid phase, while the mass transfer coefficient $k_L^{(\mathrm{Sh}=2)}$ (m/s) is referred to a Sherwood number of 2, typical for creeping (or stagnant) flow around spheres.

Larachi et al. (1998) suggest to use correlation of Wild et al. (1992) for transition flow for the estimation of $k_L°$ and $a°$, which we report:

$$\frac{k_L a d_k^{\,2}}{D} = 0.091\left[\mathrm{X}_G^{1/4}\,\mathrm{Re}_L^{1/5}\,\mathrm{We}_L^{1/5}\mathrm{Sc}_L^{3/10}\left(\frac{a_p d_k}{1-\varepsilon_B}\right)^{1/4}\right]^{3.8} \tag{25}$$

where a_p (1/m) is the external area of catalyst particles per unit reactor volume.

Finally, we report the correlation of Yaichi et al. (1988) as described by Iliuta et al. (1999) for the estimation of gas-side mass transfer coefficient, in order to check whether the influence of the gas-phase resistance on the mass transfer is truly negligible:

$$k_G a = 0.049 D_G \frac{a_p^{\,0.985}}{d_p^{\,1.015}}\left(\mathrm{Re}_G\right)^{1.08}\left(\mathrm{Re}_L\right)^{0.2}\left(\mathrm{Sc}_G\right)^{0.5}\left(\frac{d_p}{d_R}\right)^{0.72} \tag{26}$$

The details of the applicability fields of these correlations are given in Tab. 6, except for Wild et al. (1992) and Ellman (1988), whose original works were not available. Fukushima and Kusaka (1977b) measured the G/L mass transfer coefficient in four different regimes, trickle, pulse, spray and dispersed bubble, covering a large range of liquid and gas velocities; this is the reason for which we do not report it in Tab. 6. For each of these flow regimes, they proposed a correlation for the G/L mass transfer coefficient; looking at their flowmap in Fig. 3, we can state that $\mathrm{Re}_G^{\,*} < 250$ and $\mathrm{Re}_L^{\,*} < 30$ are safety limits to be in the trickle flow regime. The original work of Wild et al. (1992) was not available, but the correlation has been taken from the article of Al Dahhan et al. (1997) and checked for safety with that reported in the articles of Iliuta et al. (1999) and Roininen et al. (2009); however, each of these authors reported only the flow regime for which the correlation was derived. It should be noticed that Larachi et al. (1998) is the only correlation derived for high-pressure trickle-beds; we also note that there are strong differences for in the range of liquid velocities investigated, while the gas velocities are varying inside the typical range for a laboratory/pilot TBR.

Tab. 3. Values of parameters α_L and n_L determined by Goto and Smith (1975a).

particles	α_L (cm^{nL-2})	n_L
Glass beads (0.413 cm)	2.8	0.40
CuO/ZnO (0.291cm)	6.0	0.41
CuO/ZnO (0.0541cm)	7.8	0.39

Tab. 4. Physical properties of liquid and gas phases at the conditions for which correlations have been evaluated.

ρ_L (kg/m^3)	μ_L (Pa·s)	σ_L (mN/m)	ρ_G (kg/m^3)	μ_G (Pa·s)
997.1	0.30e-3	51.6	2.54	1.04e-5

Tab. 5. Values of parameters in the correlation of Ellman (1988) as reported in Gianetto and Specchia (1992).

conditions	Ω	*a*	*b*	*c*	*d*	*e*
$X_G<0.8$	0.45	0.65	1.04	0.26	0.65	0.325
$0.8<X_G<1.2$	0.091	0.95	0.76	0.76	1.14	0.95
$X_G>1.2$	0.00028	0.85	0.68	0.68	1.70	0.85

Tab. 6. Operation conditions and bed characteristics for which the correlations have been derived.

characteristics of system investigated	Goto and Smith (1975a)	Mahajani and Sharma (1979)	Turek and Lange (1981)	Fukushima and Kusaka (1977)	Larachi et al. (1998)
u_L (cm/s)	0.047-0.52	0.08-0.3	0-0.05	/	0.14-0.77
u_G (cm/s)	0.2-0.75	6-18	0-3	/	0.5/6
p (bar)	1.013	1.013	1.5-4	1.013	3-32
d_p (mm)	0.5-4	3-4	0.5-3	11.6-12.8	0.9-3.4
d_p/d_R (-)	0.02-0.15	0.06-0.08	0.01-0.09	0.1	0.04-0.15
liquid phase	aqueous	aqueous and organic	organic	aqueous	aqueous and organic
hydrodynamic flow regime	trickle flow regime	trickle flow regime	trickle flow regime	trickle flow regime	trickle flow and transition trickle/pulse

Tab.7. Operation conditions and bed characteristics for which the correlations have been evaluated.

T (°C)	p (bar)	d_p inert diluent (mm)	a_p of catalyst (1/m)	ε_B (-)	d_p/d_R (-)
100	40	0.2	3600	0.25	0.02

The values of particle sizes used in the experimental studies by the various authors are similar, except for Fukushima and Kusaka. Also ratios particle size-to-column diameter are in the same range 0.01-0.1. In order to compare the results which correlations give, we calculated trends of the G/L mass transfer coefficient with liquid and gas velocities for a laboratory trickle-bed reactor with a diluted catalytic bed, whose characteristics are summarized in Tab. 7.

In Fig. 7a to 7g these trends are shown; the arrows reported in some figures denote if the liquid velocity highlighted is the lower or upper bound of the experimental range investigated by the authors, since the range of u_L for which the correlations have been tested could not comprehend the whole range of u_L investigated by the different authors. The ranges of u_L for which correlation of Larachi et al. (1998) has been derived is not inside the range of interest for this work, which is about 1 order of magnitude lower. The one of Fukushima and Kusaka (1977) is valid inside the boundaries of the trickle flow regime defined by their flowmap, and for the conditions tested we are

definitely inside these boundaries. Wherever a legend showing the gas velocities (u_G) considered does not appear, it means that those correlations do not consider a dependence from gas velocity.

For the details of the calculation of the physical properties of the liquid and gas phases reported in Tab. 4, we refer to Section 4.2; liquid phase is a diluted aqueous solution of the sugar L-arabinose, while gas phase is pure hydrogen.

Tab. 8 reports the estimations of the G/L mass transfer coefficient for the TBR considered from the different correlations at u_L = 0.05 cm/s - u_G = 5 cm/s and u_L = 0.025 cm/s - u_G = 2 cm/s to compare their predictions. We can see the huge degree of disagreement among them; Wild et al. (1992) and Larachi et al. (1998) give very low values, while at the opposite Fukushima and Kusaka (1977), Ellman (1988) and Mahajani and Sharma (1979) give much larger estimations.

A similar strong disagreement among the predictions provided by different correlations has been found by Metaxas and Papayannakos (2006), who were working with the hydrogenation of benzene (up to 7%wt) in a n-hexane/cyclohexane solvent in a bench-scale trickle-bed reactor diluted with fines, which had bed characteristics and was operated under conditions close to the ones we used; they applied Goto and Smith (1975), Turek and Lange (1981), Wild et al. (1992) and Ellman (1988) correlations among the others. Tab. 9 reported the details of their experimental setup, while in Fig. 8 we see the comparison among their experimental values of the liquid-side mass transfer coefficients for hydrogen and benzene and those of the correlations. It is important to underscore that the form of the Ellman correlation used was that for $X_G < 0.8$, although for their conditions X_G could be worth up to 2; however this was the correlation that gave the closest values to those determined experimentally, although different for about one order of magnitude, especially at high gas velocities. They explained these results with the fact that such correlations were not developed for such low gas and liquid velocities, and maybe for such particular system as a small-scale trickle bed diluted with fines.

The values of k_La for hydrogen obtained by these authors, both in the bed diluted with 0.25mm fines (Metaxas and Papayannakos, 2006) and with 2.4mm fines (in this case catalyst particle sizes was about 1mm, thus they determined the hydrodynamics (Metaxas and Papayannakos, 2008)) and in operating conditions close to the ones we are also interested in, were in the range $10^{-2}/10^{-1}$ 1/s. Keeping present that gas and liquid velocities they used were slightly lower than ours, if we look at the results that the different correlations gave us, we can therefore state that the estimations obtained from Mahajani and Sharma (1979), Ellman (1988) and Fukushima and Kusaka (1977) can be considered more realistic. Obviously this is something to check carefully with ad hoc experiments on our system, but in the absence of experimental data about G/L mass transfer this is the best we have.

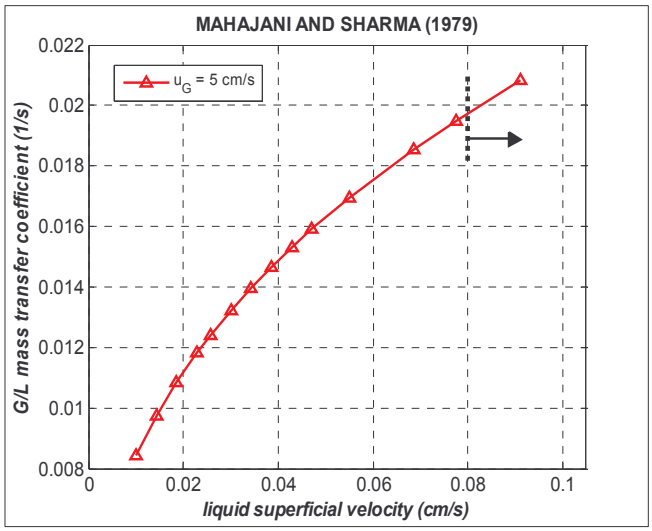
MAHAJANI AND SHARMA (1979)
u_G = 5 cm/s
G/L mass transfer coefficient (1/s)
liquid superficial velocity (cm/s)
0.022
0.02
0.018
0.016
0.014
0.012
0.01
0.008
0
0.02
0.04
0.06
0.08
0.1

a)

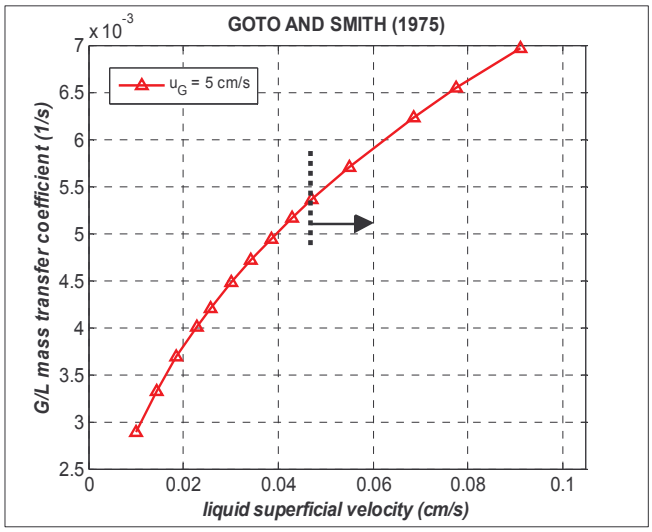
GOTO AND SMITH (1975)
x 10^-3
u_G = 5 cm/s
G/L mass transfer coefficient (1/s)
liquid superficial velocity (cm/s)
7
6.5
6
5.5
5
4.5
4
3.5
3
2.5
0
0.02
0.04
0.06
0.08
0.1

b)

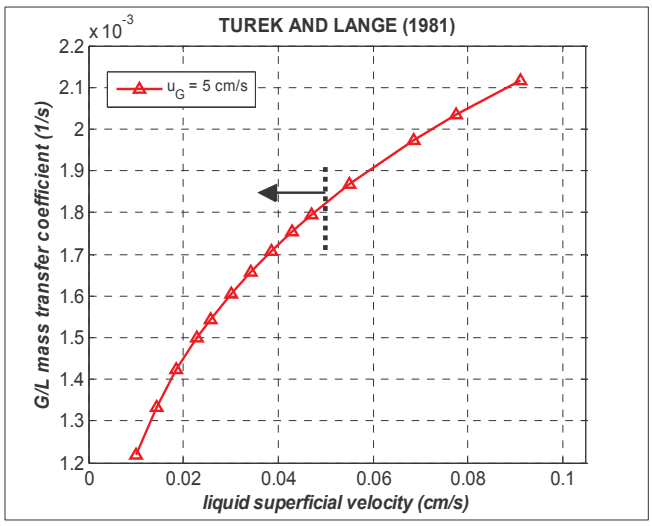
TUREK AND LANGE (1981)
x 10^-3
u_G = 5 cm/s
G/L mass transfer coefficient (1/s)
liquid superficial velocity (cm/s)
2.2
2.1
2
1.9
1.8
1.7
1.6
1.5
1.4
1.3
1.2
0
0.02
0.04
0.06
0.08
0.1

c)

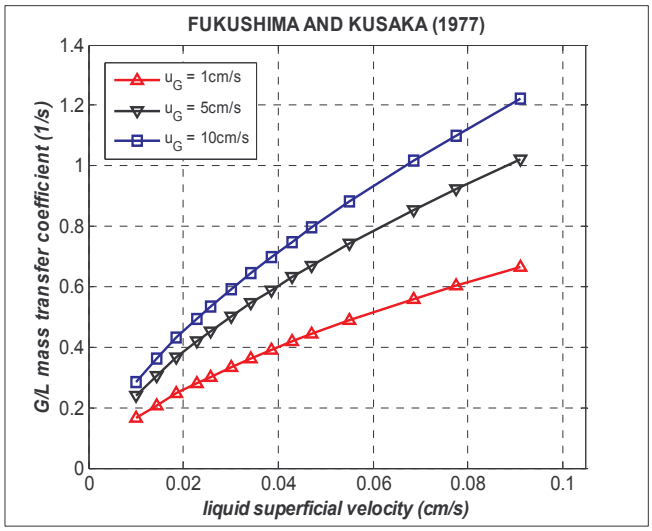
FUKUSHIMA AND KUSAKA (1977)
G/L mass transfer coefficient (1/s)
liquid superficial velocity (cm/s)
uG = 1cm/s
uG = 5cm/s
uG = 10cm/s
0
0.2
0.4
0.6
0.8
1
1.2
1.4
0.02
0.04
0.06
0.08
0.1

d)

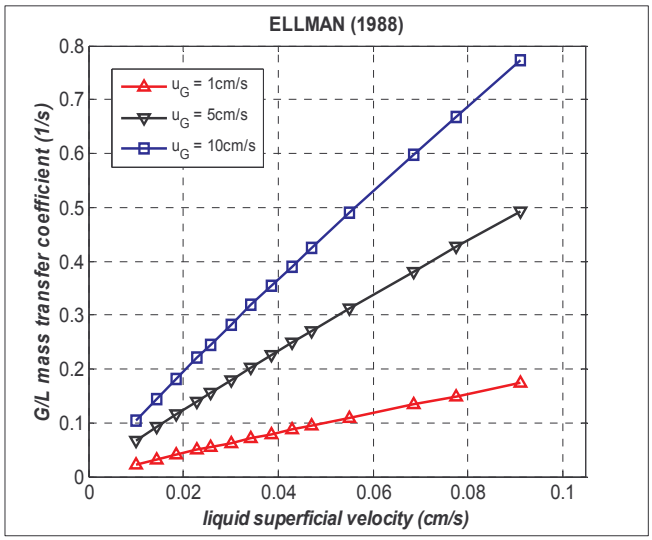
ELLMAN (1988)
G/L mass transfer coefficient (1/s)
liquid superficial velocity (cm/s)
uG = 1cm/s
uG = 5cm/s
uG = 10cm/s
0
0.1
0.2
0.3
0.4
0.5
0.6
0.7
0.8
0.02
0.04
0.06
0.08
0.1

e)

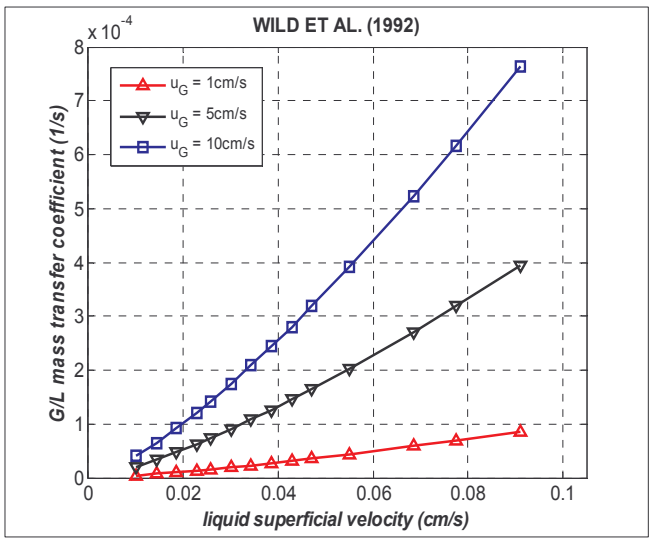
WILD ET AL. (1992)
x 10-4
G/L mass transfer coefficient (1/s)
liquid superficial velocity (cm/s)
uG = 1cm/s
uG = 5cm/s
uG = 10cm/s
0
1
2
3
4
5
6
7
8
0.02
0.04
0.06
0.08
0.1

f)

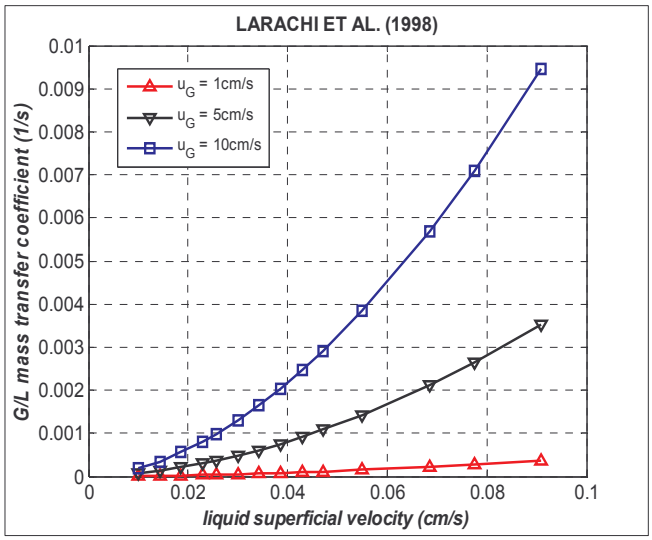

g)

Fig. 7. Trends of the G/L mass transfer coefficient with liquid and gas superficial velocities for the laboratory TBR.

A check to assure that the G/L mass transfer coefficient $k_{GL}a$ can be effectively predicted only from liquid-side coefficient k_La has been made. Correlation by Yaichi et al. (1988) was used for k_Ga, while Ellman (1988) and Fukushima and Kusaka (1977) for k_La (since these 2 correlations give the higher estimations of k_La, it is obvious to make the verification with them). In Tab. 10 some results are reported, for different temperatures and pressures, liquid and gas velocities. Only for k_La from Fukushima and Kusaka (1977) in the case of high liquid velocity (0.1cm/s) and low gas velocity (2cm/s), the ratio $k_{GL}a/k_La$ is less than 1, meaning that it is reasonable to neglect gas-side for the range of operative conditions of interest.

Tab. 8. Values of k_La (s^{-1}) for the laboratory TBR considered from correlations.

liquid and gas velocity (cm/s)	Goto and Smith (1975a)	Mahajani and Sharma (1979)	Turek and Lange (1981)	Fukushima and Kusaka (1977)
$u_L = 0.05$ $u_G = 5$	5.5e-3	1.6e-2	1.8e-3	7.0e-1
$u_L = 0.025$ $u_G = 2$	4.2e-3	1.2e-2	1.5e-3	3.7e-1

liquid and gas velocity (cm/s)	Ellman (1988)	Wild et al. (1992)	Larachi et al. (1998)
$u_L = 0.05$ $u_G = 5$	2.9e-1	1.8e-4	1.2e-3
$u_L = 0.025$ $u_G = 2$	9.6e-2	3.6e-5	1.3e-4

Tab. 9. Characteristics of the bench-scale laboratory TBR used by Metaxas and Papayannakos (2006).

T (°C)	p (bar)	u_L (cm/s)	u_G (cm/s)	d_R (mm)	d_p catalyst (mm)	d_p inert diluent (mm)	L_B (cm)
70/100	16	0.005/0.015	0.01/0.1	25.4	0.32/0.40	0.25	7

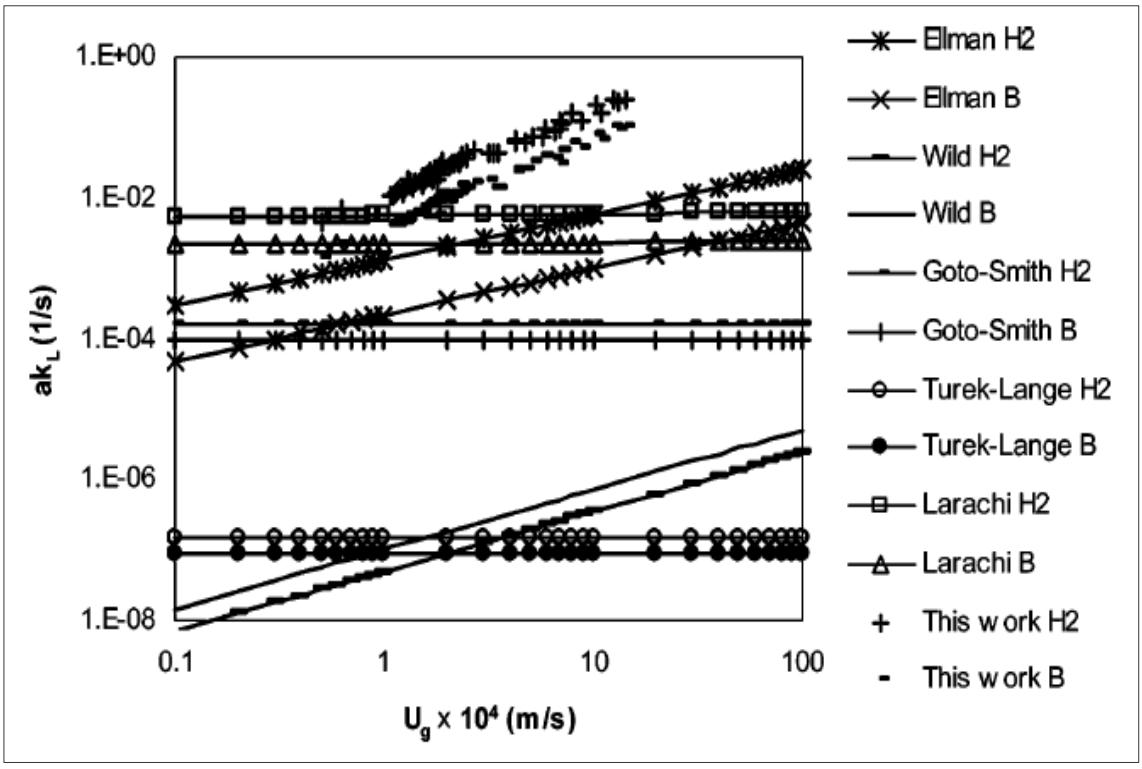

Fig. 8. Liquid-side mass transfer coefficients from experimental work of Metaxas and Papayannakos (2006) and from common correlations (adapted from Metaxas and Papayannakos, 2006; u_L is about 0.01cm/s).

Tab. 10. Results of the comparison between liquid-side and gas-side mass transfer coefficients for H_2 (a) correlation of Ellman (1988), b) correlation of Fukushima and Kusaka (1977)).

a)

T (°C)	p (bar)	u_L (cm/s)	u_G (cm/s)	$k_{GL}a/k_La$ (-)
80	30	0.05	5	1.0
80	50	0.05	5	1.0
130	30	0.05	5	1.0
130	50	0.05	5	1.0
100	50	0.025	5	1.0
100	50	0.1	5	1.0
100	50	0.025	15	1.0
100	50	0.1	2	1.0

b)

T (°C)	p (bar)	u_L (cm/s)	u_G (cm/s)	$k_{GL}a/k_La$ (-)
80	30	0.05	5	1.0
80	50	0.05	5	1.0
130	30	0.05	5	1.0
130	50	0.05	5	1.0
100	50	0.025	5	1.0
100	50	0.1	5	1.0
100	50	0.025	15	1.0
100	50	0.1	2	>0.9

From this brief literature review on the correlations for the G/L mass transfer coefficient and their application to the system of interest, it emerges that it is strongly advisable to make measurements of this parameter for the system we are interested to study and simulate, rather than rely on literature correlations; techniques to measure the k_La in continuous trickle-bed reactors, such as physical absorption-desorption with or without reaction are reported in Ramachandran and Chaudhari (1983), as well as in classical papers such as Goto and Smith (1975a).

From experimental measurements of the k_La on our own system we can reveal its dependence on u_L, u_G, liquid properties and bed characteristics and finally just fit the adjustable parameter/s of a particular correlation already available in the literature on our data or develop a new one. In this way we have a tool that let us to simulate our system with a much higher degree of accuracy than that we would have using correlations developed from different systems.

In this work we decided to use the correlation of Ellman (1988) to evaluate G/L mass transfer coefficients.

2.7 Liquid-to-solid mass transfer

The liquid-to-solid (L/S) mass transfer is an additional transport step which is necessary to carry the species from the liquid phase to the external surface of the catalyst. Based on the film-theory, the rate of mass transfer of species A from the bulk liquid to the surface of catalyst can be written as:

$$R_A = k_{LS} a_{LS} \left(c_{A,L} - c_{A,S} \right) \tag{27}$$

where k_{LS} (m/s) is the L/S mass transfer coefficient, a_{LS} (1/m) is the L/S external area of catalyst particles per unit reactor volume (in the following of the section we refer to it simply as a or a_p) and $c_{A,L}$ and $c_{A,S}$ (mol/m^3) are the concentration of A in the bulk liquid and the concentration of A in the liquid at the catalyst surface respectively.

The L/S mass transfer coefficient is affected by both liquid and gas flowrates, liquid physical properties and bed characteristics. In the dissertation of Joubert (2009), a review of the principal published works on the L/S mass transfer in TBRs is given. In this work, the author highlights the

fact that this parameter is strongly affected by the operating history of the packed bed. Multiple hydrodynamic states are common in TBRs; the two extreme operating modes for a TBR are defined as the *Levec mode* (lower leg in Fig. 9), which is obtained flooding the packed bed of dry particles for several hours, then draining it and increasing gas and liquid flowrate to the operating values, and the *Kan-liquid mode* (upper leg in Fig. 9), obtained, after having flooded and drained the bed, increasing gas flowrate to the operating value and the liquid flowrate to a value higher than that of transition between trickle and pulse flow for some minutes, then decreasing it to the operating value.

Among all the correlations for the $k_{LS}a$ described by Joubert (2009), Ramachandran and Chaudhari (1983) and Gianetto and Silveston (1986), we report only some of them. Van Krevelen and Krekels (1948) correlated their data about the dissolution in water of benzoic acid particles from 3 to 14.5 mm with the following expression, valid for $0.013<\mathrm{Re}_L{}'<12.6$:

$$\frac{k_{LS}a_P}{Da_t^2}=1.8\left(\mathrm{Re}_L'\right)^{1/2}\left(\frac{\mu_L}{\rho_L D}\right)^{1/3}$$
$$\mathrm{Re}_L'=\frac{\rho_L u_L}{\mu_L a_t}$$
$$a_t=\frac{6\left(1-\varepsilon_B\right)}{d_P*} \qquad (28)$$
$$d_P*=\frac{d_P}{1+\dfrac{4d_P}{6d_R(1-\varepsilon_B)}}$$

Dharwadkar and Sylvester (1977) correlated data of various previous works with the following correlation, valid for $0.2 < \mathrm{Re}_L < 2400$, i.e. in trickle, pulse and dispersed bubble flow regimes as the authors reported:

$$k_{LS}=1.637u_L\,\mathrm{Re}_L^{-0.331}\,\mathrm{Sc}^{-0.666} \qquad (29)$$

They said that from the literature data correlated, no appreciable increase of k_{LS} with gas velocity can be noted.

Rao and Drinkenburg (1985) correlated their experimental k_{LS} data in the trickle flow regime with the following:

$$\eta_{CE}\left(\frac{k_{LS}d_P{}'}{D}\right)=0.24\,\mathrm{Re}_L{}'^{\,0.75}\,\mathrm{Sc}^{1/3}$$
$$\mathrm{Re}_L{}'=\frac{\rho_L u_L d_p{}'}{\varepsilon_L\mu_L} \qquad (30)$$

where $d_p{}'$ (m) is the diameter of a sphere with the same external surface of the particle considered.

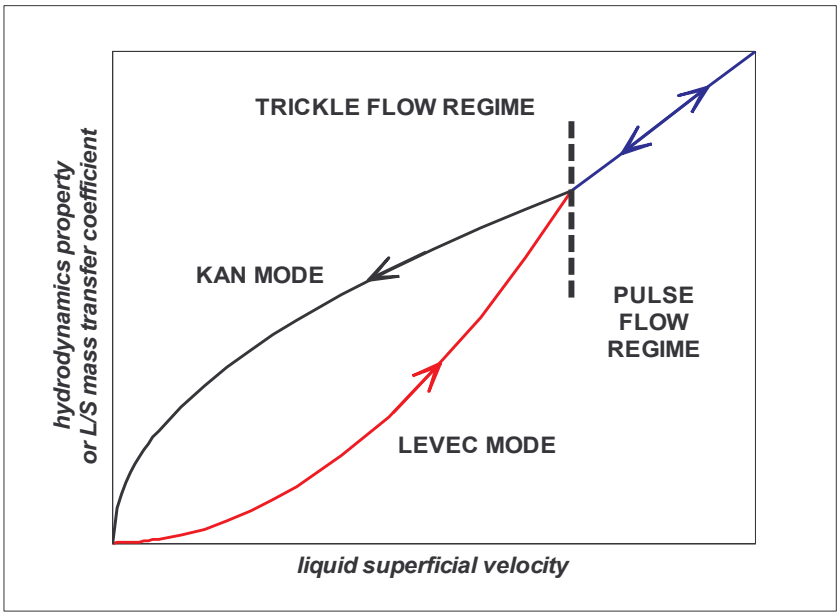

Fig. 9. Hysteresis loops for hydrodynamics or mass transfer parameters due to trickle flow multiplicity.

They noticed that effect of gas velocity on k_{LS} was significant for u_G approximately higher than 10 cm/s; since they measured the product η_{CE}·Sh$'$ and not only Sh$'$, the increase of η_{CE}·Sh$'$ with increasing gas flowrate, could have been due either to an enhancement of the spreading of liquid, that enhances the wetting efficiency η_{CE}, or to an increase of the k_{LS} coefficient, or to an increase of both of them. If it is now well accepted that η_{CE} increases with u_G, as reported in Section 2.4, not the same we can say for k_{LS} (Lakota and Levec, 1990); by the way, a recent experimental study of Highfill and Al Dahhan (2001) on the effect of pressure and gas flowrate on L/S mass transfer coefficient showed that k_{LS} increases with pressure and gas superficial velocity, especially at high gas and liquid throughput, as the G/L mass transfer coefficient does (see Section 2.6) and according to the five limiting cases of Al Dahhan and Dudukovic (1995), described in Section 2.2. They didn't propose a correlation for their data.

Rao and Drinkenburg (1985) to take into account the effect of the gas velocity in their correlation, used a modified Re number, which contains a dependence on the liquid hold-up which, from what reported in Section 2.3, decreases with increasing gas flowrate.

Finally, we report the correlation of Lakota and Levec (1990), derived for cylindrical particle of equivalent diameter of 5.45 mm (defined as 6 times the ratio volume to surface of particle), d_p/d_R = 0.03, 0.07 < u_L < 4.3 cm/s, 0.25 < u_G < 24.5 cm/s, which correlates k_{LS} data in trickle, pulse and dispersed bubble flow regimes. This correlation is valid in the range 15 < $(\mathrm{Re}_{L,m}\varepsilon_B)/\varepsilon_{L,d}$ < 600:

$$\frac{k_{LS}d_P\varepsilon_B}{D(1-\varepsilon_B)} = 0.487\left(\frac{\mathrm{Re}_{L,m}\,\varepsilon_B}{\varepsilon_{L,d}}\right)^{0.495}\mathrm{Sc}^{1/3} \qquad (31)$$

Here again, the effect of the gas velocity is visible by means of the modified Re_L; increasing the gas velocity, the dynamic liquid hold-up decreases and thus the k_{LS} increases, as observed experimentally by Lakota and Levec (1990) in each flow regime.

We underscore that none of the correlations presented has been derived for high pressure TBR, as reported by Highfill and Al Dahhan (2001).

From the comparison of the predictions of some correlations and their experimental trend of k_{LS}, Highfill and Al Dahhan (2001) concluded that the correlation of Lakota and Levec (1990) is among those which best represent the experimental results, even if the agreement is not completely satisfactorily.

In Tab. 11 we report the values of $k_{LS}a$ predicted by the four correlations presented for both systems described in Section 2.6; for this parameter, the degree of agreement among different correlations is higher than for k_La, with the correlation of Rao and Drinkenburg giving a lower estimate of $k_{LS}a$.

Tab. 11. Values of $k_{LS}a$ (s^{-1}) from correlations for the laboratory TBR considered.

liquid and gas velocity (cm/s)	Van Krevelen and Krekels (1948)	Dharwadkar and Sylvester (1977)	Rao and Drinkenburg (1985)	Lakota and Levec (1990)
$u_L = 0.05$ $u_G = 5$	6.9	5.4e-1	8.1e-2	3.0
$u_L = 0.025$ $u_G = 2$	4.9	3.4e-1	6.4e-2	2.4

2.8 Liquid distribution

In the article of Møller at al. (1996), an interesting study on the distribution of the liquid phase in a TBR is presented. Liquid radial distribution in TBR is often non-ideal, especially in small-scale and pilot TBRs where low liquid flowrates are used, and can lead to non-uniform wetting of the catalyst, which results in a loss of catalyst utilization or, especially for exothermic reactions or side reactions that deposit by-products on the particles, to hot spots and rapid deactivation of the bed.

Møller at al. (1996) showed that liquid distribution on the section of the TBR is significantly improved by flooding it before operation. Same effect can be obtained using a high liquid velocity for a limited time interval. The insertion of a top layer of larger particles also contributes to enhance the liquid distribution, especially when the liquid distributor is not effective.

The empirical criterion $d_R/d_p \geq 20$ is used to check if the liquid distribution is good and uniform (Al Dahhan and Dudukovic, 1996). Usually for industrial and pilot-scale reactors, this condition is fulfilled, but when operating on a bench-scale trickle-bed reactor, for which typical bed diameters are between 1 and 3 cm, and using catalyst particles of the size used in commercial reactors (few

mm of equivalent diameter) the previous condition is difficult to met (Al Dahhan and Dudukovic, 1996). The technique of bed dilution with fines described in Section 2.5 is helpful in obtaining a better liquid distribution, thus avoiding channelling and incomplete wetting even at low u_L.

2.9 Selection of correlations

A primary criterion in the selection of the correlations to use in the reactor model has been that of preferring correlations developed for TBR at high pressure, which include the effect of pressure and gas velocity on the predicted parameter. To this purpose, the work of Al Dahhan et al. (1997) can be considered as a guide in the research of such correlations, both for hydrodynamics and mass transfer parameters. Most of the correlations reported in the classical literature and reviewed by Shah (1979), Ramachandran and Chaudhari (1983) and Gianetto and Silveston (1986), do not contain an explicit dependence on pressure, due to the fact that they have been derived on experiments in atmospheric TBR. Others contain a dependence on pressure for the presence of parameters such as liquid holdup, wetting efficiency, gas density that directly depend on it, even if the authors didn't mean to study this dependence. An exhausting discussion has been made on G/L mass transfer coefficient, and for this parameter correlation of Ellman (1988) and Fukushima and Kusaka (1977) have been chosen, both of which include a dependence on p and u_G which respects the 5 limiting cases of Al Dahhan and Dudukovic (1995).

All the graphs reported in this section refer to the gas-liquid system used in the simulation, which is pure H_2 as gas phase and solution of sugar L-arabinose at 100°C; when the effect of gas and liquid velocity is studied, pressure was kept at 40 bar, while when the effect of pressure and gas velocity was considered, liquid superficial velocity was set to 0.05 cm/s. General information on the TBR considered for the evaluation of the correlations are given in Tab. 12.

Tab. 12. General characteristics of TBR simulated, necessary to use the correlations.

TBR characteristics	values
d_R (mm)	10
d_{pi} (mm)	0.2
d_p (mm)	1
ε_B (-)	0.25
u_L (cm/s)	0.01-0.1
u_G (cm/s)	0.1-10

Starting from the two-phase pressure drop, both phenomenological models on the effect of pressure and gas velocity on the mass transfer and hydrodynamics parameters described above predict two different behaviours of pressure drop, depending on the value of the gas superficial velocity. For u_G lower than 2 cm/s, pressure drop doesn't show a significant variation with pressure; while, for u_G > 2cm/s, the higher the gas velocity, the stronger the pressure effect on pressure drop, due to the increased shear (or momentum transfer) at the G/L interface. Pressure drop always increases with liquid superficial velocity, at constant gas velocity and pressure, and the effect of gas velocity increases with liquid superficial velocity. Fig. 10 report the trends of two-phase pressure drop as predicted by the correlation of Larachi et al. (1991a) developed for trickle flow in a TBR at high pressure, which has been used in the reactor models. The range of liquid and gas velocity investigated are typical for a small scale TBR, as reported in Ramachandran and Chaudhari (1983). The behaviours just described are well represented. It is noteworthy that the pressure drop for u_G = 5cm/s, $u_L \leq$ 0.1cm/s and a typical laboratory trickle-bed with the characteristics in Tab. 12 and length of almost 30 mm, is around 200mbar, i.e. 0.5% of the total pressure; thus inside the reactor the partial pressure of H_2 is practically uniform.

Total liquid hold-up has been calculated in the reactor model through the correlation of Larachi et al. (1991a), since it has been derived on data gathered on high pressure TBR, and it takes into account the effect of liquid and gas velocity, as well as pressure. As reported in Larachi et al. (1991) and in Al Dahhan et al. (1997), the trend predicted agrees with the 5 limiting cases of Al Dahhan and Dudukovic (1995). In Fig. 11a, the dependence of ε_L on pressure and gas superficial velocity is reported: ε_L decreases when gas velocity increases, due to the stronger drag effect that gas phase has on the trickling liquid film, reducing its thickness. In particular, the gas velocity effect on ε_L, at the same pressure and u_L, is evident especially for u_G < 5cm/s, while the effect of pressure is practically negligible for the system considered. In Fig. 11b we see that the larger the liquid velocity, the higher the liquid hold up inside the reactor.

It is worth highlighting that both correlations for pressure drop and liquid hold up have been derived upon 1500 experimental data points obtained on a large variety of gas-liquid systems, including viscous, weakly foaming and foaming systems.

The correlation of Al Dahhan and Dudukovic (1995) has been used to estimate the contacting efficiency between liquid and catalyst. This correlation has been derived and tested by the authors on data at high pressure (0.31-5 MPa). As described above, η_{CE} depends on pressure and gas velocity in a similar way as the pressure drop does. In Fig. 12a the trend of η_{CE} against gas superficial velocity at different pressures is shown, and it appears that effect of u_G is stronger than pressure effect, and for u_G < 2-5cm/s, the latter effect on η_{CE} is negligible; however, both effects are much less evident than the effect of liquid velocity, as we can see from Fig. 12b, where η_{CE} increases much more significantly with u_L. In general the correlation predicts an excellent external wetting, mainly due to the dilution with fines that improves the hydrodynamics in the bed.

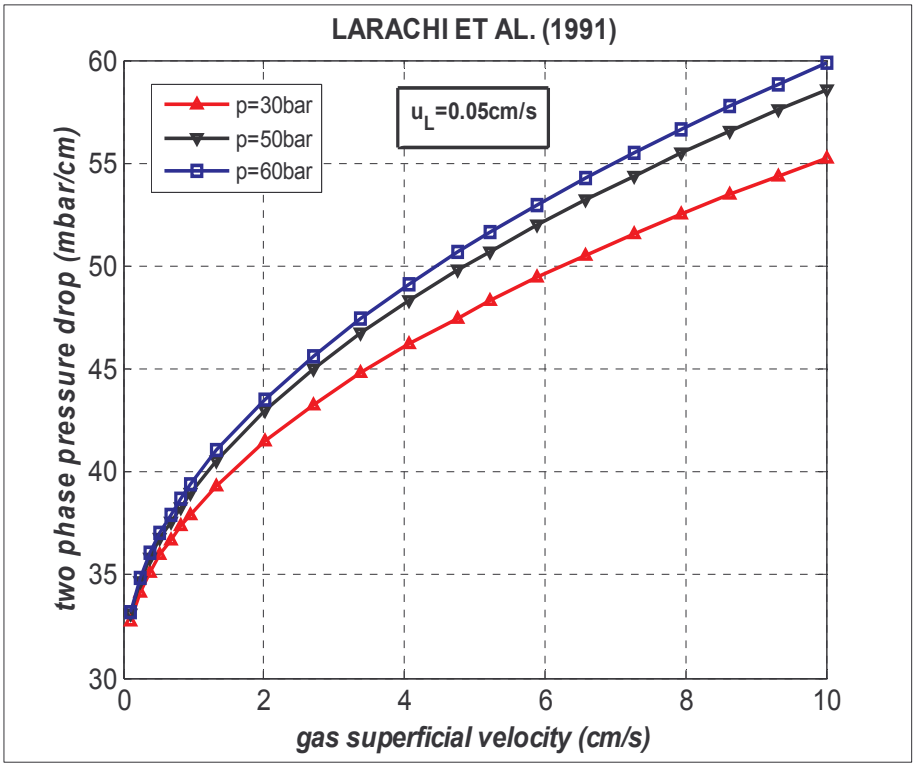

a)

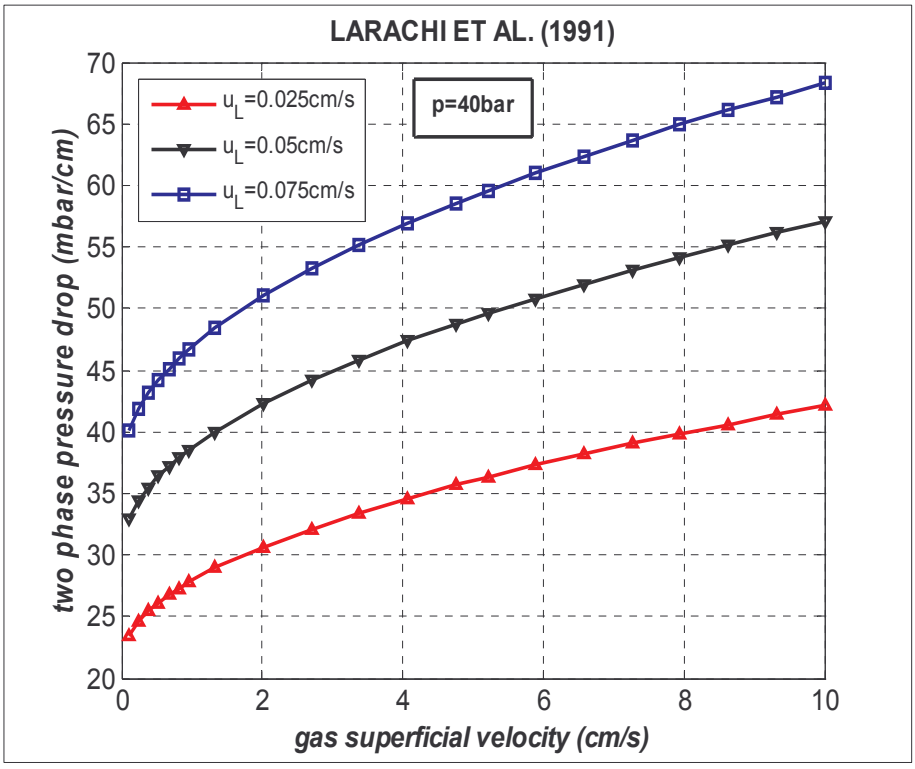

b)

Fig. 10. Trends of pressure drop in trickle bed (a) effect of gas superficial velocity and pressure, b) effect of gas and liquid superficial velocities).

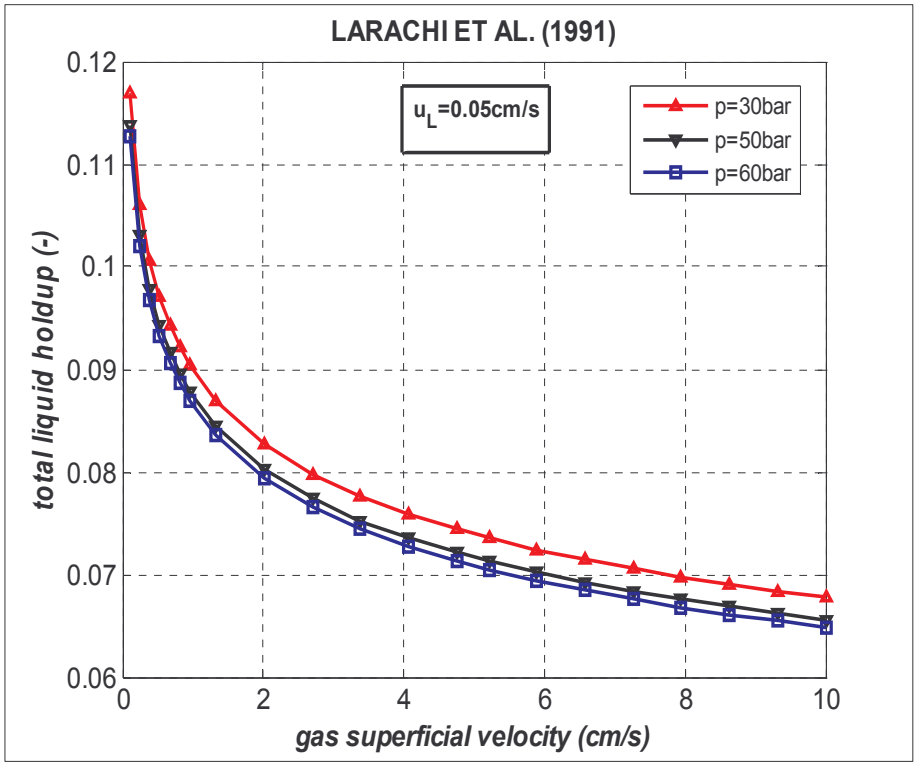

a)

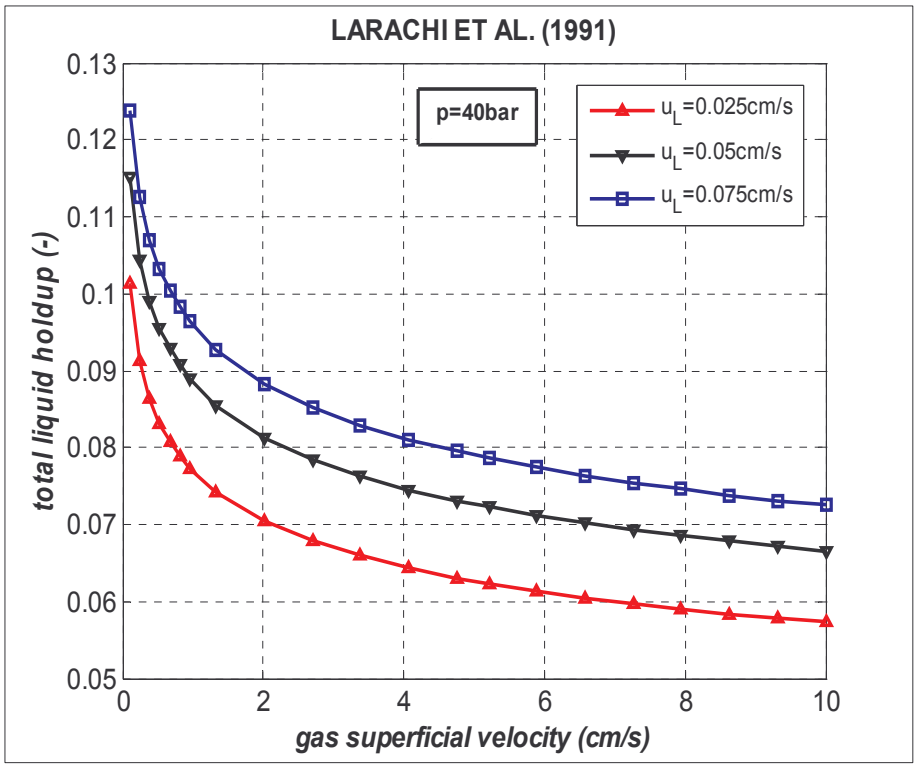

b)

Fig. 11. Trends of liquid holdup (a) effect of gas superficial velocity and pressure, b) effect of gas and liquid superficial velocities).

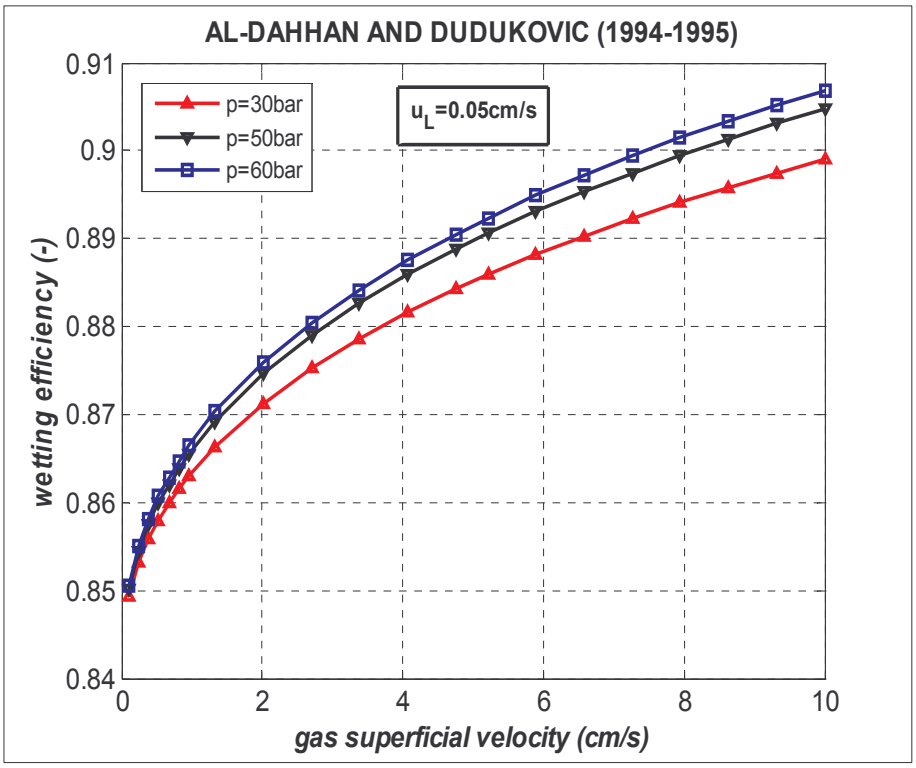

a)

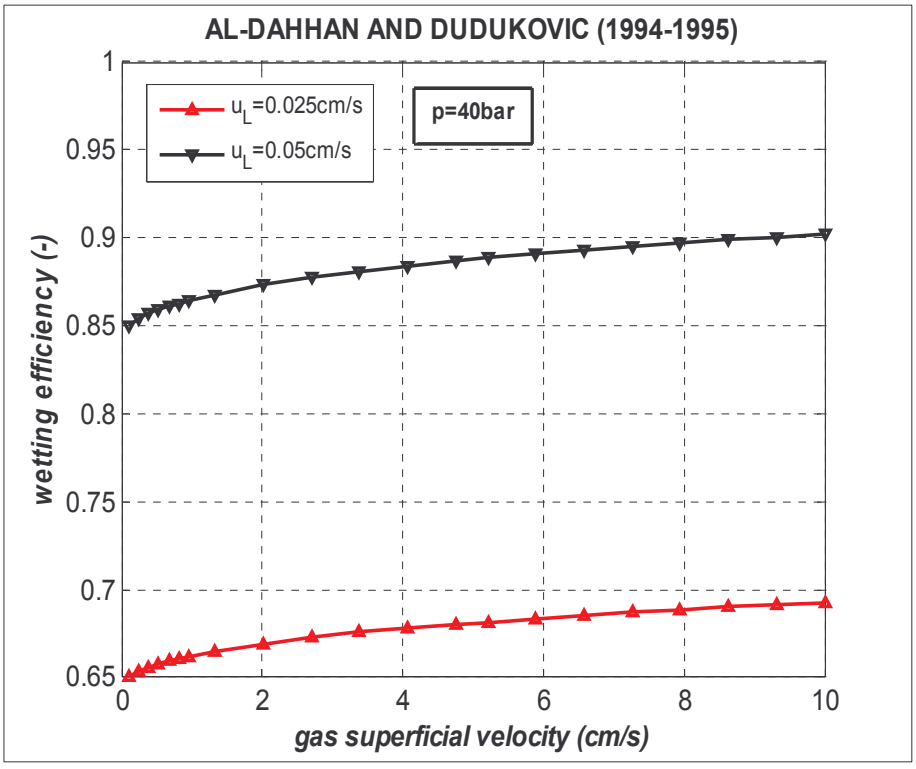

b)

Fig. 12. Trends of wetting efficiency (a) effect of gas superficial velocity and pressure, b) effect of gas and liquid superficial velocities).

Finally, the L/S mass transfer coefficient has been calculated by means of the Lakota and Levec correlation (1990), which has not been derived at high pressure. However, it can predict at least the effect of liquid and gas flowrates on $k_{LS}a$; it has been ascertained that increasing liquid velocity, L/S mass transfer improves. As reported by Highfill and Al Dahhan (2001), L/S mass transfer is enhanced also by increasing gas velocity, both for the better spreading of liquid on the catalyst surface and for the higher local turbulence created by gas phase.

Using the Specchia and Baldi correlation (1977) for the dynamic liquid hold-up that appears in the Lakota and Levec (1990), it is possible to take into account also the effect of pressure and gas velocity, since it contains a dependence on the two-phase pressure drop in the form:

$$\varepsilon_{L,d} \propto \left(\frac{\Delta p_{GL}}{z} \right)^{-0.42} \tag{32}$$

Therefore increasing the pressure, i.e. gas density, two-phase pressure drop increases and liquid hold up decreases according to Eq. (32). For the particular operating conditions tested, the influence of pressure on L/S mass transfer coefficient is quite faint, while in Fig. 13 it is evident that liquid velocity has a stronger effect than gas velocities.

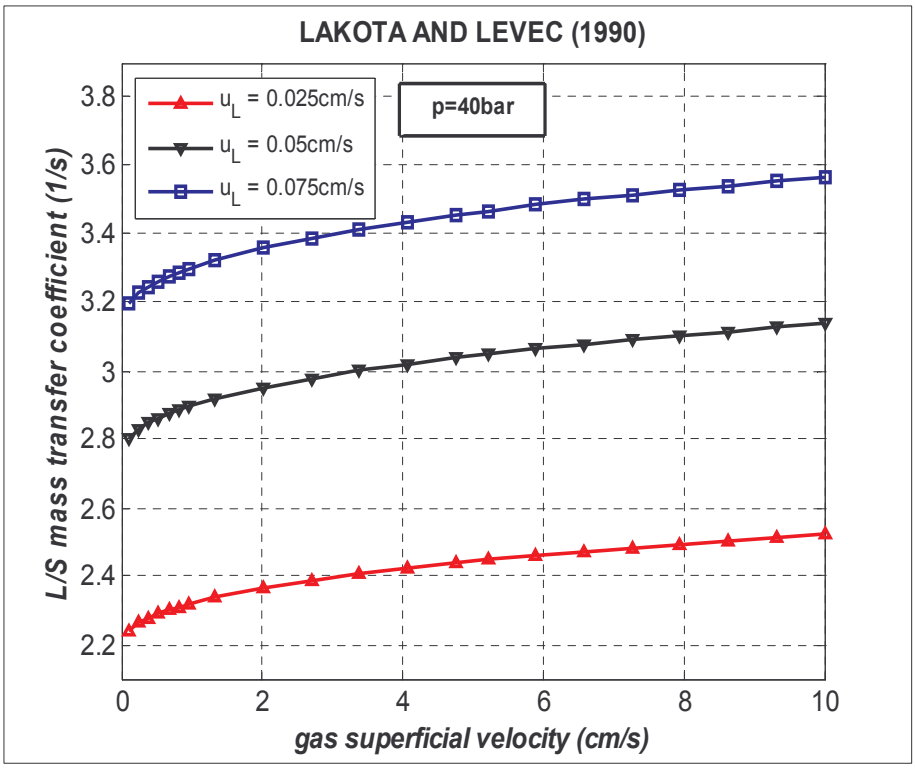

Fig. 13. Trend of L/S mass transfer coefficient from correlation of Lakota and Levec (1990) with gas superficial velocity and liquid superficial velocity.

Capitolo 3

Metodo numerico:

metodo delle linee (NUMOL)

In questo capitolo vengono presentate le principali caratteristiche del metodo numerico delle linee (NUMOL), utilizzato per la risoluzione dei sistemi di equazioni differenziali alle derivate parziali risultanti dalla scrittura dei bilanci di specie chimica e di energia sul reattore.

Nel metodo delle linee, il dominio spaziale è discretizzato e le derivate spaziali sono approssimate con opportuni schemi (differenze finite centrate, upwind), mentre le derivate temporali sono mantenute tal quali; il sistema di PDE è pertanto trasformato in un sistema di ODE, una per ogni intervallo spaziale. Tale sistema può essere integrato numericamente mediante un integratore ODE ottenendo l'evoluzione temporale della variabile dipendente in ogni intervallo spaziale.

Tale procedimento numerico può essere utilizzato anche per risolvere problemi stazionari, mediante il cosiddetto "metodo dei falsi transienti".

Le scelte principali da operare per definire un codice NUMOL riguardano lo schema di discretizzazione delle derivate spaziali e l'integratore ODE. Le due principali fonti di errore di un metodo NUMOL sono relative all'ordine di accuratezza dello schema di discretizzazione usato per le derivate spaziali e alla tolleranza imposta all'integratore ODE.

Il metodo delle linee può essere integrato con un algoritmo di adattamento della griglia, che permette di modificare la posizione dei nodi interni durante la risoluzione, seguendo il trend della soluzione, ovvero concentrando i nodi laddove la soluzione presenta larghi gradienti. Alla fine del capitolo è riportata una breve descrizione dei due metodi di raffinamento più comuni.

Chapter 3

Numerical method:

method of lines (NUMOL)

The purpose of this chapter is that of presenting the main features of the numerical method of lines, a computational tool that can be applied to solve a broad range of problems in the engineering field. It is particularly suitable for solving PDE problems, such those that arise from the modelling of dynamic continuous tubular reactors. In these cases, we are interested in both the time profiles and spatial distributions of dependent variables.

We adopt the following convention to present the time derivatives and spatial derivatives, which is the one used by Schiesser (1991):

$$\begin{aligned} \phi_t &= \frac{\partial \phi(\vec{x},t)}{\partial t} \\ \phi_x &= \frac{\partial \phi(\vec{x},t)}{\partial x} \\ \phi_{xx} &= \frac{\partial^2 \phi(\vec{x},t)}{\partial x^2} \end{aligned} \tag{33}$$

where ϕ is a generic dependent variable.

The chapter is structured in the following way: first of all a brief introduction of the NUMOL is given, then spatial differentiation is taken into account, followed by some concepts relative to initial-value integration.

3.1 Introduction to the Numerical Method of Lines

Let's consider a 1-dimensional, dynamic PDE to fix the ideas. The usual approach to the numerical solution of systems of PDEs is that of the finite difference, finite elements or finite volume

methods. These methods require to discretize the spatial and time domain, creating a grid of nodes *x(i)* and *t(j)*, where *i* could vary from 1 to N and so *j*. In this way, the partial derivatives can be approximated with suitable discretization schemes to algebraic expressions, and the initial system of PDEs is transformed in a system of algebraic equations, that can be solved with appropriate solvers.

In the NUMOL spatial derivatives are still discretized in the spatial grid, while time derivatives are kept, leading to a system of differential equations (one for each spatial interval) in only one independent variable, which is *t*, and so the initial PDE problem is reduced to an ODE problem. This system can then be numerically integrated by means of a ODE integrator to obtain for each spatial interval the time evolution of the dependent variable. Fig. 14 well explains this methodology and the origin of the name NUMOL.

The most important steps in the definition of a NUMOL code are the choice of a suitable discretization scheme for spatial derivatives, the choice of an appropriate ODE integrator and the setting of its main properties (time span, tolerances).

A simplified overall structure of a NUMOL code for the solution of a system of PDEs is reported in Fig. 15.

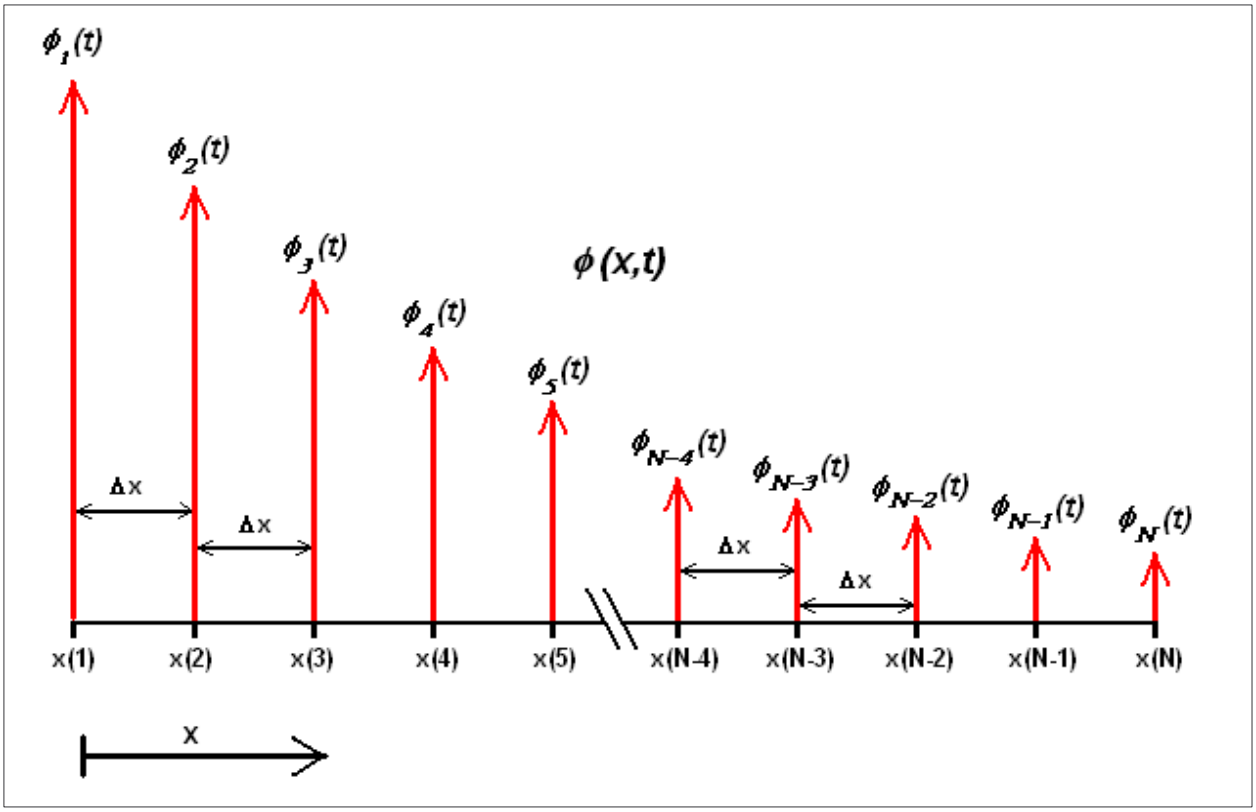

Fig. 14. Spatial discretization and numerical integration in the time for the generic function ϕ (x,t).

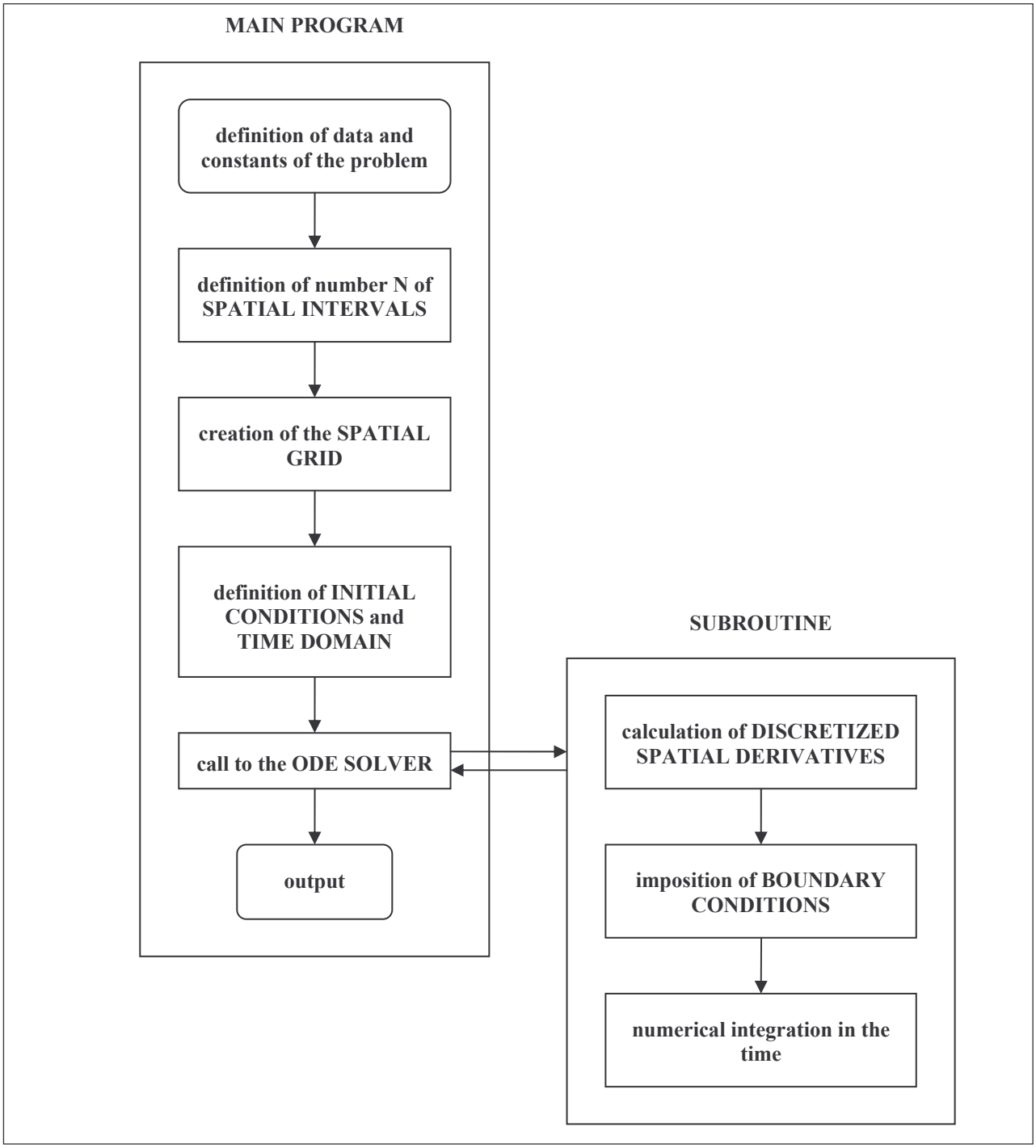

Fig. 15. Overall structure of a NUMOL code.

The NUMOL is not only suitable to solve 1-dimensional parabolic PDEs, which arise from dynamic problems, but also steady-state problems in more than one spatial independent variable, applying the so-called "*method of false transients"* (Schiesser, 1991); let's suppose we are interested in solving the steady-state diffusion-reaction equation in a spherical pellet, considering only the variation of concentration along the particle radius. This is a 1-dimensional non-dynamic PDE (for simplicity let's consider a 1st order irreversible kinetics A→ products):

$$\begin{aligned} &\frac{D_{eff,A}}{r^2}\frac{\partial}{\partial r}\left(r^2\frac{\partial c_A}{\partial r}\right)-R=0 \\ &R=kc_A \\ &c_A(r=R_P)=c_A^{\,s} \\ &\frac{\partial c_A}{\partial r}(r=0)=0 \end{aligned} \tag{34}$$

where r (m) is the radial coordinate, c_A (mol/m^3) is the concentration of the generic reactant A (our dependent variable), $D_{eff,A}$ (m^2/s) the effective mass diffusivity coefficient in the spherical particle, R (mol/m^{3}s) the reaction rate, k (1/s) the kinetic constant, R_P (m) is the particle radius and notation s means "at the surface of the catalyst pellet". The "*method of false transients*" consists in creating a fictitious dependence on t, initial-value independent variable, in the dependent variable c_i, defining a generic initial-value condition, whose effect for long t is negligible, and transforming the initial PDE in a parabolic PDE:

$$\frac{\partial c_A}{\partial t}=\frac{D_{eff,A}}{r^2}\frac{\partial}{\partial r}\left(r^2\frac{\partial c_A}{\partial r}\right)-R \tag{35}$$

In Fig. 16 are reported the evolution in the time of the concentration profile of A inside the particle obtained from a NUMOL code and the comparison between the steady state concentration profile from analytical solution (Salmi et al., 2010), which is given by

$$\begin{aligned} &c_A=c_A^{\,s}\frac{R_p}{r}\frac{\sinh\left(\phi\dfrac{r}{R_p}\right)}{\sinh(\phi)} \\ &\Phi=R_p\left(\frac{k}{D_{eff,A}}\right)^{1/2} \end{aligned} \tag{36}$$

where Φ (-) is the Thiele modulus, and the same profile from the NUMOL.

In this simulation (conducted in *MatLab 7.1*) the initial condition imposed was a very trivial one, $c_A(r,0)=1$, the concentration at the surface of the catalyst particle was 10 mol/m^3, time span was 600 s and the spatial domain was divided in N=51 intervals. In Fig. 16a we can see that already after a time interval of approximately 400 seconds, the solution has reached a steady state profile and is no more influenced by the initial condition. Fig. 16b shows that the level of agreement between the NUMOL and the analytical solutions is excellent.

One last aspect of the NUMOL that we will treat in more detail in the following sections, is how to increase the NUMOL solution accuracy, which requires to investigate which are the main error sources in a NUMOL code. We commit essentially two types of approximations, the 1st one due to the discretization of the spatial derivatives. The narrower the spatial interval, the more accurate the approximation of the exact solution that we obtain from the NUMOL. The higher the order of

accuracy of the discretization scheme adopted to approximate the spatial derivatives, the more accurate the solution. In both cases, we pay this increase of accuracy in term of higher computational effort, which in the 1st case is due to the increase in the number of ODEs to solve (n° intervals x n° PDEs), while in the 2nd to the higher complexity of the differentiation formula. The 2nd approximation made by NUMOL is the numerical integration of the ODEs, the accuracy of which can be defined through the tolerances of the ODE solver. Also here, the tighter the tolerance, the more accurate the solution, but the higher the computational effort required.

3.2 Spatial differentiation

The algebraic approximation of the spatial derivatives of a PDE is one of two fundamental steps in the NUMOL solution and it is therefore one of the sources of error of the numerical solution. In this section we briefly see how we can construct a discretization scheme and some of the most used differentiation formulas.

Let's consider the variation of a dependent variable *u* along the *x* direction, assuming here that *u* is a function of only one spatial independent variable. Let's assume it can vary as a polynomial in *x* (Schiesser, 1991):

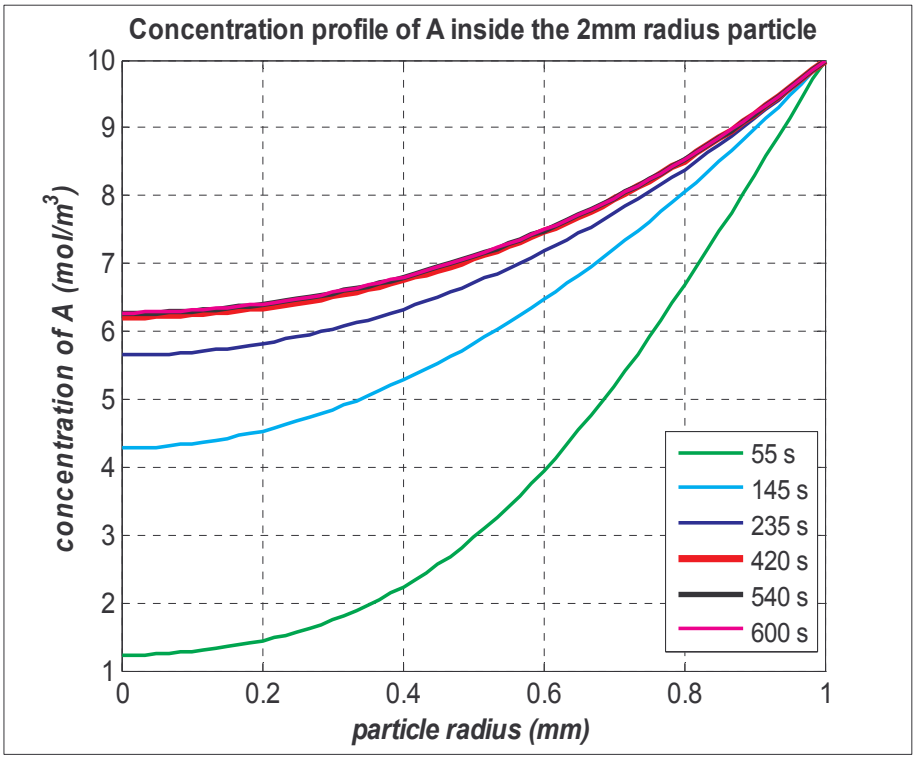

a)

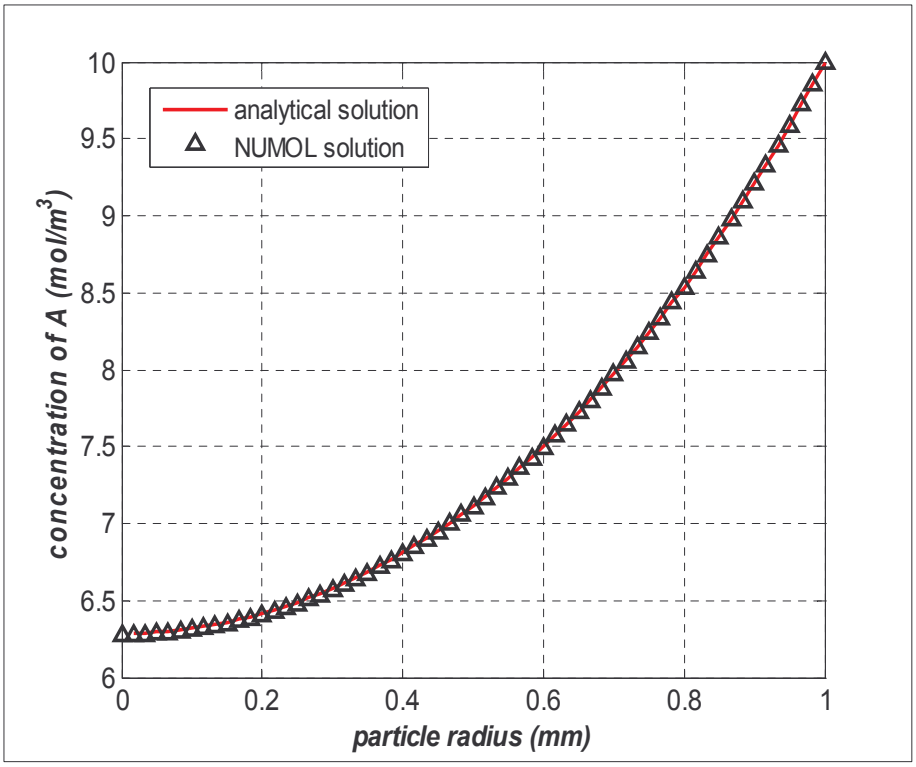

b)

Fig. 16. Solution of steady state diffusion-reaction equation in a catalyst particle (a) evolution of the NUMOL solution in the time, b) comparison between analytical and numerical concentration profile).

$$u(x) = a_0 + a_1(x - x_i) + a_2(x - x_i)^2 + a_3(x - x_i)^3 + \ldots \tag{37}$$

where x_i is a generic point in the x direction and a_i, $i=1 \ldots N$, are coefficients to be determined. In general they have the following form:

$$a_n = \frac{1}{n!}\frac{d^n u}{dx^n}(x_i) \tag{38}$$

and thus the polynomial approximation of $u(x)$ is the Taylor series expansion of $u(x)$ around x_i.

3.2.1 Second order differentiation formula for first derivative

Fornberg (1988) published an algorithm to derive differentiation matrix for any order of derivative and to any order of accuracy on a arbitrary spaced grid, i.e. not necessary uniformly spaced. In the following we derive and present the most common differentiation formulas based on uniform grid.

We now derive a 2nd order differentiation formula to approximate the 1st derivative of u in x_i. Let's consider a uniform grid in x, such that every node has a distance of Δx from its adjacent nodes, and write a Taylor series for u in x_{i+1} and x_{i-1}:

$$u(x_{i+1}) = u(x_i) + u_x(x_i)\Delta x + \frac{u_{xx}(x_i)}{2!}\Delta x^2 + \frac{u_{xxx}(x_i)}{3!}\Delta x^3 + \ldots \tag{39}$$

$$u(x_{i-1}) = u(x_i) - u_x(x_i)\Delta x + \frac{u_{xx}(x_i)}{2!}(-\Delta x)^2 - \frac{u_{xxx}(x_i)}{3!}\Delta x^3 + \ldots \tag{40}$$

Let's subtract Eq. (40) from Eq. (39) and explicit $u_x(x_i)$:

$$u_x(x_i) = \frac{u(x_{i+1}) - u(x_{i-1})}{2\Delta x} + \frac{u_{xxx}(x_i)}{3!}\Delta x^2 = \frac{u(x_{i+1}) - u(x_{i-1})}{2\Delta x} + \mathrm{O}(\Delta x^2) \tag{41}$$

This is the second order central finite difference approximation for the 1st derivative in $u_x(x_i)$. The term central refers to the fact that in order to evaluate $u_x(x_i)$, information is taken both upwind, in x_{i-1}, and downwind, in x_{i+1}. This formula can be used to calculate $u_x(x_i)$ in the internal nodes, i.e. $i=2,3,\ldots,N-2,N-1$, while for the boundary nodes different formulas must be used, to avoid recourse to fictitious points x_0 and x_{N+1}. Let's derive both of them, first for boundary node x_1 and then for x_N. Let's evaluate $u(x_2)$ and $u(x_3)$ from a Taylor expansion centred in x_1:

$$u(x_2) = u(x_1) + u_x(x_1)\Delta x + \frac{u_{xx}(x_1)}{2!}\Delta x^2 + \frac{u_{xxx}(x_1)}{3!}\Delta x^3 + \ldots \tag{42}$$

$$u(x_3) = u(x_1) + u_x(x_1)2\Delta x + \frac{u_{xx}(x_1)}{2!}(2\Delta x)^2 + \frac{u_{xxx}(x_1)}{3!}(2\Delta x)^3 + \ldots \tag{43}$$

By multiplying Eq. (42) by 4, then subtracting (43), and explicating $u_x(x_1)$, we obtain:

$$u_x(x_1) = \frac{-3u(x_1) + 4u(x_2) - u(x_3)}{2\Delta x} + \mathrm{O}(\Delta x^2) \tag{44}$$

which is a 2nd order forward (or downwind) finite difference approximation of $u_x(x)$. If we write similar approximations for $u(x_{N-2})$ and $u(x_{N-1})$ and execute the same operations on them, we obtain the 2nd order backward (upwind) differentiation formula for $u_x(x_N)$:

$$u_x(x_N) = \frac{3u(x_N) - 4u(x_{N-1}) + u(x_{N-2})}{2\Delta x} + \mathrm{O}(\Delta x^2) \tag{45}$$

Equations (41), (44) e (45) can be used to calculate the 1st order spatial derivative of u in each node of the grid. Matrix form of Eqs. (41), (44) and (45) is:

$$\overline{u_x}(x_i) = \frac{1}{2\Delta x}\begin{bmatrix} -3 & 4 & -1 \\ -1 & 0 & 1 \\ 1 & -4 & 3 \end{bmatrix}\bar{u} + O(\Delta x^2) \tag{46}$$

where the 3x3 matrix is called differentiation matrix.

Let's now evaluate what is the meaning of "second order" and in which cases these differentiation formulas are not exact. If we assume that $u(x)$ vary as a 1st or 2nd order polynomial in x, its derivatives will be respectively:

$$\frac{du(x)}{dx} = \frac{d}{dx}\left(a_0 + a_1 x\right) = a_1$$
$$\frac{du(x)}{dx} = \frac{d}{dx}\left(a_0 + a_1 x + a_2 x^2\right) = a_1 + 2a_2 x \tag{47}$$

One could check that applying Eqs. (41), (44) e (45), the same results are obtained. So these differentiation formulas do not commit any error in the derivation of the 1st derivative of such functions. This is due to the fact that in deriving Eqs. (41), (44) and (45), only the 3rd and higher order derivatives of the function contribute to the final result; since linear functions and 2nd order polynomials has zero 3rd and higher order derivatives, there is no contribution from these higher order derivatives to $u_x(x_i)$. The contribution of these higher order derivatives of $u(x_i)$ is evident in the $O(\Delta x^2)$ term.

To confirm this, let's suppose that $u(x)$ varies as a 3rd order polynomial and derive the exact 1st order derivative and its approximation given by Eq. (41):

$$\frac{du(x)}{dx} = \frac{d}{dx}\left(a_0 + a_1 x + a_2 x^2 + a_3 x^3\right) = a_1 + 2a_2 x + 3a_3 x^2 \tag{48}$$

$$\frac{du(x_i)}{dx} = \frac{\left(a_0 + a_1\left(x_i + \Delta x\right) + a_2\left(x_i + \Delta x\right)^2 + a_3\left(x_i + \Delta x\right)^3\right)}{2\Delta x} + \\ - \frac{\left(a_0 + a_1\left(x_i - \Delta x\right) + a_2\left(x_i - \Delta x\right)^2 + a_3\left(x_i - \Delta x\right)^3\right)}{2\Delta x} + \mathrm{O}(\Delta x^2) = a_1 + 2a_2 x + 3a_3 x^2 + a_3 \Delta x^2 \tag{49}$$

Here the differentiation formula commits an error in the estimation of the 1st derivative, due to the fact that the 3rd order derivative for a 3rd order polynomial is not zero and so the $O(\Delta x^2)$ term gives a contribution. The interesting thing is that the error goes with Δx^2, which means that reducing the size of the spatial intervals, error decreases, and this is a justification to what we anticipated in the previous section. The price we have to pay to gain accuracy is more computation effort, since higher number of intervals means higher number of ODEs to be solved.

We must point out that the discussion made so far is based on polynomials, but in general the solution of a PDE does not vary along x as a polynomial. By the way, as it is highlighted in Schiesser (1991), experience has demonstrated that the latter conclusion about the error of the discretization formula is commonly valid.

Another possibility to increase the accuracy of the NUMOL solution is to use a higher order differentiation formula.

3.2.2 Fourth order differentiation formula for first derivative

To obtain a differentiation formula of higher accuracy than the previous one, based on 3 points, we could use 5 points, that is x_i, two points upwind, x_{i-2} and x_{i-1}, and two downwind, x_{i+1} and x_{i+2}, and write for x_{i-2}, x_{i-1}, x_{i+1} and x_{i+2} a Taylor expansion of $u(x)$ around x_i:

$$u(x_{i-2}) = u(x_i) - u_x(x_i)2\Delta x + \frac{u_{xx}(x_i)}{2!}(-2\Delta x)^2 - \frac{u_{xxx}(x_i)}{3!}(2\Delta x)^3 + \ldots \tag{50}$$

$$u(x_{i-1}) = u(x_i) - u_x(x_i)\Delta x + \frac{u_{xx}(x_i)}{2!}(-\Delta x)^2 - \frac{u_{xxx}(x_i)}{3!}\Delta x^3 + \ldots \tag{51}$$

$$u(x_{i+1}) = u(x_i) + u_x(x_i)\Delta x + \frac{u_{xx}(x_i)}{2!}\Delta x^2 + \frac{u_{xxx}(x_i)}{3!}\Delta x^3 + \ldots \tag{52}$$

$$u(x_{i+2}) = u(x_i) + u_x(x_i)2\Delta x + \frac{u_{xx}(x_i)}{2!}(2\Delta x)^2 + \frac{u_{xxx}(x_i)}{3!}(2\Delta x)^3 + \ldots \tag{53}$$

The objective is as before to explicit $u_x(x_i)$ and to drop as many as possible of the higher order derivatives to gain maximum accuracy. A systematic procedure to do this is presented in Schiesser (1991) and it consists in making a linear combination of Eqs. (50), (51), (52) and (53), multiplying them respectively for coefficients a, b, c and d and requiring that the coefficient of the 1st derivative $u_x(x_i)$ will be 1, while those of higher order derivatives ($u_{xx}(x_i)$, $u_{xxx}(x_i)$ and $u_{xxxx}(x_i)$) be 0. From these 4 constraints we can obtain the values of the 4 coefficients which are:

$$a = \frac{2}{4!}, b = -\frac{16}{4!}, c = \frac{16}{4!}, d = -\frac{2}{4!} \tag{54}$$

If we put in evidence $u_x(x_i)$ from the linear combination we obtain:

$$u_x(x_i) = \frac{2u(x_{i-2}) - 16u(x_{i-1}) + 16u(x_{i+1}) - 2u(x_{i+2})}{4!\Delta x} + \mathrm{O}(\Delta x^4) \tag{55}$$

This is a 4th order central finite difference differentiation formula, which means it is 4th order accurate (so it calculates without error the 1st derivative of polynomials up to 4th order) and it calculates the derivative using values of $u(x)$ in 2 points downwind and 2 points upwind. This formula can be applied only to internal nodes $i = 3, \ldots, N\text{-}2$, while at the boundary nodes x_1, x_2, x_{N-1} and x_N, different formulas must be applied, in order to avoid the recourse to fictitious points. We demonstrate how to derive the approximation only for $u_x(x_1)$, while for $u_x(x_2)$, $u_x(x_{N-1})$ and $u_x(x_N)$ we only report the final result. We use Taylor expansions for $u_x(x_2)$, $u_x(x_3)$, $u_x(x_4)$ and $u_x(x_5)$:

$$u(x_2) = u(x_1) + u_x(x_1)\Delta x + \frac{u_{xx}(x_1)}{2!}\Delta x^2 + \frac{u_{xxx}(x_1)}{3!}\Delta x^3 + \ldots \tag{56}$$

$$u(x_3) = u(x_1) + u_x(x_1)2\Delta x + \frac{u_{xx}(x_1)}{2!}(2\Delta x)^2 + \frac{u_{xxx}(x_1)}{3!}(2\Delta x)^3 + \ldots \tag{57}$$

$$u(x_4) = u(x_1) + u_x(x_1)3\Delta x + \frac{u_{xx}(x_1)}{2!}(3\Delta x)^2 + \frac{u_{xxx}(x_1)}{3!}(3\Delta x)^3 + \ldots \tag{58}$$

$$u(x_5) = u(x_1) + u_x(x_1)4\Delta x + \frac{u_{xx}(x_1)}{2!}\left(4\Delta x\right)^2 + \frac{u_{xxx}(x_1)}{3!}\left(4\Delta x\right)^3 + \ldots \tag{59}$$

Let's make a linear combination of them and impose again that the parametric coefficient that multiplies $u_x(x_1)$ be 1, to retain the 1st derivative in which we are interested; to delete 2nd, 3rd and 4th order derivatives we impose the conditions that respective derivatives be 0. Solving the linear system in a, b, c and d and highlighting $u_x(x_1)$, we obtain:

$$u_x(x_1) = \frac{-50u(x_1) + 96u(x_2) - 72u(x_3) + 32u(x_4) - 6u(x_5)}{4!\Delta x} + \mathrm{O}(\Delta x^4) \tag{60}$$

For the node x_2 we apply the same procedure to the Taylor expansions of $u_x(x_1)$, $u_x(x_3)$, $u_x(x_4)$ and $u_x(x_5)$, obtaining:

$$u_x(x_2) = \frac{-6u(x_1) - 20u(x_2) + 36u(x_3) - 12u(x_4) + 2u(x_5)}{4!\Delta x} + \mathrm{O}(\Delta x^4) \tag{61}$$

In similar way, we derive the following differentiation formulas for $u_x(x_{N-1})$ and $u_x(x_N)$:

$$u_x(x_{N-1}) = \frac{-2u(x_{N-4}) + 12u(x_{N-3}) + 36u(x_{N-2}) + 20u(x_{N-1}) + 6u(x_N)}{4!\Delta x} + \mathrm{O}(\Delta x^4) \tag{62}$$

$$u_x(x_N) = \frac{6u(x_{N-4}) - 32u(x_{N-3}) + 72u(x_{N-2}) - 96u(x_{N-1}) + 50u(x_N)}{4!\Delta x} + \mathrm{O}(\Delta x^4) \tag{63}$$

The compact form of the previous differentiation formulas is:

$$\overline{u_x}(x_i) = \frac{1}{4!\Delta x}\begin{bmatrix} -50 & 96 & -72 & 32 & -6 \\ -6 & -20 & 36 & -12 & 2 \\ 2 & -16 & 0 & 16 & -2 \\ -2 & 12 & -36 & 20 & 6 \\ 6 & -32 & 72 & -96 & 50 \end{bmatrix}\overline{u} + O(\Delta x^4) \tag{64}$$

Proceeding with the developed method, we can derive higher order differentiation formulas, based on 7 points (6th order differentiation scheme), 9 points (8th order differentiation scheme) and so on. An algorithm to obtain the weights of the various formulas is reported by Fornberg (1988), together with some tables that report these coefficients for various order differentiation schemes.

There are mainly two reasons that discourage to use such higher order formulas:

1. the PDE solution in general does not vary as a polynomial along x, thus the advantages that these higher order formulas offer would not be effective;
2. the higher the order of the approximating polynomial, the higher the number of roots of its 1st derivative and hence the number of maxima and minima. Accordingly, the possibility of unrealistic oscillations of the numerical solution increases. As reported by Schiesser (1991), a good compromise between accuracy and minimization of the oscillation is the 4th order formula.

A possible alternative is to consider different approximation of the PDE spatial derivatives, such as spline approximations. We therefore see that the NUMOL method can be implemented in many ways.

3.2.3 Fourth order differentiation formula for second derivative

PDEs such as for example the diffusion-reaction equation solved in Section 3.1, could contain besides 1st order spatial derivatives also 2nd order derivatives. A 1st approach in the discretization of such derivatives is the one called *stagewise differentiation*, which consists in applying again the 1st derivative formulas to the already calculated 1st derivative terms. Alternatively, we can calculate the 2nd derivative directly from the dependent variable values.

To derive the differentiation formulas for 2nd derivative we proceed in the same way we did before. Let's get the formula for internal nodes $i = 3, \ldots, N\text{-}2$; we consider Taylor expansions for $u(x)$ at x_{i-2}, x_{i-1}, x_{i+1} and x_{i+2}, reported in Eqs. (50), (51), (52) and (53). Let's multiply each of them for an unknown coefficient:

$$a \cdot u(x_{i-2}) = a \cdot u(x_i) - a \cdot u_x(x_i) 2\Delta x + a \cdot \frac{u_{xx}(x_i)}{2!}\left(-2\Delta x\right)^2 - a \cdot \frac{u_{xxx}(x_i)}{3!}\left(2\Delta x\right)^3 + \ldots \tag{65}$$

$$b \cdot u(x_{i-1}) = b \cdot u(x_i) - b \cdot u_x(x_i) \Delta x + b \cdot \frac{u_{xx}(x_i)}{2!}\left(-\Delta x\right)^2 - b \cdot \frac{u_{xxx}(x_i)}{3!}\left(\Delta x\right)^3 + \ldots \tag{66}$$

$$c \cdot u(x_{i+1}) = c \cdot u(x_i) + c \cdot u_x(x_i) \Delta x + c \cdot \frac{u_{xx}(x_i)}{2!}\left(\Delta x\right)^2 + c \cdot \frac{u_{xxx}(x_i)}{3!}\left(\Delta x\right)^3 + \ldots \tag{67}$$

$$d \cdot u(x_{i+2}) = d \cdot u(x_i) + d \cdot u_x(x_i) 2\Delta x + d \cdot \frac{u_{xx}(x_i)}{2!}\left(2\Delta x\right)^2 + d \cdot \frac{u_{xxx}(x_i)}{3!}\left(2\Delta x\right)^3 + \ldots \tag{68}$$

then sum all of them. To keep the 2nd derivative term in which we are interested and cancel the 3rd, 4th, and 5th order ones we impose the following constraints:

$$\begin{aligned} \frac{4a + b + c + 4d}{2!} &= 1 \\ \frac{-8a - b + c + 8d}{3!} &= 0 \\ \frac{16a + b + c + 16d}{4!} &= 0 \\ \frac{-32a - b + c + 32d}{5!} &= 0 \end{aligned} \tag{69}$$

By solving this linear system and substituting the coefficients in Eqs. (65), (66), (67) and (68) we finally obtain:

$$u_{xx}(x_i) = \frac{-2u(x_{i-2}) + 32u(x_{i-1}) - 60u(x_i) + 32u(x_{i+1}) - 2u(x_{i+2})}{4!\Delta x^2} + \mathrm{O}(\Delta x^4) \tag{70}$$

To maintain the discussion brief, we won't derive the approximations for the boundary nodes. The procedure is the same, but with some exceptions necessary to include boundary conditions of the Neumann or Dirichlet type at x_1 and x_N.

3.2.4 Upwind approximations

Let us consider an apparently simple-to-solve PDE, which describes the dynamic convective (inviscid) transport of heat along a tube. This is a 1st order hyperbolic PDE in 1-dimensional domain:

$$\begin{aligned} T_t &= -u \cdot T_x \\ T(x,0) &= 0 \\ T(0,t) &= f(t) \end{aligned} \tag{71}$$

where T (-) is a dimensionless temperature, u (m/s) is the fluid velocity and $f(t)$ is the unit step function, which worth *0* for $t<0$ and *1* for $t>0$. In practice, for $t<0$ temperature everywhere inside the tube is *0*, then abruptly it jumps to *1* at the inlet. The analytical solution to this PDE is

$$T(x,t) = f(t - x/u) \tag{72}$$

which represents the propagation along x at the velocity u of a square wave, the unit step, in practice a discontinuity advancing along x. This is what make hyperbolic PDE difficult to solve. If we try to solve it with a NUMOL code using 2nd order or 4th central finite difference approximation for the 1st derivative, the results we obtain even for a strongly discretized grid are those shown in Fig. 17a and 17b (where the x-domain length is *1*, as well as *u*), where we note an evident numerical oscillation. These central finite difference approximations fail to correctly calculate the derivative T_x since they take information both upwind and downwind respect to the direction of flow, while it seems clear that values of T upwind influence the derivative in x_i much more than those downwind, since the only phenomenon which contributes to the transport of energy is the convective transport in the positive x-direction. Following this reasoning, the simplest approximation for the 1st derivative of T in x_i (assuming flow from left to right) follows from the Taylor expansion of $T(x_{i-1})$ around x_i, truncated at the 1st term:

$$T(x_{i-1}) = T(x_i) - T_x(x_i)\Delta x + O(\Delta x^2) \tag{73}$$

Isolating $T_x(x_i)$, we obtain:

$$T_x(x_i) = \frac{T(x_i) - T(x_{i-1})}{\Delta x} + O(\Delta x) \tag{74}$$

which is the 1st order upwind (backward) approximation of $T_x(x_i)$. If we want to use this approximation, we must pay attention that at the boundary node x_1, we must use a downwind

approximation, in order not to consider a fictitious point before x_1. The formula for the case of negative flow, can be easily derived.

This approximation permits to erase the oscillation of the numerical solution, but it is only 1st order accurate and it introduces a phenomenon called *numerical diffusion*, which leads to a spreading of the profile in the time and space, as it is evident from Fig. 18a and 18b below. To limit this numerical error, we can derive the upwind approximation based on more points, which means increase the accuracy of the numerical formula. The procedure is the same used to derive Eq. (45), and we obtain the 2nd order upwind approximation:

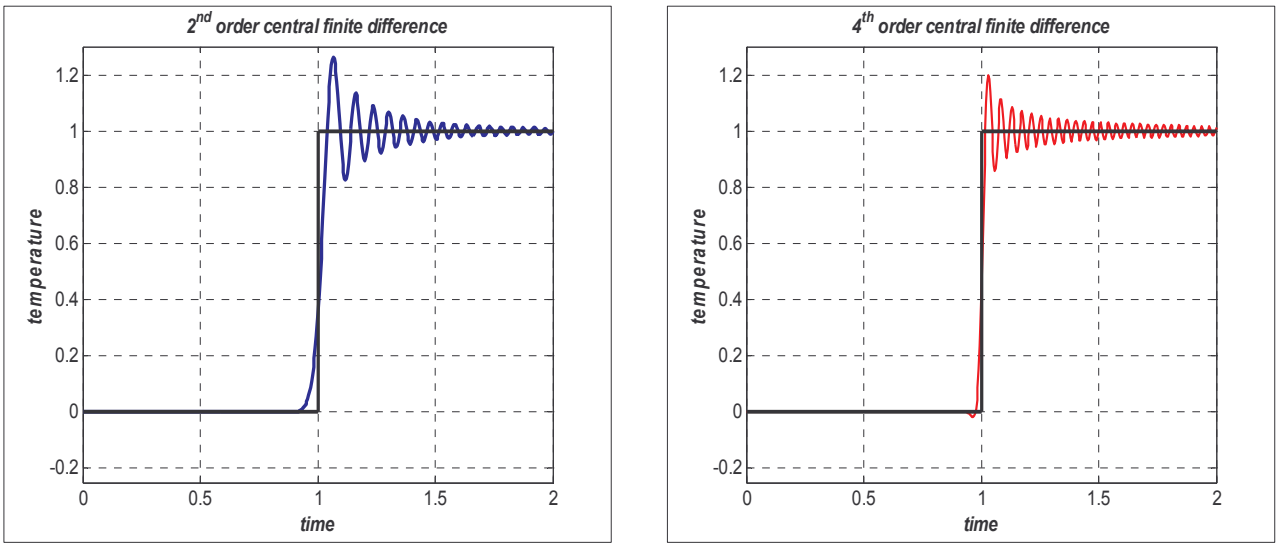

a) b)

Fig. 17. Solution with NUMOL of the transport equation using central finite difference schemes (a) 2nd order central finite difference scheme, b) 4th order central finite difference scheme).

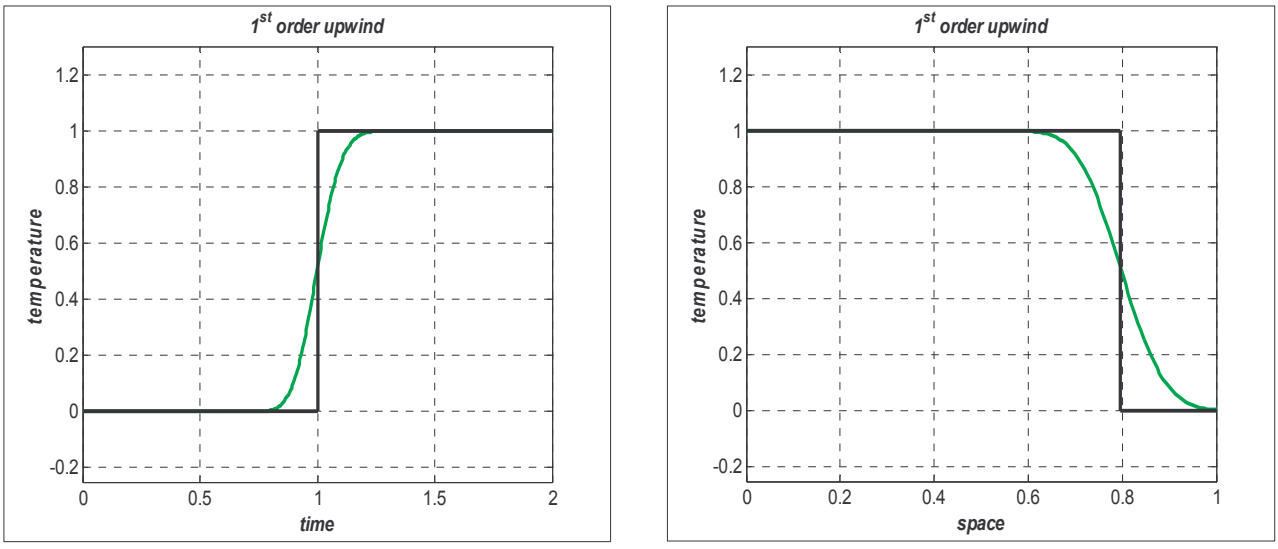

a) b)

Fig. 18. Solution with NUMOL of the transport equation using 1st order upwind scheme (a) time spreading due to numerical diffusion, b) space spreading due to numerical diffusion).

$$T_x(x_i) = \frac{3T(x_i) - 4T(x_{i-1}) + T(x_{i-2})}{2\Delta x} + \mathrm{O}(\Delta x^2) \tag{75}$$

Always in the case of positive flow, the approximation of T_x at nodes x_2 and x_1 could be done respectively through a 2nd order central finite difference based on nodes x_3, x_2 and x_1 and a 2nd order downwind (forward) approximation based on the same nodes. Application of this formula leads to results in Fig. 19a. We can see that numerical diffusion is strongly limited respect to previous case, but some oscillation appear again but before the discontinuity. So it has been proposed by Carver and Hinds (1978) to merge the upwind and central finite difference approximation in a 4th order upwind approximation, which gathers and weights information from 3 points upwind, the point in which we are interested in calculate T_x and 1 point downwind. The differentiation formula for the nodes $i = 4, \ldots, N\text{-}1$ for the case of positive flow is the following:

$$T_x(x_i) = \frac{-2T(x_{i-3}) + 12T(x_{i-2}) - 36T(x_{i-1}) + 20T(x_i) + 6u(x_{i+1})}{4!\Delta x} + \mathrm{O}(\Delta x^4) \tag{76}$$

Appropriate formulas must be derived for the boundary nodes. The performance of this approximation is reported in Fig. 19b below. Numerical diffusion is practically negligible, while some oscillations still appear upwind and downwind respect to the wave front, but their amplitude as well as time duration is lower than in previous cases. Schiesser (1991) suggests to use this approximation for the 1st derivative in hyperbolic PDEs.

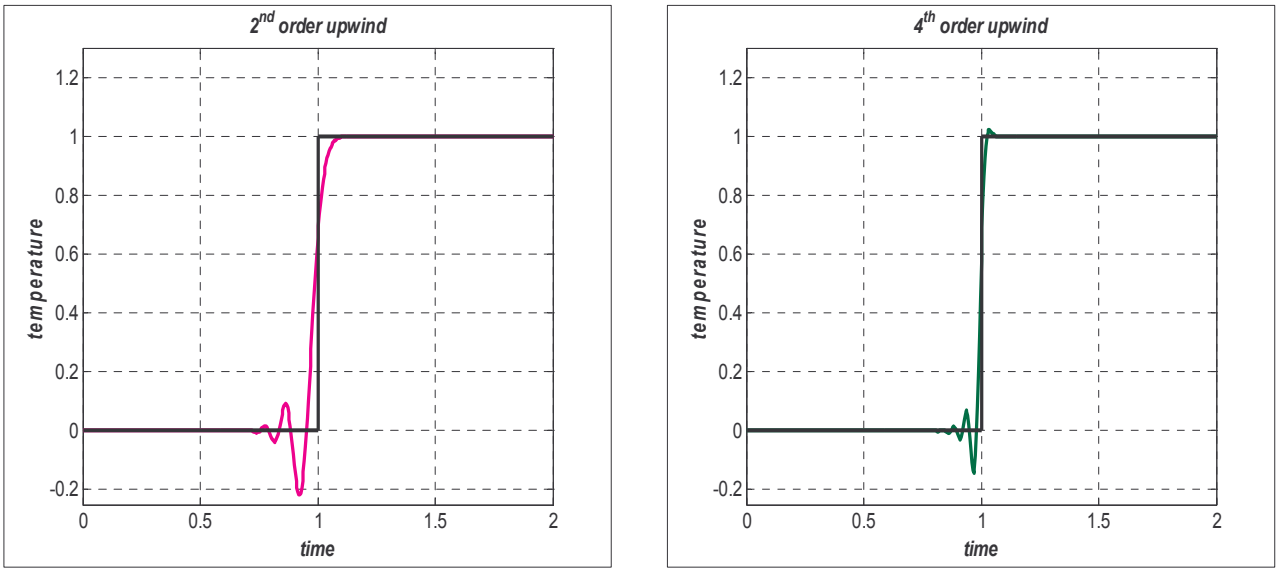

a) b)

Fig. 19. Solution with NUMOL of the transport equation using higher order upwind schemes (a) 2nd order upwind scheme, b) 4th order upwind scheme).

Practically speaking, in the modelling of a chemical reactor, we normally expect that a certain amount of dispersion (backmixing) in the flow of the fluid exists. This impedes the propagation of a discontinuity as it happens with Eq. (71); thus the behaviour of the central finite difference and upwind schemes improves noticeably. Let's add for example a dispersion term to Eq. (71), obtaining the dynamic convection-diffusion equation for energy transport (Eq. (77)), which represent in a more realistic way the heat transport in a vessel:

$$\begin{aligned} T_t &= -uT_x + \alpha T_{xx} \\ T(x,0) &= 0 \\ T(0,t) &= f(t) \\ T_x(L,t) &= 0 \end{aligned} \tag{77}$$

α (m^2/s) is the thermal conductivity and $f(t)$ is the same step function used before. The thermal Pe number ($=(u \cdot L)/\alpha$) defines the relative strength of convection and dispersion term; higher Pe means strong convection, and so possible oscillations for the numerical solution. In Fig. 20 we see a comparison of the performance of three approximation formulas for a simulation in which $L = 1m$, Pe $=200$ (so strong convective component) and just 30 spatial intervals; it's evident how each of the approximations behaves satisfactorily, except for a small amplitude oscillation and a limited amount of numerical diffusion when the 2nd order upwind method is used.

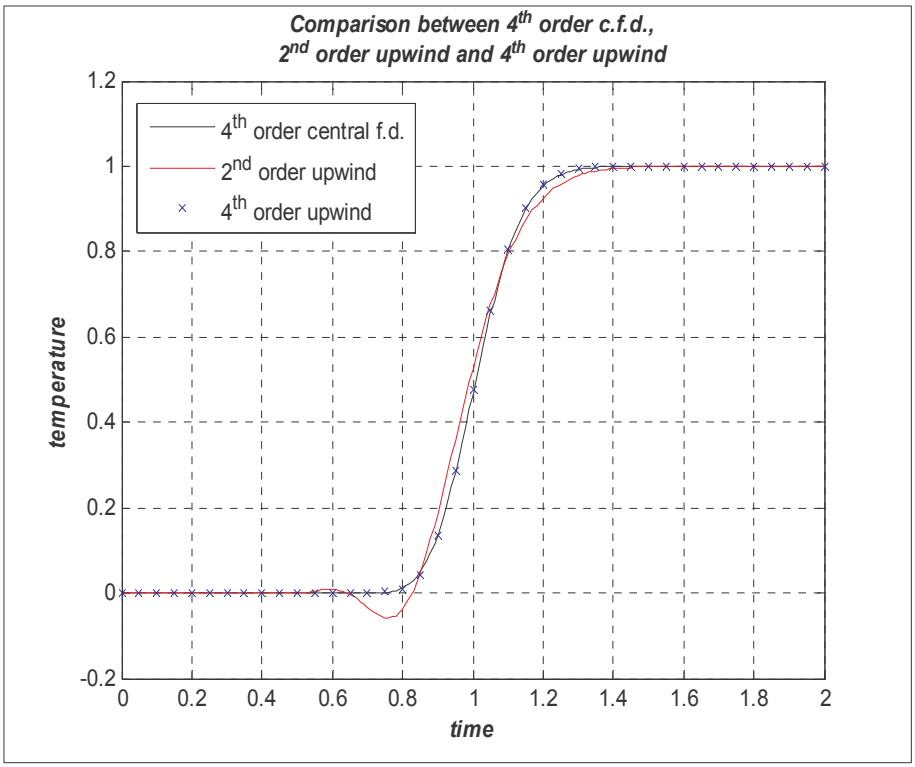

Fig. 20. NUMOL solution of convection-diffusion equation for energy transport using three different discretization schemes.

3.3 Initial-value integration

Two concepts are central to the numerical integration of ODEs, which is the 2nd fundamental step in a NUMOL code: accuracy of the solution and stability of the algorithm. The 1st requirement, accuracy, could be specified by the user through definition of two tolerances, a relative one and an absolute one. As it is reported in Schiesser (1991) as well as in *MatLab 7.1 Help*, at each integration step the error *e* estimated by the solver on the *i*-th component of the solution *y* must be less than or equal to the error defined by the user through a RelTol and an AbsTol by means of Eq. (78) :

$$\left|e(i)\right| \le \max\left(\mathrm{RelTol}\cdot\mathrm{abs}\left(\mathrm{y}\left(\mathrm{i}\right)\right),\mathrm{AbsTol}\right) \tag{78}$$

The RelTol relative error tolerance controls the number of correct digits in the solution components, except for those smaller than AbsTol(i), considered as a threshold. So the definition of the latter is important especially when one of the components of the solution (in case *y* is an array) is small.
Default values of RelTol and AbsTol in *MatLab* ODE suite are 1e-3 and 1e-6. Schiesser (1991) suggests to use a stringent value of RelTol (1e-4 - 1e-6) in order to gain higher accuracy and to avoid an interaction between the errors of the ODE integration and spatial differentiation; in this way the error of the NUMOL solution could be attributed mainly to the spatial differentiation. It is obvious that more stringent integration tolerance leads to greater computational time, so that sometimes a relaxation of this factor is necessary.
In case the estimated error exceeds the user specified tolerance defined above, the solver reduces the time step to increase accuracy and repeat the solution procedure. This continues until the error fulfil the above condition.
Finally, let's come to the stability requirement of a ODE solver, which is the factor that must guide our choice of the solver. We report briefly the treatment reported in Schiesser (1991), considering 1st of all the stability properties of a system of linear, constant-coefficient ODEs, then of a non-linear system and finally the stability properties of some integration algorithms.

3.3.1 Stability of a linear, constant-coefficient ODE system

Let's consider a system of linear, constant-coefficient ODEs, which in matrix form appears as:

$$\begin{aligned} \frac{d\bar{y}}{dt} &= A\bar{y} \\ \bar{y}(0) &= \bar{y}_0 \end{aligned} \tag{79}$$

where A is the coefficient matrix, a n x n matrix in the most general case; we directly develop our reasoning for a n x n system. Solutions of such a system are in the exponential form:

$$\bar{y} = \bar{C}e^{\lambda t} \tag{80}$$

where λ is a generic eigenvalue of the system. Substituting these assumed solutions in the system (79) and simplifying the common term $e^{\lambda t}$, we obtain:

$$(A-\lambda I)\overline{C}=0 \tag{81}$$

where I is the identity matrix, which is the general form of the linear algebraic eigenvalue problem. In order for this homogeneous system not to have a trivial solution ($\vec{C}=0$), the matrix A-λI must have zero determinant. This condition leads to the characteristic equation of system (79), Eq. (82) below, a n^{th} order polynomial in λ from which we can extract the n eigenvalues.

$$\det(A-\lambda I)=0 \tag{82}$$

Given the form of the solution of system (79), we can derive the following criterion for the stability of a general linear, constant-coefficient, 1st order ODEs system: all n eigenvalues given from Eq. (82) must have negative real parts. This is in order not to have exponential terms that explodes in the solution.

The main property of the system (79) that is of interest for the selection of an ODE integrator is the *sparsity* of the eigenvalues of A, which defines the *stiffness* of the ODE problem; if eigenvalues vary for orders of magnitude, a stiff ODE integrator is necessary in the NUMOL code.

The problem is that normally ODEs systems are nonlinear. Let's see how it is possible to extend these conclusions to this case.

3.3.2 Stability of a non-linear ODE system

A rigorous stability analysis for non-linear ODEs doesn't exist (Schiesser, 1991), but some of the ideas developed for the linear case are applied as well.

A non-linear ODE system could be written in matrix form as

$$\begin{aligned}&\frac{d\overline{y}}{dt}=\overline{f}(\overline{y},t)\\&\overline{y}(0)=\overline{y_0}\end{aligned} \tag{83}$$

where $\overline{f}(\overline{y}, t)$ is an array of non-linear functions of the variables $\overline{y}$. To linearize them, let's take Taylor expansion around ($\overline{y}_s$, t_s) truncated to the 1st term:

$$\overline{f}\left(\overline{y},t\right)=\overline{f}\left(\overline{y}_s,t_s\right)+J\left(\overline{y}_s,t_s\right)\left(\overline{y}-\overline{y}_s\right) \tag{84}$$

where J is the *Jacobian matrix*, i.e. the n x n matrix of the partial derivatives of each f respect to each dependent variable y. Its important properties are:

1. it is a matrix of constants for a linear ODE system, in which case it coincides with the coefficient matrix A;
2. its elements are functions of $\overline{y}$ for a non-linear ODE system.

If we rewrite Eq. (83) with Eq. (84), the non-linear system becomes identical to the linear one, with J having the same role of A. So the previous conclusions about the eigenvalues properties still apply to the linearized form of (83), but in this case their numerical value depend on ($\bar{y}_s$, t_s), they're not constant during the time evolution of the solution. The stiffness of the ODE system will be related to the separation of the eigenvalues of the Jacobian matrix.

3.3.3 Stability of explicit methods

Let's consider the most simple explicit method, the Euler method or 1st order Runge-Kutta method; it is derived from a Taylor expansion of $\bar{y}$ truncated at the 1st term:

$$\bar{y}(t_{n+1}) = \bar{y}_{n+1} = \bar{y}_n + \frac{d\bar{y}_n}{dt}(t_{n+1} - t_n) = \bar{y}_n + \frac{d\bar{y}_n}{dt}\Delta t \tag{85}$$

which means that to calculate $\bar{y}$ at new time instant t_{n+1} we only need to know its value and its time derivative at the previous instant t_n. In the particular case of a scalar y, it calculates the solution at t_{n+1} moving along the tangent to the solution at t_n; the solution has accuracy $O(\Delta t)$.

To study the stability of this method, let's proceed in a similar way as we did in Section 3.3.1; let's consider for simplicity a linear, constant coefficient system of 2 ODEs (which could also be 2 non-linear ODEs linearized) and apply Eq. (85); we obtain:

$$\begin{aligned} y_{1,n+1} &= y_{1,n} + (a_{11}y_{1,n} + a_{12}y_{2,n})\Delta t \\ y_{2,n+1} &= y_{2,n} + (a_{21}y_{1,n} + a_{22}y_{2,n})\Delta t \end{aligned} \tag{86}$$

These are called *difference equations*. It is assumed that they have solutions in the form:

$$\begin{aligned} y_{1,n} &= C_1\beta^n \\ y_{2,n} &= C_2\beta^n \end{aligned} \tag{87}$$

in analogy to Eq. (80) for the ODEs. Substituting (87) in (86), simplifying β^n and rearranging, we obtain:

$$\begin{aligned} \big((\beta - 1) - a_{11}\Delta t\big)C_1 - a_{12}\Delta t C_2 &= 0 \\ -a_{21}\Delta t C_1 + \big((\beta - 1) - a_{22}\Delta t\big)C_2 &= 0 \end{aligned} \tag{88}$$

which is a linear, homogenous system in C_1 and C_2; in order for it not to have trivial solution, the determinant of the coefficient matrix must be 0. Again, as in Section 3.3.1, this condition gives the characteristic equation of the system (86), which is a 2nd order polynomial in β:

$$\big((\beta - 1) - a_{11}\Delta t\big)\cdot\big((\beta - 1) - a_{22}\Delta t\big) - a_{21}a_{12}\Delta t^2 = 0 \tag{89}$$

The roots β_1 and β_2 are the eigenvalues of the system (86). From the form of the solutions (87), we can finally derive a criterion for the *stability* of the explicit Euler method; in order for the numerical solution not to become unbounded with increasing n (so as we step in the time), it must be that

$$|\beta| < 1 \tag{90}$$

for all the eigenvalues.

To derive a practical consequence of this criterion, we shall relate the eigenvalues β of the difference equations, on which depend the stability of the numerical solution, with those of the original ODEs system, λ, which define its stiffness, since in both of the characteristic equations, the coefficients a_{ij} of the original ODEs appear. By the way, to derive this relation we refer to a simplest case, in which $a_{11}=a_{22}=-a$ and $a_{12}=a_{21}=b$, in order to have real λ. One can easily demonstrate that:

$$\begin{aligned} \lambda_1 &= -(a-b) \\ \lambda_2 &= -(a+b) \end{aligned} \tag{91}$$

In a similar way we obtain that:

$$\begin{aligned} \beta_1 &= 1-(a-b)\Delta t \\ \beta_2 &= 1-(a+b)\Delta t \end{aligned} \tag{92}$$

From the stability criterion (90), in order for the numerical solution to be stable, it is necessary that:

$$\begin{cases} |1+\lambda_1 \Delta t| \le 1 \\ |1+\lambda_2 \Delta t| \le 1 \end{cases} \Leftrightarrow \begin{cases} |\lambda_1 \Delta t| \le 2 \\ |\lambda_2 \Delta t| \le 2 \end{cases} \tag{93}$$

This is a general result for the Euler explicit method, even when it is applied to a system of N linear, constant coefficient ODEs, in which case conditions (93) must extend to all N eigenvalues of the system.

The practical implication of this result is immediate. If we have for example λ_1=-1 and λ_2=-1e6, they are both real and negative so the ODEs system is stable, but they are strongly separated, that means that the system is stiff. Another important feature of the ODEs system that we can get from the general form of their solutions, Eq. (80), is that the smallest eigenvalue defines the ODE time scale (i.e., the time span of integration), while the largest eigenvalue defines the maximum integration step Δt that ensures stability of the explicit Euler method, according to Eq. (93). Accordingly, this integration step is no more varied only to meet the user specified error, but also to ensure the stability of the explicit method.

If the separation of the eigenvalues, and in particular of the smallest and largest, is huge, the number of the integration steps by the explicit Euler method to give a stable solution becomes unreasonable. This is a stability not an accuracy problem of the method. So using explicit RK methods of higher order (as the 4th and 5th order method in the *MatLab* solver *ode45*), the stability interval enlarges in a negligible way (Schiesser, (1991)). So all the explicit numerical integration methods have limited stability intervals and therefore are not effective to solve stiff ODE problems, while for non-stiff

problems (whose extreme eigenvalues are separated by no more than a factor 1e3), these algorithms work very well, and as pointed out in the *MatLab* Help, the *ode45* should be the 1st function to use for most problems.

3.3.4 Stability of implicit methods

The implicit Euler method is

$$\bar{y}_{n+1} = \bar{y}_n + \frac{d\bar{y}_{n+1}}{dt}\Delta t = \bar{y}_n + \bar{f}\left(\bar{y}_{n+1}, t_{n+1}\right)\Delta t \tag{94}$$

where the derivative is no more evaluated at t_n, but at t_{n+1}. Let's apply Eq. (94) to a linear, constant coefficient system of 2 ODEs as we did in Section 3.3.3 to get the difference equations, then repeat the same steps did before until we obtain the characteristic equation of the difference equations:

$$\left[1+\left(a_{11}\Delta t-1\right)\beta\right]\cdot\left[1+\left(a_{22}\Delta t-1\right)\beta\right]-a_{12}a_{21}\Delta t^2\beta^2=0 \tag{95}$$

Again we could derive from here the eigenvalues expressions and relate them to the eigenvalues of the ODEs system, but let's do it for the simple case used before. The relation between the eigenvalues β and λ in this case is:

$$\begin{aligned}\beta_1 &= \frac{1}{1-\lambda_1\Delta t}\\ \beta_2 &= \frac{1}{1-\lambda_2\Delta t}\end{aligned} \tag{96}$$

Since the general form of the solutions to the difference equations is the same as before, in order for the solution to remain stable the criterion (90) must again apply to all eigenvalues. If we look at Eq. (96) and consider to have a stable ODEs system (Re$(\lambda)<0$), denominator is always greater than 1, thus the stability criterion is always satisfied for any values of Δt. The same conclusion can be extended to a linear system of N ODEs, with all eigenvalues having negative real parts, that means that the eventual stiffness of the problem is not a problem when we are using an implicit Euler method.

The integration step Δt is thus not limited by stability, but only by accuracy. These conclusions are strictly valid for linear, constant coefficient ODEs, however the implicit Euler method has demonstrated to be effective also for the solution of stiff non-linear ODEs. In the non-linear case, a root-finding method must be applied to Eq. (97), difference equations for the implicit Euler method, to obtain $\bar{y}_{n+1}$, as for example Newton's method.

$$\bar{y}_{n+1} = \bar{y}_n + \bar{f}\left(\bar{y}_{n+1}, t_{n+1}\right)\Delta t \tag{97}$$

Finally, even if the implicit Euler is unconditionally stable, it is little accurate (1st order correct), so a more accurate implicit method is normally used in the integration of stiff ODEs system.

If we consider the MatLab ODE solver *ode15s*, this is a variable order, multistep solver that implements an algorithm based on the numerical differentiation formulas (NDFs) and optionally the usually less efficient backward differentiation formulas (BDFs or Gear's method): both of them are implicit algorithms of higher accuracy than the implicit Euler method. Let's examine briefly the main characteristics of this solver.

The general stepping formula for the BDF method is (Schiesser, 1991):

$$y_{n+1} = \sum_{l=0}^{q-1} \alpha_l y_{n-l} + \Delta t \beta_0 \frac{dy_{n+1}}{dt} \tag{98}$$

where q is the order of the method, while α_l and β_0 are constants that vary with the order. For the implicit Euler method, q=1 as well as α_l and β_0. The term *multistep* method arises from the fact that, in case q>1 to estimate y_{n+1} it uses more than one past value of the numerical solution. Gear (1971) has derived the values of coefficients α_l and β_0 that give a trade-off between good accuracy and stability for $1 \leq q \leq 6$; when q=6, the time behaviour of the solution is approximated by a 6th order polynomial, but for this to be possible we need to know the values of the solution at 6 past instants. These are not available at the initial step, so the calculation must start with the implicit Euler method, then point after point, higher order BDF method can be used. Computer implementation of BDF methods so normally has to change the integration step Δt to meet the user requirement about accuracy and also the order of the algorithm, leading to a variable step, variable order, multistep implicit method.

As said before, the coefficients α_l and β_0 have been estimated to achieve a compromise between accuracy and stability; this sounds strange since from what we showed before, the implicit Euler method is unconditionally stable. Actually, implicit methods of order higher than 2nd are not unconditionally stable, i.e. a part of the left half of the complex plane Im($\lambda \Delta t$) vs Re($\lambda \Delta t$) is not stable for them. The coefficients derived by Gear assure that the negative real axis remains in the stable region, for implicit methods of every order from 1 to 6; for many physical problems, the ODEs eigenvalues are real and negative, so no matter how dispersed they are, BDF methods are stable.

3.4 Adaptive grid

In general could be advantageous to adapt the grid during the solution procedure in order to concentrate nodes where the solution shows a steep trend (large gradients). This could be done with a static grid refinement, which consists in 4 steps outlined by Vande Wouwer et al. (2004-2005):

- approximation of the spatial derivatives on a fixed non-uniform initial grid;
- periodically stopped time integration of the ODEs;

- adaptation/refinement of the spatial grid during integration stops;
- interpolation of the solution on the new grid and restart of the integration.

The other possibility is a continuous adaptation of the grid in the time, which ensures optimal location of the grid points, since instant per instant the internal node positions are updated following the trend of the solution in the time. We don't report the complex mathematical derivation of the algorithm proposed by Vande Wouwer et al. (2004-2005), but just the main ideas of the algorithm. It is based on a Lagrangian formulation of the PDE problem, so that the total time derivative of function *u(t,x)* is

$$\frac{Du}{Dt} = \frac{\partial u}{\partial t} + \frac{dx}{dt}\frac{\partial u}{\partial x} \tag{99}$$

dx/dt is the ODE that defines the movement of the node in the time and is derived in order to equidistribute a monitor function *m(x)* which is related to the 1st or 2nd derivative of the solutions and evaluated in discrete form in each spatial interval $[x_i,x_{i+1}]$ (Vande Wouwer et al. (2004-2005)). An example could be:

$$m(i) = \sqrt{\alpha + \frac{1}{n_{eq}}\sum_{j=1}^{n_{eq}}\left[\frac{u(x_{i+1},j) - u(x_i,j)}{z_{i+1} - z_i}\right]^2} \tag{100}$$

where *m(i)* is the monitor function in the interval $[x_i,x_{i+1}]$, n_{eq} the number of PDEs (or dependent variables) and the index j=1: n_{eq} defines the particular dependent variable. Defined *dx/dt*, we can treat the coordinates of the internal nodes as if they were further N-2 unknowns besides the "actual" n_{eq}· (N-1) dependent variables, with N as the total number of nodes; the final ODE system will therefore have (n_{eq}+1)·(N-1) ODEs. Therefore this approach to grid adaptation is more difficult to implement, requires a modification of the original NUMOL algorithm to include the above steps and is more demanding since we must solve N-2 ODEs. On the other side, it optimally locates the grid points following the time evolution of the solutions, does not require periodical interruption of the time integration and interpolation to spawn new initial conditions on the new grid.

Built-in routines implementing dynamic grid adaptation were supplied by Vande Wouver and Schiesser and adapted to our system.

Capitolo 4

Modellazione e simulazione di un reattore trickle-bed di piccola taglia

In questo capitolo si procede dapprima alla caratterizzazione della reazione modello considerata, l'idrogenazione catalitica del monosaccaride L-arabinosio in soluzione acquosa, del meccanismo e del modello cinetico utilizzato. Quindi si riportano le correlazioni utilizzate per il calcolo delle proprietà fisiche della fase liquida.

Si definisce il sistema di reazione studiato, un piccolo reattore trickle-bed di laboratorio con letto catalitico diluito con particelle inerti fini, a cui si alimentano in equicorrente H_2 puro gassoso in pressione (30/60 bar) e una soluzione acquosa diluita di L-arabinosio al 10%m/m. Sono in seguito riportati alcuni modelli matematici di complessità variabile per la simulazione di tale reattore.

Si illustrano i risultati di alcune simulazioni condotte manipolando variabili operative quali la temperatura, le velocità del gas e del liquido, le dimensioni del catalizzatore.

Tali simulazioni rivelano una significativa limitazione della prestazione del reattore dovuta al mass transfer gas-liquido, responsabile della fornitura di H_2 alla fase liquida; questo trasporto può essere migliorato aumentando le velocità delle due fasi, meglio se quella della fase gas che non comporta riduzione del tempo di permanenza nel reattore della fase liquida. Inoltre utilizzando catalizzatore di dimensione caratteristica prossima o superiore a 1 mm, si ha un'ulteriore riduzione della velocità di reazione globale a causa della resistenza al trasporto di specie intraparticellare, con fattori di sfruttamento del catalizzatore fino al 20%.

Esperimenti condotti su un TBR di laboratorio hanno rivelato una forte disattivazione del catalizzatore; è stato effettuato un tentativo di riprodurre i trend sperimentali con uno dei modelli di reattore proposti, incluso un semplice modello di disattivazione del catalizzatore.

Chapter 4

Modeling and simulation of a small-scale trickle bed reactor

Modeling of trickle-bed reactors has been reported in classical texts on three-phase reactors by various authors (Shah, 1979; Ramachandran and Chaudhari, 1983; Gianetto and Silveston, 1986) as well as in the open literature (Rajasekharan et al., 1998; Lange et al., 2004) and more recent texts (Salmi et al., 2010). In this chapter, different models for TBRs are presented and the results of the simulations are reported. Each of these models takes into account different characteristics of this type of reactor, such as interfacial mass-transfer at the gas-liquid interface, at the liquid-solid interface, intraparticle mass transfer, heat transfer in the case of exothermic and endothermic reactions as well as catalyst deactivation in the time. The model reaction considered is the hydrogenation of sugar L-arabinose to the corresponding sugar alcohol in aqueous solution on a Ru/C catalyst. The numerical solution of these models was performed by means of the method of lines, described in the previous Chapter 3, and the codes were written in *MatLab* 7.1 environment.

4.1 Reaction model and regression of kinetic parameters

The catalytic hydrogenation of sugars to their corresponding sugar alcohols is an environmentally friendly route to produce alternative natural sweeteners (Sifontes et al., 2010), since it avoids the use of stoichiometric reducing agents (homogeneus catalyst) that leads to waste inorganic salts, using instead solid metal-based catalysts. Data on hydrogenation experiments of some mono- and disaccharides of industrial interest (L-arabinose, D-galactose, D-maltose, L-rhamnose) were available, conducted at the Laboratory of Industrial Chemistry and Reaction Engineering of Åbo Akademi by Sifontes et al. (2010-2011) in a three-phase slurry reactor at temperature ranging from 90 to 130°C and pressures of H_2 ranging from 40 to 60 bar, using catalyst particles of ruthenium dispersed on active carbon of flake shape, Ru content 2.5%wt surface area about 700m^2/g and average size 10x10μm and thickness 1-2μm (Sifontes et

al., 2010). High stirring rates (1800rpm) were used to operate in the kinetic regime; by-product formation in the hydrogenation of L-arabinose was negligible (Sifontes et al., 2010).

The best fit to experimental kinetics data was obtained with a model based on Langmuir-Hinshelwood assumptions which considered competitive adsorption of H_2 and organic components, adsorption and desorption steps as quasi-equilibrium steps and reaction between hydrogen and sugar as rate limiting step. This is a typical surface reaction which involves a reactant A (sugar) available in the liquid phase, a reactant H_2 supplied by the gas phase and which has to solubilize in the liquid, and a product B (sugar alcohol) which forms and stays in the liquid phase. The mechanism of reaction is shown below:

$$\begin{aligned} H_2 + \sigma &\overset{K_{H_2}}{\rightleftarrows} H_2^* \\ A + \sigma &\overset{K_A}{\rightleftarrows} A^* \\ A^* + H_2^* &\xrightarrow{k} B^* + \sigma \\ B^* &\overset{K_B}{\rightleftarrows} B + \sigma \end{aligned} \tag{101}$$

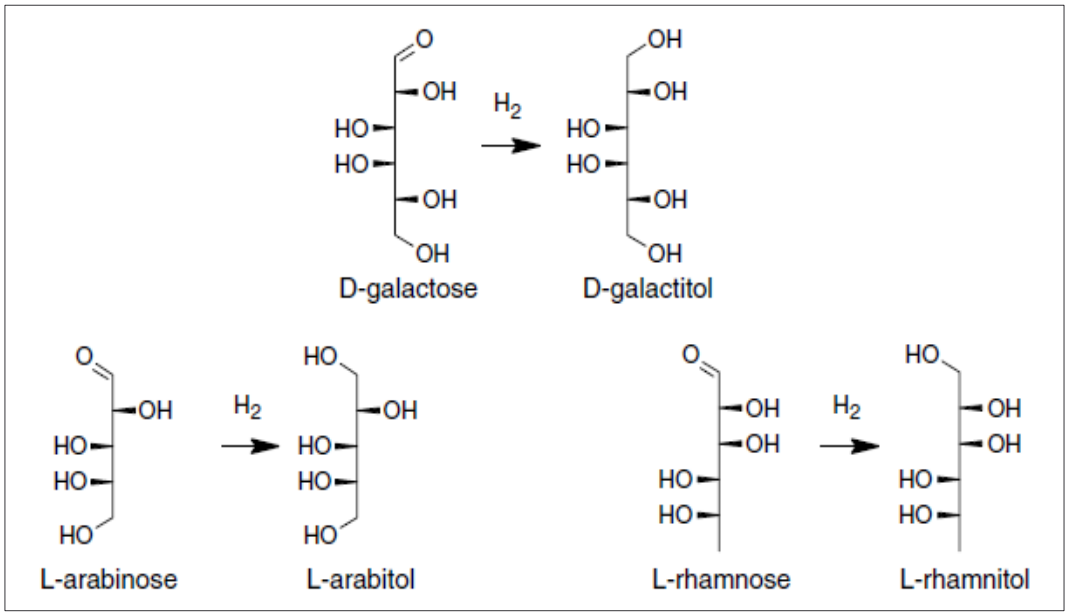

Fig. 21. Stoichiometry of hydrogenation of some monosaccharides: D-galactose, L-arabinose and L-rhamnose (adapted from Sifontes et al., 2011).

The original reaction rate expression proposed by Sifontes et al. (2010) expresses the concentrations of the sugar and the sugar alcohol in %wt, while for H_2 the pressure instead of the concentration was used. It was the latter characteristics that induced us to modify the kinetic expression using molar concentrations of all components, including H_2; in fact, it is commonly accepted and reported in the literature (Ramachandran and Chaudhari, 1983; Gianetto and Silveston, 1986; Al Dahhan and Dudukovic, 1995) that in three-phase reactors and TBR in particular, the catalyst particles are

completely wetted internally, due to capillary effects; accordingly, when we solve the mass balances inside the catalyst particle, often necessary in the case of a TBR, in which the catalytic particles can have size of few mm which can give rise to significant internal mass transfer resistance, it is of poor significance to use a kinetic expression in which appears the pressure of gaseous component, while it is more straightforward to consider its concentration. Moreover, if strong G/L mass transfer limitations prevail in the reactor, the concentration of the dissolved gaseous component and its partial pressure cannot be linked through an equilibrium law such as Henry's law, thus the use of the pressure in the kinetic expression is not correct.

The original data of Sifontes et al. (2010) for the L-arabinose hydrogenation were modified to convert mass fraction of organic compounds to molar concentrations and H_2 pressure in its concentration in the liquid phase, by means of Henry's law, since the hydrogen solubility in water is low. This was possible since no mass transfer limitations existed particularly in the liquid phase thanks to a vigorous stirring, as reported above, thus gas and liquid phase were in equilibrium. To determine the liquid density, necessary to the conversion of mass fractions into molar concentrations, and to calculate the hydrogen concentration at equilibrium, the correlations of Rivero were used (see following Section 4.2).

The reaction rate expression and the reactor model used in the fitting of new kinetic parameters are shown below:

$$k = A\exp\left(-\frac{E_a}{R_G T}\right)$$

$$R = \frac{kK_A K_{H_2} c_A c_{H_2}}{\left(1 + K_A c_A + K_B c_B + K_{H_2} c_{H_2}\right)^2} \qquad (102)$$

$$\frac{d\bar{c}}{dt} = \rho_{cat}\bar{r}$$

where k (mol/g_{Ru}s) is the kinetic constant expressed by means of the Arrhenius law, E_a (J/mol) is the activation energy, R_G (J/mol·K) is the universal gas constant, R (mol/g_{Ru}s) is the reaction rate, K_i (m^3/mol) is the adsorption constant of the generic compound i, c_i (mol/m^3) is the molar concentration of the generic species i, ρ_{cat} (g_{Ru}/m^3) is the active catalyst concentration, calculated as the product of the content of active catalyst (2.5%wt Ru on C) and the catalyst density in the liquid solution (around 0.9 $g_{particle}$/L), and r_i (mol/g_{Ru}s) is the rate of consumption/production of the generic species i per unit mass of active catalyst. The subscript A refers to the reactant L-arabinose and B to the product L-arabitol.

The regression of kinetic parameters A, E_a, K_A, K_B and K_{H2} was conducted in *ModEst* 6.0 environment, using a *Simplex* algorithm and an objective function defined as the sum of square residuals between calculated and experimental concentrations of A and B of all experimental sets:

$$Q(\theta) = \sum_{k=1}^{nsets} \sum_{j=1}^{nobs(k)} \sum_{i=1}^{nydata(j,k)} w_{i,j,k} \left[y_{i,j,k} - y_{p_{i,j,k}}(\theta) \right]^2 \tag{103}$$

where Q is the objective function, θ is the set of parameters to be determined, *nsets* indicates the number of experimental sets, *nobs* the number of observations for each set, *nydata* the number of response variables y on which we want to make the minimization (subscript p denotes predicted values of the response variables).

The estimated values of parameters, the estimated relative standard errors and the coefficient of determination R^2 as given by *ModEst*, are reported in Tab. 13, while some graphical results from the fitting are reported in Fig. 22. The R^2 value obtained is considerably high; the experimental data sets used for the fitting are reported in Appendix A.

Tab. 13. Results of kinetic parameters estimation.

R^2 = 99.26		
Parameter	**Estimated values**	**Estimated Relative Std. Error (%)**
A (mol/g_{cat}s)	5.95e5	50.3
E_a (kJ/mol)	48.8	3.8
K_A (m^3/mol)	2.76e-3	17.9
K_B (m^3/mol)	0.88e-3	50.7
K_{H2} (m^3/mol)	15.2e-3	21.7

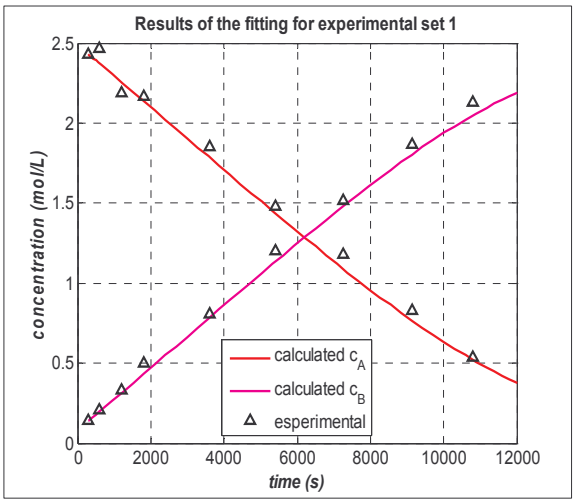

a)

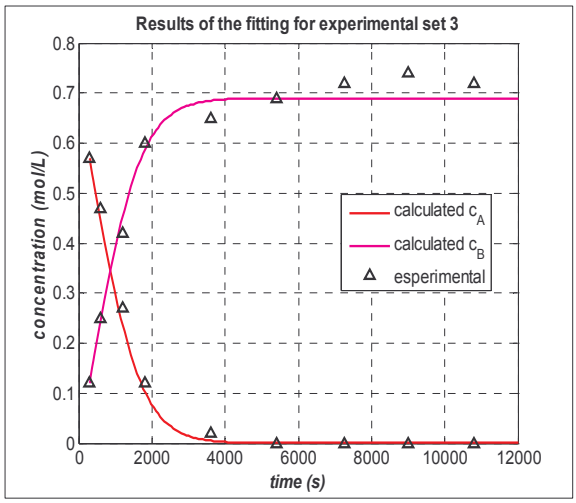

b)

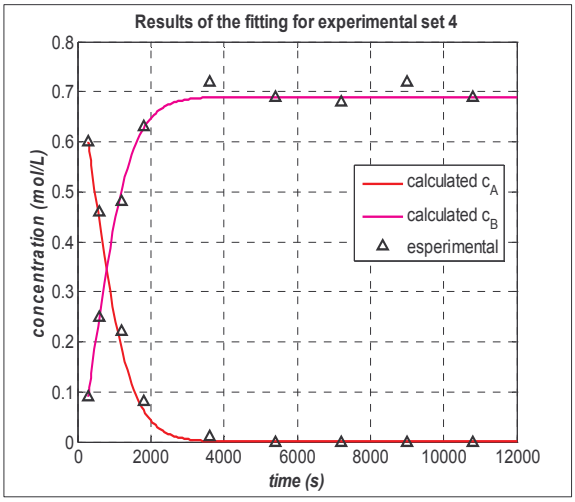

c)

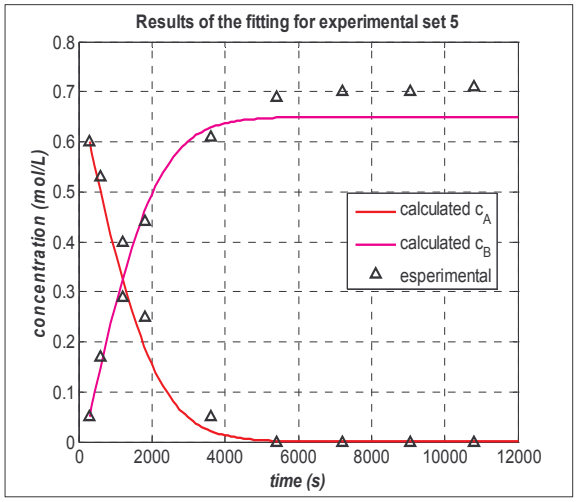

d)

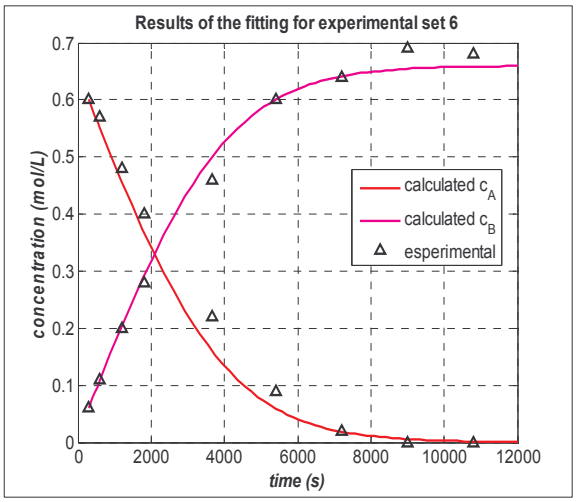

e)

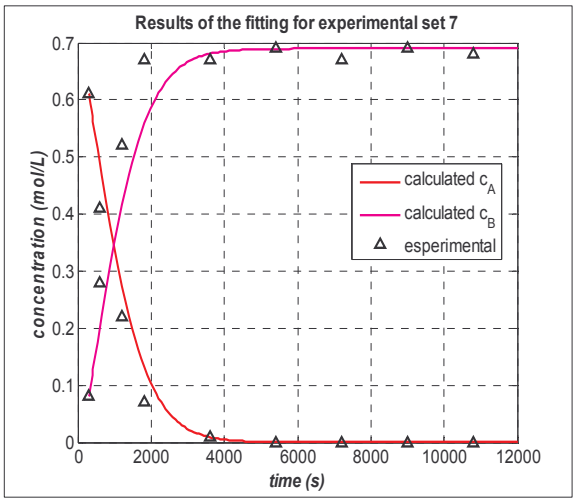

f)

Fig. 22. Experimental and calculated evolution of A and B species in the liquid phase for some data set, with optimal parameters after reworking the regression.

The trends of the reaction rate R as a function of the concentration of A and H_2 for a temperature of 100°C are reported in Fig. 23.

As we see from Fig. 23a, reaction rate dependence on c_A is non-linear and reaction rate sensibility to L-arabinose concentration becomes stronger at high concentration of H_2. The dependence on hydrogen concentration is instead more linear, but again for higher c_A values, reaction rate variation per unit c_{H2} variation is larger.

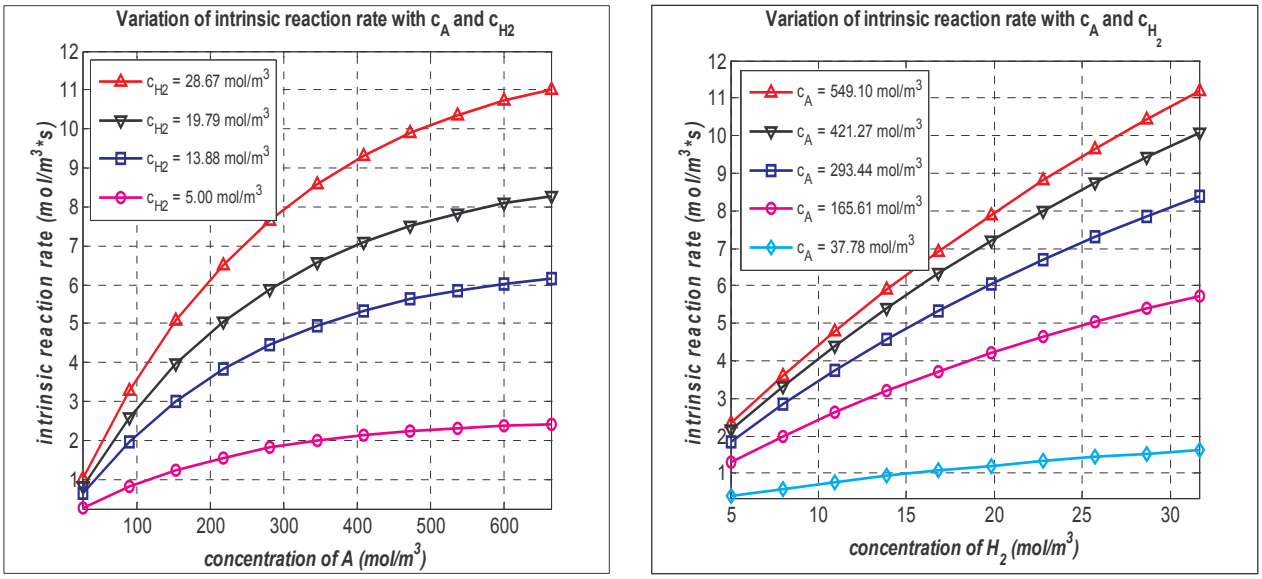

Fig. 23. Trends of the reaction rate as a function of the concentrations of H_2 and L-arabinose (A).

4.2 Physical properties and reactor characteristics

The physical properties of the liquid solution were determined by means of the empirical correlations proposed by Rivero (2009) for the calculation of the density, viscosity and solubility of H_2 in aqueous solutions of sugars, in particular L-arabinose. The density is correlated to temperature (°C) and mass fraction (%wt) of the sugar in solution; the ranges of applicability of the correlation are 60°C $< T <$ 130°C and 0% $< w_A <$ 50%. The correlation together with the dimensional parameters regressed for L-arabinose, whose units of measure can be readily determined from a dimensional analysis on each term, are reported in Eq. (104); Rivero determined a mean percent relative deviation between experimental and generated values of 0.25%.

$$\rho\left(\frac{kg}{m^3}\right) = A\cdot T\cdot w_A + B\cdot w_A^{\,2} + C\cdot w_A + D + E\cdot T + F\cdot T^2$$

$$\begin{cases} A = -8.154\cdot 10^{-4} \\ B = 8.424\cdot 10^{-3} \\ C = 4.797 \\ D = 1.065\cdot 10^{3} \\ E = -1.627 \\ F = 5.412\cdot 10^{-3} \end{cases} \qquad (104)$$

In an analogous way, the viscosity was correlated to the temperature (°C) and mass fraction (%wt) of the sugar in solution, the ranges of applicability of this empirical correlation are 60°C < T < 90°C and 0% < w_A < 50%. The correlation and the dimensional parameters for L-arabinose are reported in Eq. (105); the author determined a mean percent relative deviation between experimental and generated values of less than 2.2%.

$$\ln \mu(cP) = A \cdot \frac{w_A}{T} + B \cdot {w_A}^2 + C \cdot w_A + D + \frac{E}{T} + \frac{F}{T^2}$$

$$\begin{cases} A = 1.544 \\ B = 3.808 \cdot 10^{-4} \\ C = -0.011 \\ D = -2.845 \\ E = 193.763 \\ F = -3892 \end{cases} \tag{105}$$

The correlation for the hydrogen solubility reported in Eq. (106) is valid for 363.15 K < T < 403.15 K, 30 bar < P < 60 bar and only for a 10%wt solution of L-arabinose; Rivero determined a mean percent relative deviation between experimental and generated values of less than 1.8%. However, after having verified that the trend of c_{H2} is linear with pressure at a certain T, he also proposed values of Henry's constants H_{H2} for certain values of T that permit to calculate the hydrogen concentration also outside the above range of pressure.

$$c_{H_2,L} * \left(\frac{mol}{L} \right) = A \cdot P \cdot T + B \cdot T^2 + C \cdot T + D + E \cdot p + F \cdot p^2$$

$$\begin{cases} A = 9.35 \cdot 10^{-6} \\ B = 0.01447 \cdot 10^{-4} \\ C = -1.138 \cdot 10^{-3} \\ D = 0.222 \\ E = -2.833 \cdot 10^{-3} \\ F = -0.1481 \cdot 10^{-8} \end{cases} \tag{106}$$

It is noteworthy that the correlations of Rivero have different ranges of applicability; in particular the correlation for the hydrogen solubility has been derived for one sugar concentration only, thus all simulations have been conducted using a 10%wt L-arabinose solution entering the reactor. Moreover, the temperature ranges for correlations for the viscosity and hydrogen solubility do not overlap; the temperature range we decided to investigate in the simulations has been set in such a way that extrapolations from the temperature intervals of the correlations were limited to at most 10°C.

Other properties related to the liquid phase necessary to use the correlations for the estimation of mass transfer and hydrodynamic parameters are the surface tension of the sugar solution, the density and viscosity of the solvent (water), diffusion coefficients of the solute (H_2) and sugars in the aqueous solution. The first has been approximated to that of pure water and determined from the

correlation of Sastri and Rao (1995) proposed in Poling, Prausnitz, O'Connell (2004) for the calculation of surface tension of polar liquids:

$$\sigma\left(\frac{mN}{m}\right) = K p_c{}^x T_b{}^y T_c{}^z \left(\frac{1-T_r}{1-T_{br}}\right)^m$$

$$\begin{cases} K = 0.158 \\ x = 0.50 \\ y = -1.5 \\ z = 1.85 \\ m = 11/9 \end{cases} \tag{107}$$

where T_b (K) is the normal boiling point of the liquid, T_c (K) and p_c (bar) are critical temperature and pressure and the subscript r refers to reduced temperatures. The parameters listed refer to those polar liquids other than alcohol and acids; Poling et al. (2004) report the percent deviation from the experimental value to be less than 4% for polar compounds such as small chain alcohols and acids. Experimental work is necessary to determine a proper correlation for the surface tension of sugar solutions on temperature and concentration, since this can sometimes be quite different from that of water.

The densities and viscosities have been determined from tables reported in NIST Chemistry WebBook, calculated from EoS and correlations reported respectively in Wagner and Pruss (2002) and IAPWS (1997).

The estimation of the diffusion coefficient of hydrogen in the sugar solution has been determined by means of the Wilke-Chang method reported in Poling, Prausnitz, O'Connell (2004):

$$D_{H_2} = \frac{7.4 \cdot 10^{-8} \left(\Phi \cdot MW_s\right)^{1/2} T}{\mu_s V_{H_2}} \tag{108}$$

where Φ (-) is the association factor of the solvent, MW_s (g/mol) is the molecular weight of the solvent and V_{H2} (cm^3/mol) is the molar volume of the solute H_2 at its normal boiling point, which from was taken from literature as 14.3 cm^3/mol (Meille et al., 2002).

The diffusion coefficient for sugar arabinose in water was calculated with the correlation proposed by Noriko et al. (2007) derived in the temperature range 273.2-353.2K and atmospheric pressure:

$$D_A = 2.224 \cdot 10^{-15} \mu_s{}^{-1.007} T \tag{109}$$

where the units of measure are SI. The effect of pressure on diffusion coefficients in liquid phase has not been taken into account by many authors (Poling et al., 2004) and therefore reliable correlations to extend estimations at pressure higher than atmospheric do not exist. The effect of temperature, if the range of T investigated is small as in our case, is adequately described assuming $(D_A \cdot \mu)/T = constant$ (Poling et al., 2004) as both relations above do. Physical properties of the gas phase pure H_2, i.e. density, viscosity, specific heat and thermal conductivity, at high and

atmospheric pressure were determined for the temperatures and pressures of interest from tables reported in NIST Chemistry WebBook.

The characteristics of the reaction system which were kept constant during the sensitivity analysis on the model parameters were the mass of catalyst used, 0.90 g, with a content of Ru on activated carbon of 0.7%, the reactor diameter, 10 mm, thus giving a bed length of around 30 mm, since the bulk density of the specific catalyst considered is 0.4 g/cm^3. The particles of catalyst used have a diameter of 1 mm (assumed as spheres), while inert particles, normally used to reduce non-uniformity of liquid distribution, improve the wetting efficiency and to reduce the axial dispersion effects in the liquid phase, were considered to be non-porous and to have a diameter of 200μm. It is important to highlight this because this is the size of the particles used for determining the hydrodynamics and mass transfer parameters. As pointed out by Al Dahhan and Dudukovic (1996), hydrodynamics is largely dictated by the smaller inert fines. Finally the porosity of the bed considering only the large catalytic particles was considered to be of 0.40, while the porosity of the bed with the inert fines is 0.25, both values were derived based on common values encountered in literature.

Common features of the NUMOL codes developed for the simulations are here listed:

- for some simulations the computational grid was adapted dynamically with the technique discussed in Section 3.4, while for others the grid was fixed and uniform. The number of nodes used in the former case was around 70, while in the latter could be as high as 200;
- the integration time span has been set at 10^5s to be sure that no effect of the initial conditions could be noticeable on the final solution;
- mass balances and energy balances were always solved in dimensionless form, since this has been proved to reduce appreciably the computational time;
- the tolerances of the ODE solver were fixed tight, in order to ensure that the numerical errors of NUMOL solutions could be attributed mainly to the spatial discretization formulas adopted (see Section 3.3); in particular an absolute tolerance of 10^{-6} and a relative tolerance of 10^{-5} were adopted;
- the ODE solver *ode15s* was used; it is a multistep, variable order solver adapt to face stiff ODE problems. It has been briefly described in Section 3.3.4; an initial trial was conducted using the explicit solver *ode45*, but the integration time was extremely long.
- the spatial discretization formulas adopted to approximate 1st and 2nd spatial derivative were respectively the 4th order upwind approximation that, from what we showed in Section 3.2.4, gives a reasonable trade off between accuracy and stability of the solution especially in the case of problems with a strong convective component, and the 4th order central finite difference approximation for the 2nd derivative, i.e. the approximation of the 2nd derivative calculated directly on the dependent variable, not on its 1st derivative.

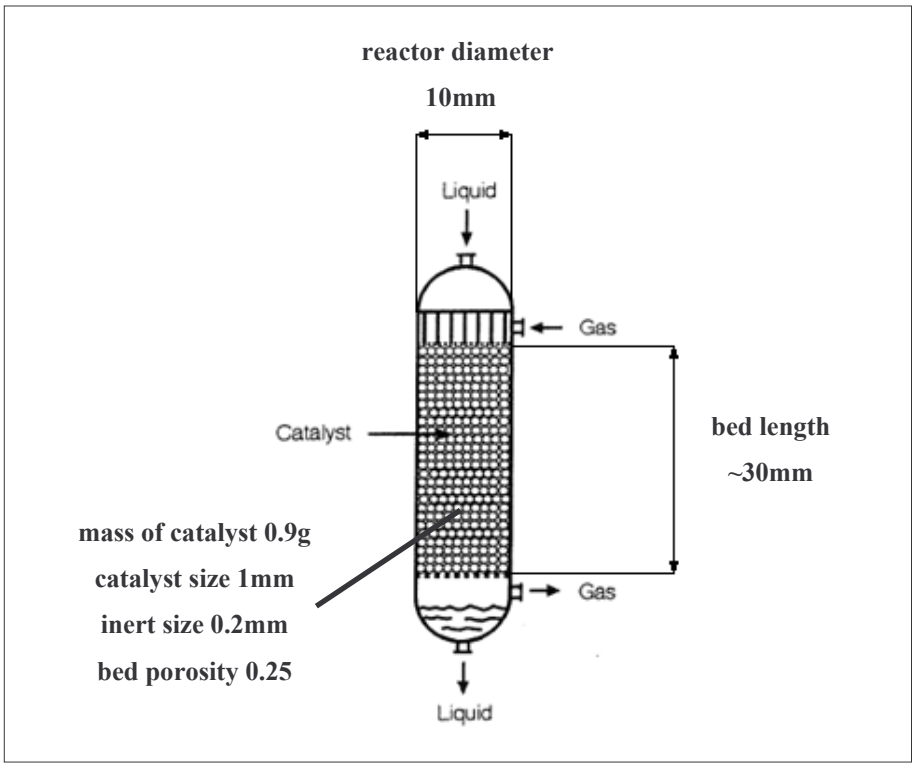

Fig. 24. General characteristics of the small scale trickle bed reactor simulated (adapted from Al Dahhan and Dudukovic, 1996).

In Tab.14, we summarized the characteristics of the different models of a TBR described in the next sections. A detailed description of each model is given in the relative section.

Tab. 14. Characteristics of the different TBR models described in the work.

Section	Pseudo-homogeneous	Heterogeneous	Isothermal	Adiabatic	Internal mass transfer resistance	Catalyst deactivation
4.3.1	●		●			
4.3.2	●		●		●	
4.4		●	●			
4.5	●		●			●
4.6		●		●		

4.3 Isothermal models with effective L/S mass transfer

In this paragraph, we describe models for a trickle-bed reactor (TBR) in which liquid-solid (L/S) mass transfer is assumed to be effective, which means that no differences in the concentration arise between bulk liquid and liquid at the surface of the catalyst particle, as shown schematically in Fig. 25. The reactor is assumed to operate isothermally. Internal mass transfer has been considered as well, since the size of particles considered is typical of commercial catalyst for pilot TBR and can give rise to significant concentration gradients. In Fig. 25a it is assumed that concentration profiles inside the catalyst pellets are flat, i.e. no resistance to the mass transfer inside the pellet exists, while in Fig. 25b the diffusional resistance generates concentration profiles and reduces the working efficiency of the catalyst.

Mixing in liquid phase has been described using three different models, the ideal plug flow and perfectly mixed models and the non-ideal axial dispersion model; the first two were mainly used to define the boundaries for the performance achievable from the numerical solution of the third, solved with the method of lines.

Some general assumptions, commonly encountered in literature, have been made in developing the models:

- no vaporization of the liquid solvent is considered; this is an important assumption especially in the case of an exothermic reaction such as an hydrogenation; in our particular case, sugars are considered non-volatile and, since the sugar hydrogenation is considered to take place at $T \leq 130°C$ and high pressure (up to 50-60 bar), the solvent water could be also reasonably assumed non-volatile, since its vapor pressure at 130°C is 2.70 bar, from NIST Chemistry WebBook;
- the catalyst is completely wet externally; according to Gianetto and Silveston (1986), to have a complete external wetting of a bed of catalyst particles of commercial sizes, the liquid superficial velocity should be, as a rule of thumb, higher than 0.7 cm/s. By the way, when diluting the bed with fines of typical diameter about 200μm, wetting efficiency improves noticeably, as showed by Al Dahhan and Dudukovic (1996), Metaxas and Papayannakos (2008) and Mary et al. (2009); Metaxas and Papayannakos (2008) estimated the wetting efficiency for their small-scale TBR described in Section 2.6 to be about 1, even for coarse bed diluent of about 2mm diameter. Thus the hypothesis made in the modelling of our small-scale trickle bed reactor seems to be a rather reasonable approximation; moreover the empirical criterion reported in Section 2.4 has been used to check for each simulation the adequacy of wetting. In each case the criterion was fulfilled for the particular conditions simulated;

- the hydrogen concentration in the gas phase is assumed uniform along the reactor, which is a reasonable in the case of a pure hydrogen stream, if the pressure is almost uniform along the reactor and the molar rate of absorbed H2 is small respect to the incoming molar rate; we will show subsequently that the overall two-phase pressure drop estimated by means of the correlation of Larachi et al. (1991) is around than 0.05 bar for u_L=0.05cm/s and T=80°C (temperature at which liquid viscosity is at its peak), being about 0.5% of the pressure of hydrogen in the reactor. This assumption allows to simplify the overall model, avoiding to solve mass balances for the gas phase.

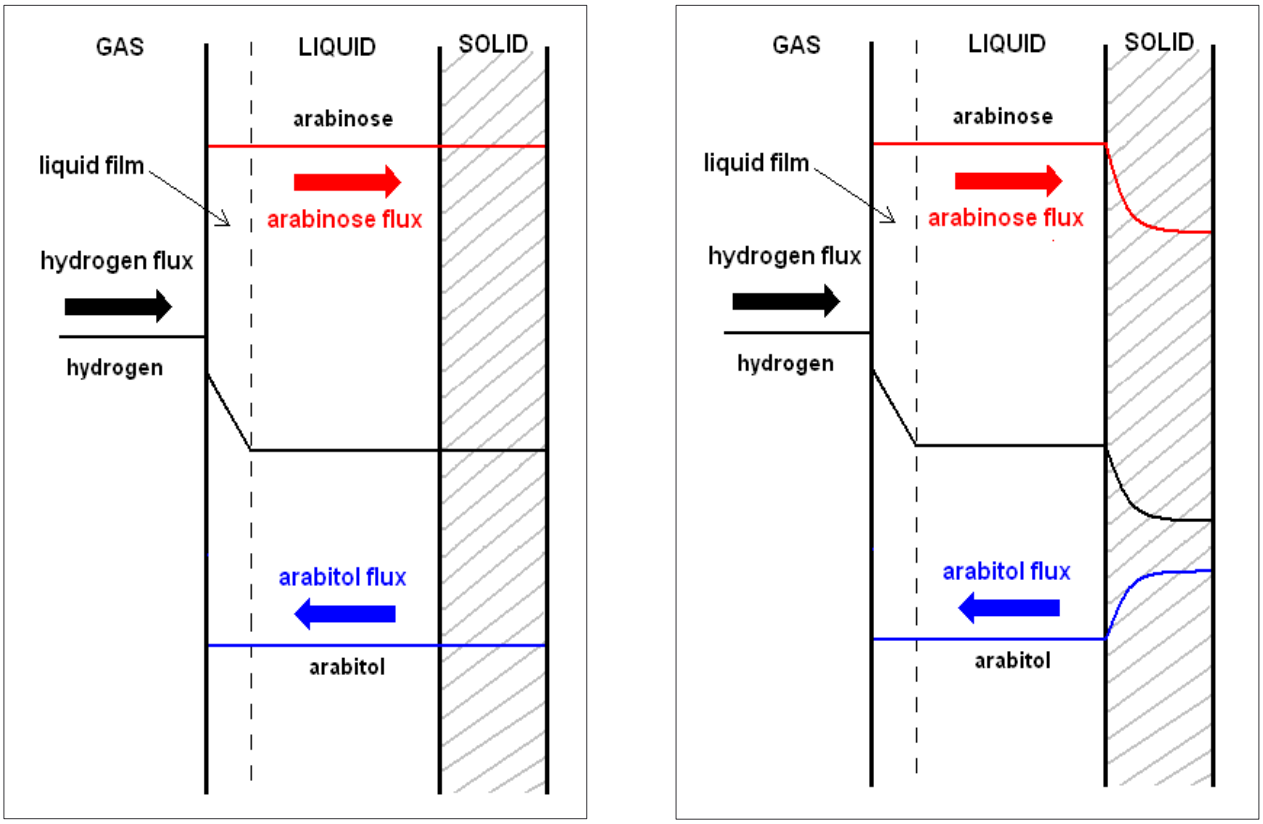

Fig. 25. Concentration profiles in the gas, liquid and solid phase
(a) no intraparticle mass transfer resistance, b) with intraparticle mass transfer resistance).

4.3.1 Models with negligible internal mass transfer resistance

As highlighted above, we are considering models which assume that the transport of the chemical species in the liquid phase is effective, thus no concentration gradients exist between the bulk liquid and the liquid at the surface of the catalyst. In this subsection, we consider the simplest case, in which no resistance to the mass transfer of species inside the catalyst particles exists, so concentrations everywhere inside is equal to that at the surface and it is not necessary to solve any mass balance in the catalyst.

If we describe the liquid phase with a 1-D axial dispersion model, the dynamic equations of the model are written as follows:

$$\begin{aligned}
\varepsilon_L \frac{\partial c_{H_2}}{\partial t} &= D_{ax} \frac{\partial^2 c_{H_2}}{\partial x^2} - u_L \frac{\partial c_{H_2}}{\partial x} + k_{GL} a \left(c_{H_2,L}^{\ *} - c_{H_2} \right) - \frac{k K_A K_{H_2} c_A c_{H_2}}{\left(1 + K_{H_2} c_{H_2} + K_A c_A + K_B c_B \right)^2} \\
\varepsilon_L \frac{\partial c_A}{\partial t} &= D_{ax} \frac{\partial^2 c_A}{\partial x^2} - u_L \frac{\partial c_A}{\partial x} - \frac{k K_A K_{H_2} c_A c_{H_2}}{\left(1 + K_{H_2} c_{H_2} + K_A c_A + K_B c_B \right)^2} \\
\varepsilon_L \frac{\partial c_B}{\partial t} &= D_{ax} \frac{\partial^2 c_B}{\partial x^2} - u_L \frac{\partial c_B}{\partial x} + \frac{k K_A K_{H_2} c_A c_{H_2}}{\left(1 + K_{H_2} c_{H_2} + K_A c_A + K_B c_B \right)^2}
\end{aligned} \tag{110}$$

where x (m) is the axial coordinate of the reactor, D_{ax} (m^2/s) is the axial dispersion coefficient of the liquid phase and k ($mol/m^3_{bed} \cdot s$) is the kinetic constant derived as described in Section 4.1 multiplied by the content of active metal Ru in the catalyst (0.7%), the density of the catalyst particle and the ratio between the volume occupied by catalyst and the total bed volume; in mathematical terms we have:

$$k \left(\frac{mol}{m^3_{bed} \cdot s} \right) = k \left(\frac{mol}{g_{Ru} \cdot s} \right) \cdot \frac{g_{Ru}}{g_{particle}} \cdot \left. \frac{g}{m^3} \right|_{particle} \frac{m^3_{particle}}{m^3_{bed}} \tag{111}$$

Boundary conditions are those of Danckwerts:

$$\begin{aligned}
\frac{\partial c_i}{\partial x}(0,t) &= \frac{u_L}{D_{ax}} \left(c_i(0,t) - c_i^{IN} \right) \\
\frac{\partial c_i}{\partial x}(L_B,t) &= 0
\end{aligned} \tag{112}$$

where i refer to the generic species; note that if the left-boundary condition is rewritten in dimensionless form, the ratio u_L/D_{ax} turns out to be the Peclè number Pe. The initial conditions could be fixed arbitrarily, since as we showed in Section 3.1 with the method of false transients, they do not affect the steady state solution, provided that the time interval on which we integrate the ODEs is sufficiently large. In Eq. (110) only the mass balances of H_2, A and B are reported, since the reactor is assumed to be isothermal: we can discern the dispersion term, the convective term and the reaction term in each of them, while in the H_2 mass balance there is also the gas-liquid (G/L) mass transfer term, since H_2 is supplied from gas to liquid phase in order for the reaction to take place. Danckwerts boundary conditions assume continuity of the flux at the reactor inlet, with negligible dispersion outside the reactor, and impose that concentration gradients disappear at the reactor outlet.

The evaluation of the G/L mass transfer coefficient is a hard task without having experimental data on which testing experimental correlations; as stated in Section 2.6 one correlation was selected, the Ellman (1988), which gives estimations of the mass transfer coefficient more close to the experimental values determined by Metaxas and Papayannakos (2006) for a system very similar to ours. In particular, from

what will be reported in Section 4.5, the predictions from Ellman (1988) have been corrected by a factor 1/2.

Both the total liquid hold-up ε_L and the two-phase pressure drop have been estimated by means of the correlations of Larachi et al. (1991); to assess the importance of axial dispersion in the liquid phase, empirical criteria presented in Sec. 2.5 were used and for the particular reactor setup considered they gave:

$$\begin{aligned} &\frac{L_B}{d_p} \sim 140 \\ &\frac{d_R}{d_p} = 50 \end{aligned} \tag{113}$$

since the right particle dimension to be considered is that of the fines. The 2nd criterion is satisfied (d_R/d_p should be larger than 10), as well as the 1st one (L_B/d_p should be greater than 100); we conducted some sensitivities with this model of reactor, showing that a reasonable choice for liquid Pe can be 20, since for this value we are already close to the upper conversion limit typical of a PF liquid phase.

To fix the upper and lower limit of the performance of the TBR, the plug flow and the perfectly mixed models were also used. The mass balances for plug flow model are reported subsequently:

$$\begin{aligned} u_L \frac{\partial c_{H_2}}{\partial x} &= k_{GL} a \left(c_{H_2,L}{}^{*} - c_{H_2} \right) - \frac{k K_A K_{H_2} c_A c_{H_2}}{\left(1 + K_{H_2} c_{H_2} + K_A c_A + K_B c_B \right)^2} \\ u_L \frac{\partial c_A}{\partial x} &= - \frac{k K_A K_{H_2} c_A c_{H_2}}{\left(1 + K_{H_2} c_{H_2} + K_A c_A + K_B c_B \right)^2} \\ u_L \frac{\partial c_B}{\partial x} &= + \frac{k K_A K_{H_2} c_A c_{H_2}}{\left(1 + K_{H_2} c_{H_2} + K_A c_A + K_B c_B \right)^2} \end{aligned} \tag{114}$$

with the boundary condition:

$$c_i(0) = c_i{}^{IN} \tag{115}$$

The dynamic term does not appear, since this is a simple non-linear ODE system which does not require a NUMOL procedure to be solved, but just forward numerical integration in the space. Again we note the convective term in the left-hand side and the reaction term at the right-hand side of Eqs. (114), while the mass transfer term appears only in the H_2 mass balance. It was verified that they could be solved both by a stiff solver and by an explicit solver.

The mass balances in the liquid phase for the perfectly mixed model are:

$$\begin{aligned} \frac{c_{H_2} - c_{H_2}{}^{IN}}{\tau} &= k_{GL} a \left(c_{H_2,L}{}^{*} - c_{H_2} \right) - \frac{k K_A K_{H_2} c_A c_{H_2}}{\left(1 + K_{H_2} c_{H_2} + K_A c_A + K_B c_B \right)^2} \\ \frac{c_A - c_A{}^{IN}}{\tau} &= - \frac{k K_A K_{H_2} c_A c_{H_2}}{\left(1 + K_{H_2} c_{H_2} + K_A c_A + K_B c_B \right)^2} \\ \frac{c_B - c_B{}^{IN}}{\tau} &= \frac{k K_A K_{H_2} c_A c_{H_2}}{\left(1 + K_{H_2} c_{H_2} + K_A c_A + K_B c_B \right)^2} \end{aligned} \tag{116}$$

where τ (s) is the liquid residence time. They were solved by *MatLab 7.1* non-linear equations solver *fsolve*, based on a trust region dogleg algorithm.

Sensitivity analysis was conducted to evaluate the effect on the reactor performance of temperature, pressure, liquid and gas superficial velocity and Peclét number. Also the concentration of H_2 in the feed was varied, since it has been revealed to have significant impact. We report some of the most interesting conversion (X_A) trends obtained together with the values of operation conditions and parameters used. The reactor was kept in the trickle flow regime during the simulations choosing appropriate values of liquid and gas superficial velocities, since correlations used refer to this particular hydrodynamic flow regime. The criteria of Larachi et al. (1993) and Fukushima and Kusaka (1977) were used jointly.

Adaptive grids were employed particularly when concentration profiles showed large gradients, in order to gain sufficient accuracy.

Tab. 15. Operation conditions and parameters used for sensitivity analysis on temperature.

operation condition / parameter	value
p (bar)	40
u_L (cm/s)	0.05
u_G (cm/s)	5
fs (-)	1
Pe (-)	20

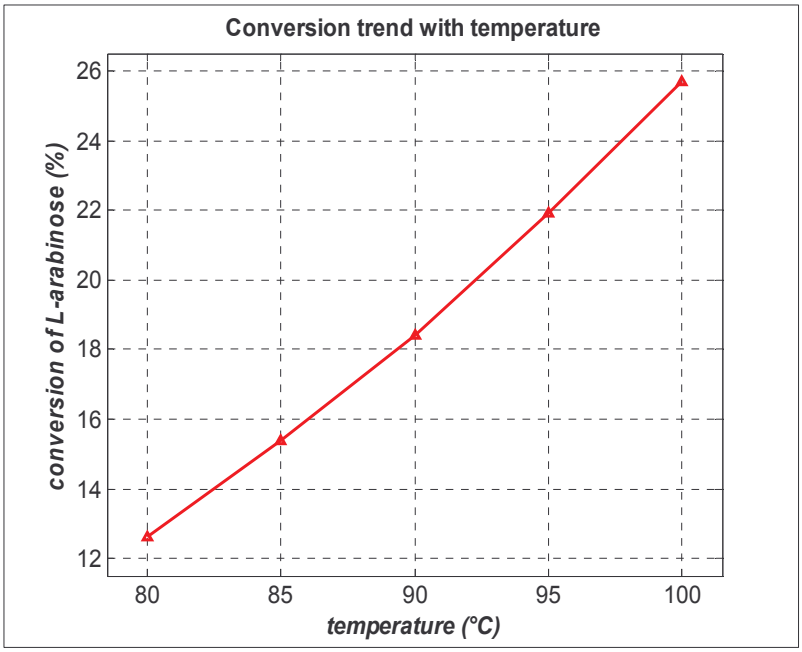

Fig. 26. Trend of the sugar conversion with the temperature for the axial dispersion TBR model.

In Tab. 15, the operation conditions and parameters used in the simulations of the reactor for different values of temperature are reported; the parameter *fs* is the ratio between the inlet concentration of H_2 in the liquid and its saturation concentration at the same conditions.

In Fig. 26, the trend of the conversion with temperature in the range 80-100°C is reported. The temperature range investigated is limited by the considerations made in Section 4.1.

We obtain conversions in the range 10-30%, not very high because of the small mass of catalyst used and of G/L mass transfer limitation, as we can see from the concentration profiles at 100°C along the bed (Fig. 27a, concentration of H_2 has been divided by $c_{H2,L}^{*}$, while concentration of A and B for $c_{A,L}^{IN}$), where a consistent fall of H_2 concentration takes place within 10% of the bed length (remember that the liquid phase enters saturated in H_2). The hydrogenation reaction shows to be effective even at these low temperatures, as already revealed by Sifontes et al. (2010). Axial dispersion does not affect significantly performances for these particular conditions, most probably because of the low conversions achieved; note that the different trends of the profiles of H_2 and A, both consumed by the reaction with stoichiometric coefficient -1, are due to the different phenomena controlling the concentration of the two species in the liquid phase, G/L mass transfer and reaction for H_2, only reaction for A.

H_2 can be supplied to liquid phase by feeding a saturated liquid phase and of course by interfacial mass transfer; to determine the contribution of the G/L mass transfer to the quantity of H_2 being available for the reaction in the liquid phase, the following balance was made: since 1 mol of H_2 reacts to give exactly 1 mol of L-arabitol (the selectivity has been shown to be 100% for L-arabinose to L-arabitol by the kinetic study Sifontes et al. (2010)), to obtain the mass-transfer contribution we must subtract the molar rate of H_2 entering the reactor with the liquid feed to the sum of the molar rate of H_2 consumed (equivalent to the molar rate of B produced) and the molar rate of H_2 left in liquid phase at the outlet. In other terms:

$$Q \cdot [fs \cdot c_{H_2,L}^{*} - (c_{B,L}^{OUT} + c_{H_2,L}^{OUT})] = -k_{GL}a \cdot \int \left(c_{H_2,L}^{*} - c_{H_2,L} \right) dx \cdot A_R \qquad (117)$$

We can also evaluate separately the two terms of the balance, solving the integral at the right hand side with *MatLab* function *trapz*, which implements trapezoidal numerical integration, and compare them to get an idea of the accuracy of the numerical method used to solve the differential system; the contribution of G/L mass transfer at different temperatures is shown in 2nd column of Tab. 16, expressed as % of the total molar rate of H_2 available to reaction in liquid phase. We have that the G/L mass transfer contribution, although limiting, is determinant to reach the performance shown. The increase of mass transfer contribution with temperature is due to the fact that besides k_La increase with

temperature, also the concentration difference between the interfacial liquid and bulk liquid increases, leading to a more intense enhancement.

The 3rd column reports the percent relative closure errors of the balance (117), which are satisfying. Finally, in order to check the assumption of uniform pressure of H_2 along the bed, which has allowed not to solve gas phase mass balances, the ratio between the molar rate of H_2 which absorbs in the liquid phase and the total molar rate of gaseous H_2 entering the reactor has been calculated and reported in the 4th column of Tab. 16; as we see, ratios are very low, thus the reduction in pressure along the bed due to H_2 consumption by the reaction is negligible.

Adaptive grids were used in the simulations, although also uniform grids gave accurate results.

Tab. 16. Contributions of the gas-liquid mass transfer to H_2 availability in the liquid phase and comparison between the molar rate of H_2 absorbed and the total H_2 gas flowrate.

temperature (°C)	mass transfer contribution (%)	relative closure (%)	absorbed H_2 on total gaseous H_2 (-)
80	79.1	0.023	0.6e-3
85	81.2	0.025	0.6e-3
90	83.0	0.028	0.8e-3
95	84.5	0.030	1.0e-3
100	85.8	0.031	1.1e-3

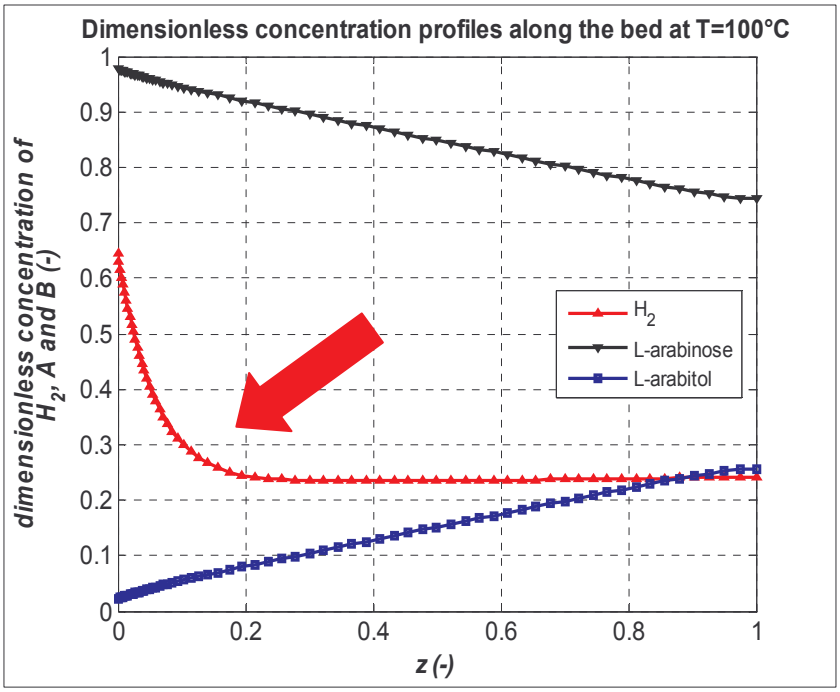

a)

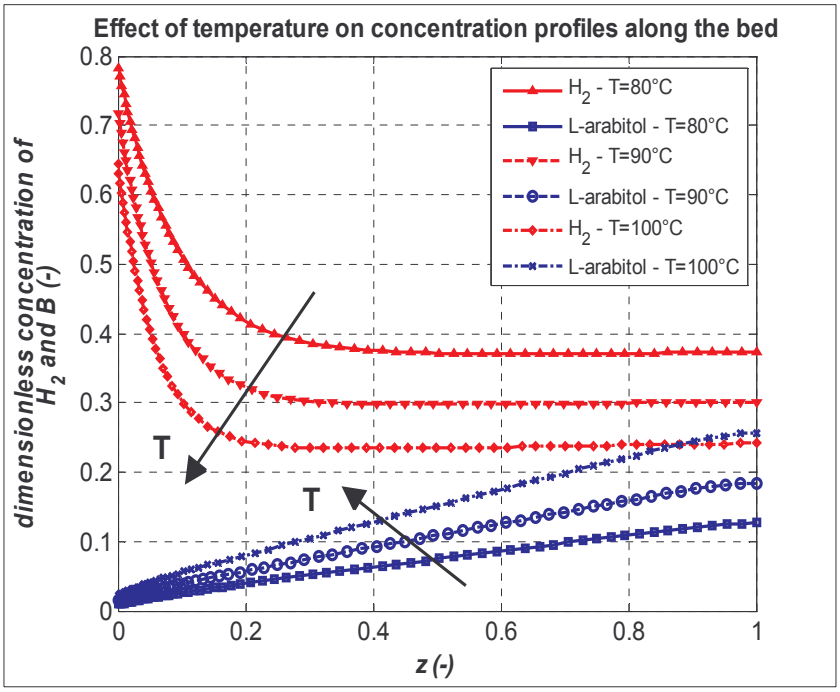

b)

Fig. 27. a) Concentration profiles along the bed at 100°C and b) concentration profiles along the bed at different temperatures.

From Fig. 27b we can see the effect of temperature on the consumption of H_2 in liquid phase; the higher the temperature, the more intense is the intrinsic reaction, both for a more considerable increase of the kinetic constant with temperature respect to the G/L mass transfer coefficient and for the increase of the H_2 content in the saturated feed, therefore H_2 concentration in the liquid phase along the bed decreases, because of the enhanced mass transfer limitation.

The effect of feeding the liquid phase saturated with H_2 can be seen from Tab. 17, where conversions obtained feeding a H_2-saturated liquid phase and a liquid feed with no H_2 solubilized are compared. As expected from the results in Tab. 16, there's little advantage in feeding a solution saturated with H_2, as it is the G/L mass transfer that mostly contributes to the supplying of H_2 in the liquid phase.

Tab. 17. Importance of feeding a liquid phase saturated in hydrogen.

temperature (°C)	X_A (%) – saturated feed	X_A (%) – non saturated feed
80	12.6	10.9
90	18.4	16.2
100	25.7	22.9

Tab. 18. Operation conditions and parameters used for sensitivity analysis on liquid superficial velocity.

operation condition / parameter	value
T (°C)	100
p (bar)	40
u_G (cm/s)	5
fs (-)	1
Pe (-)	20

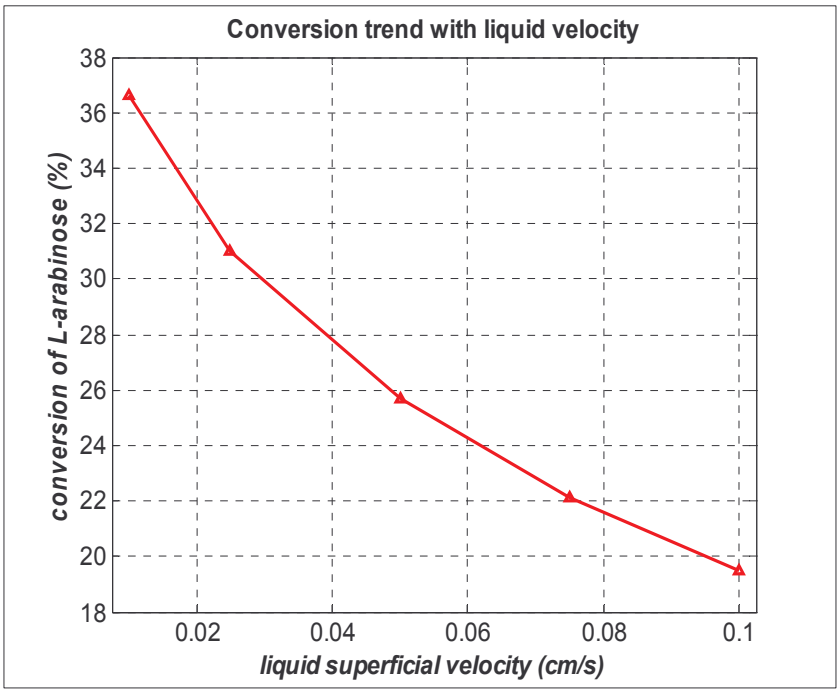

Fig. 28. Trend of the sugar conversion with the liquid superficial velocity for the axial dispersion TBR model.

Tab. 18 reports the operation conditions and parameters used in simulations with a variable liquid superficial velocity. In Fig. 28 the trend of the conversion with the liquid superficial velocity is reported; with an increasing liquid velocity, the performance of the reactor impairs. In fact, u_L has two major effects, the reduction of the liquid residence time and the local improvement of the mass transfer rate. The shorter liquid residence time in the reactor leads to a lower conversion; so, since our reactor operates in mass transfer controlled regime, if we extend the bed length to maintain a constant liquid space velocity (LSV), we would obtain higher conversion while increasing u_L. We can state that the local increase of the overall reaction rate due to the improvement of mass transfer is not large enough to compensate the reduction in residence time.

Thus low liquid velocities seem to be preferable to achieve higher conversions in our system, although this penalizes the mass transfer. Other ways to boost it are necessary, such as for example increasing the gas velocity. Pressure drop increases rapidly with u_L going from about 70mbar for u_L=0.01cm/s to 190mbar for u_L =0.1cm/s, not more than 0.5% of the overall pressure as said previously.

The concentration profiles of H_2 along the bed for different u_L are plotted in Fig. 29a. We clearly see that increasing u_L, G/L mass transfer improves, because the H_2 concentration in liquid phase stabilizes at higher values all along the reactor, but the overall performance decays as we see from the lowering concentration profiles of L-arabitol. Thanks to the use of inert particles of 200μm of diameter, the criterion for adequate catalyst wetting results satisfied even for the lower liquid velocity; thus the assumption of complete wetting of the catalyst used in the modeling is rather reasonable. In Fig. 29 we see the importance of the implementation of a grid adaptation algorithm especially for simulations using low liquid velocity and high temperature, which determine a rapid decay of H_2 concentration at the beginning of the reactor. The grid points end to be more tight just after the reactor inlet section, where H_2 concentration gradient is larger.

In Tab. 19 below operative conditions and parameters used in sensitivities to gas superficial velocity are given.

In Fig. 30a trends of L-arabinose conversion with the gas superficial velocity are reported; as expected, the effect of u_G on mass transfer coefficients and thus on the performance is very significant. Increasing u_G, the interaction between phases improves and more H_2 is transferred to liquid phase section by section, leading to a higher c_{H2} in the liquid phase and so to the enhancing of the intrinsic reaction rate as showed in Fig. 30b.

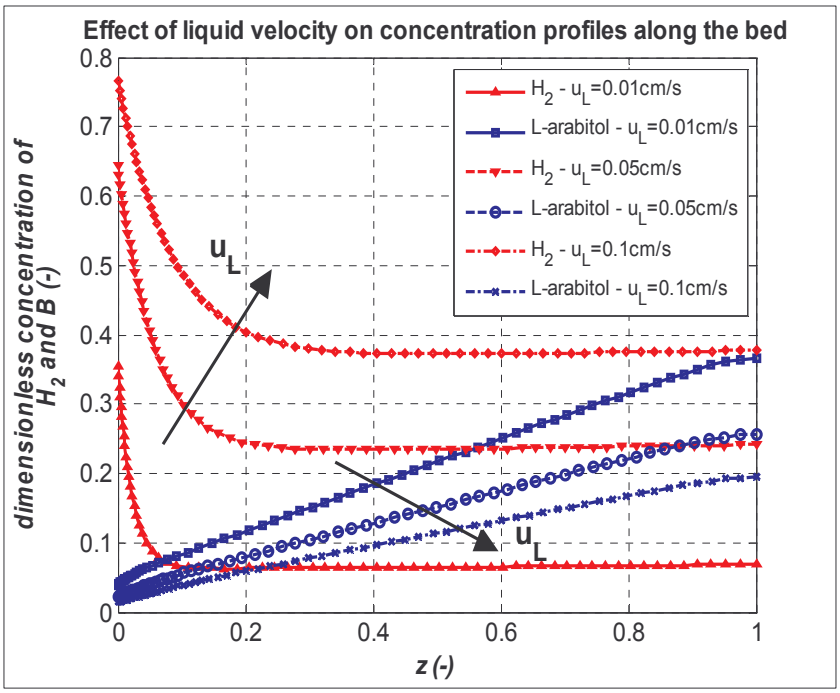

a)

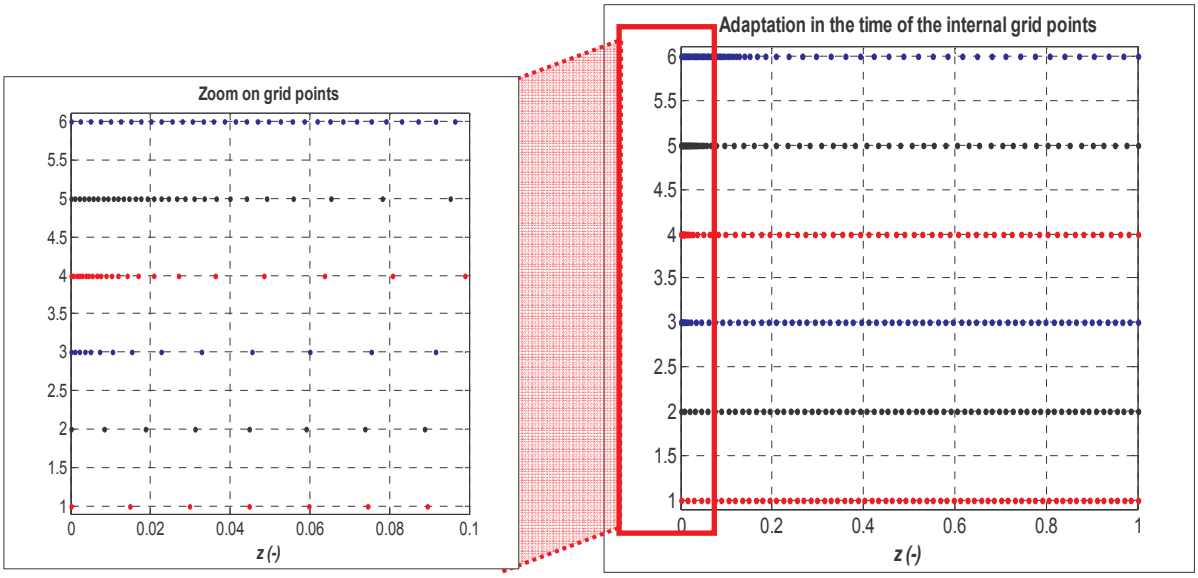

b)

Fig. 29. a) Concentration profiles along the bed for different liquid superficial velocities and b) spatial grid adaptation evolving during the solution procedure.

Tab. 19. Operation conditions and parameters used for sensitivity analysis on gas superficial velocity.

operation condition / parameter	value
T (°C)	100
p (bar)	40
u_L (cm/s)	0.05
fs (-)	1
Pe	20

Oppositely to an increase of u_L, the raise of u_G has little effect on the residence time of the liquid phase; in fact the liquid hold-up does not decrease significantly passing from 1 to 10 cm/s (see Section 2.9), thus the residence time reduction is almost negligible.

The contribution of the G/L transport to the H_2 available for the reaction jumps from 70% when u_G = 1cm/s to 90% for u_G = 10cm/s; another aspect to note is that based on the correlation of Larachi et al. (1991), pressure drop increases much more slowly with u_G than with u_L (approximately 0.7 mbar/mm/s against 140 mbar/mm/s for u_L) and since the two phases flow cocurrently, there is no flooding.

Therefore increasing u_G, especially when strong mass transfer limitation occurs, is a practical way to improve the performance, according to the phenomenological models on the effect of u_G on k_La described in Chapter 2. Metaxas and Papayannakos (2006) observed experimentally in their bench-scale laboratory system of characteristic very close to our a very strong dependence of k_La on the gas superficial velocity.

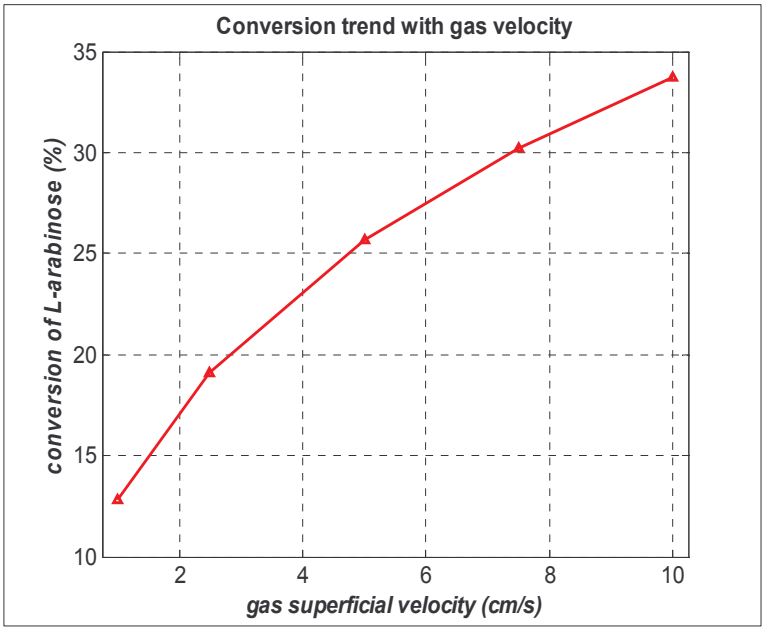

a)

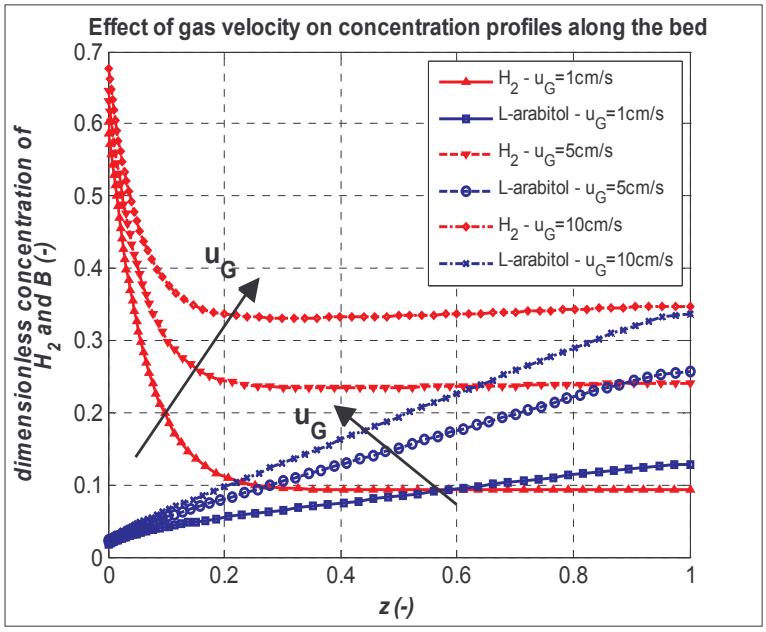

b)

Fig. 30. a) Trend of the sugar conversion with the gas superficial velocity for the axial dispersion TBR model and b) concentration profiles along the bed for different superficial velocities of the gas phase.

4.3.2 Models with significant internal mass transfer resistance

The intraparticle (or internal) mass transfer resistance can be an important issue in the transport of the species to the active catalyst sites when the intrinsic reaction rate is high and/or the size of the catalyst particles is significant (as in the case of a TBR). Due to this resistance, concentrations inside the particles are lower than that at the surface and this, for the most common kinetic expressions, leads to observed reaction rate lower than that expected at the bulk concentrations. To take into account this resistance in the reactor simulation, it

is possible to use an effectiveness factor η of the catalyst, defined as the ratio of the actual/observed rate of reaction to the reaction rate at the surface conditions (concentration and temperature) (Missen et al., 1999; Salmi et al., 2010):

$$\eta_i = \frac{N_i^{obs}\left(r = R_p\right)\cdot A_p}{r_i\left(\bar{c}^{surface}, T^{surface}\right)\cdot V_p} \tag{118}$$

where N_i^{obs} (mol/m^{2}s) is the diffusive molar flux of the component *i* observed at the surface that is affected by the diffusional resistance inside the particle, R_p (m) is the particle radius, A_p (m^2) is the external surface of the particle which is invested by the molar flux, r_i (mol/m$^3_{cat}$s) is the rate of consumption or production of component *i*, V_p (m^3) is the volume of the particle and the notation *surface* refers to concentrations and temperature at the external surface of the catalyst. The bar above *c* indicates that in general r_i is function of concentrations of different species. With some passages, reported in Salmi et al. (2010), a more practical expression can be derived:

$$\eta = \frac{\int_0^{V_{particle}} R\left(\bar{c}^{inside}, T^{inside}\right) dV}{R\left(\bar{c}^{surface}, T^{surface}\right)\cdot V_{particle}} \tag{119}$$

where R (mol/m$^3_{cat}$s) is the reaction rate that should be calculated as a function of the concentrations and temperature profiles inside the particle or of the concentrations and temperature at the surface.
For simple kinetics the effectiveness factor can be calculated analytically as a function of the Thiele modulus Φ, dimensionless number that tells us how strong is the diffusional resistance inside the catalyst particle compared to the reaction rate. For a nth order irreversible kinetics in the reactant A and spherical particle of radius R_p, Φ and η are expressed as (Missen et al., 1999):

$$\begin{aligned} \Phi &= R_p\left(\frac{k\cdot {c_A}^{n-1}}{D_{eff}}\frac{n+1}{2}\right)^{1/2} \\ \eta &= \frac{3}{\Phi}\left(\frac{1}{\tanh\left(\Phi\right)} - \frac{1}{\Phi}\right) \end{aligned} \tag{120}$$

where D_{eff} (m^2/s) is the effective diffusion coefficient, a property of each species in a specific catalyst particle; for a given value of *k*, large values of D_{eff} give small Φ, which means negligible internal mass transfer limitation (transport by diffusion is able to sustain the reaction), while large Φ denote strong internal mass transfer resistance. D_{eff} is usually estimated from the random pore model (Missen et al., 1999):

$$D_{eff} = D\frac{\varepsilon_p}{\tau_p} \tag{121}$$

where D (m^2/s) is the diffusion coefficient (normally a combination of molecular and Knudsen diffusion coefficients, since it is possible that both kind of molecular transport of chemical species

take place in a catalyst particle), ε_p (m^3_{void}/m^3_{cat}) is the internal porosity of the catalyst particle and τ_p (-) is the tortuosity factor. These two factors allow to take into account the fact that only a portion of the particle is permeable to the species and the path is random and tortuous. Typical values of τ_p are between 3 and 7 (Missen et al., 1999).

In the present work, in order to account for internal mass transfer limitations the following procedure shown in Fig. 31 was adopted.

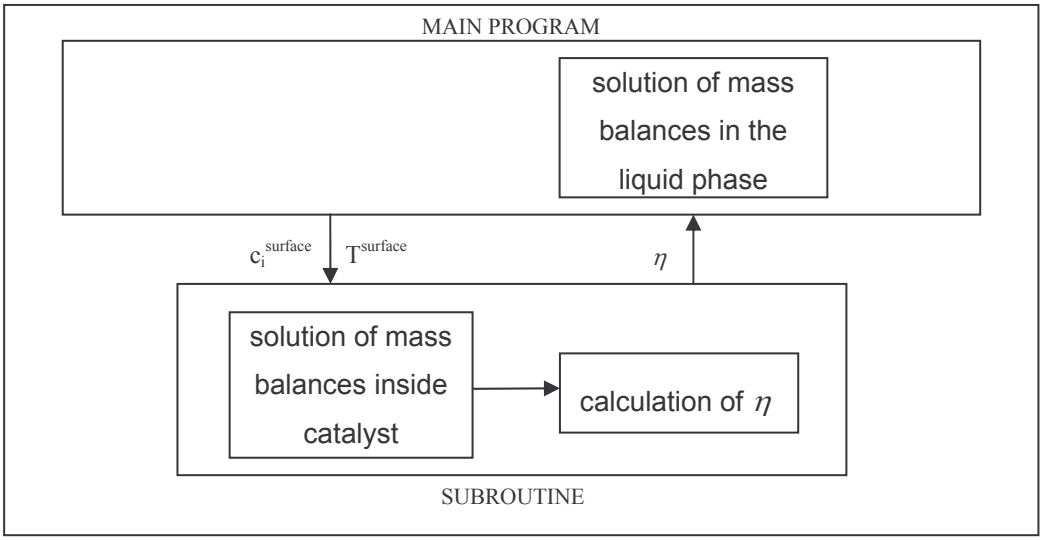

Fig. 31. Procedure for the inclusion of the internal mass transfer resistance in the reactor simulation.

An analytical form of Φ for the particular Langmuir-Hinshelwood rate expression used does not exist, so the only way to calculate η is to solve numerically the mass balances inside the isothermal particle, obtain the concentration profiles and apply Eq. (119). Let us focus on the mass balance for component A inside the porous catalyst particle and on the numerical method used to solve it, proposed by Hoyos et al. (2004). The most important assumptions made are:

- particles are all assumed to be spherical;
- physical and transport properties are uniform along the particle;
- diffusion coefficient of H_2 is calculated from Eq. (108) while the one of the sugar and sugar alcohol molecules are calculated with Eq. (109), and are almost 1 order of magnitude smaller than the one of H_2, since these molecules are much larger;
- effective diffusion coefficients have been calculated from Eq. (121), assuming an internal porosity of the catalyst of 0.5 and varying τ during the sensitivities.

The steady state 1-D diffusion and reaction model for component A in an isothermal spherical particle is:

$$\begin{cases} 0 = \dfrac{D_{eff,A}}{r^2}\dfrac{d}{dr}\left(r^2\dfrac{dc_A}{dr}\right) + r_A \\ c_A\left(R_p\right) = c_A{}^s \\ \dfrac{dc_A}{dr}(0) = 0 \end{cases} \tag{122}$$

It is noteworthy that the reference volume on which the mass balance is made is the particle volume. Using dimensionless variables $f_A=c_A/c_A{}^s$ and $x=r/R_p$, substituting r_A with the rate expression used in this work, approximating 1st and 2nd derivative respectively with 2nd order central finite difference approximation for 1st derivative and 2nd derivative and highlighting $f_A(x_{i+1})$, one obtains:

$$f_A\left(x_{i+1}\right) = \frac{x\dfrac{f_A\left(x_{i-1}\right)}{\Delta x} + x^2\dfrac{2f_A\left(x_i\right) - f_A\left(x_{i-1}\right)}{\Delta x^2} + \dfrac{R_p{}^2x^2c_{H_2}{}^s}{D_{eff,A}}\dfrac{kK_AK_{H_2}f_A\left(x_i\right)f_{H_2}\left(x_i\right)}{\left(1+K_Ac_A{}^sf_A\left(x_i\right)+K_Bc_B{}^sf_B\left(x_i\right)+K_{H_2}c_{H_2}{}^sf_{H_2}\left(x_i\right)\right)^2}}{\dfrac{x}{\Delta x}+\left(\dfrac{x}{\Delta x}\right)^2} \tag{123}$$

Analogously one can derive the expressions for $f_{H2}(x_{i+1})$ and $f_B(x_{i+1})$. The particle radius must be divided in N-1 intervals, so that one can solve a system of 3xN non-linear equations in $f_A(x_i)$, $f_{H2}(x_i)$ and $f_B(x_i)$ with a solver for non-linear equations. An initial estimate of the 3xN unknowns is required; to include the boundary conditions in the system the mass balances for the node at the centre of the particle ($r=0$) and for that at the surface ($r=R_p$) are substituted respectively by:

$$\begin{aligned} &\frac{f(2)-f(1)}{\Delta x} = 0 \\ &f(N) = 1 \end{aligned} \tag{124}$$

where f is each one of the three dimensionless concentrations.

Once solved the mass balances, the effectiveness factor can be calculated from the concentration profiles. The expression used for an isothermal particle was:

$$\eta = \frac{\displaystyle\int_0^{R_p}\frac{kK_AK_{H_2}c_A\left(r\right)c_{H_2}\left(r\right)}{\left(1+K_Ac_A\left(r\right)+K_Bc_B\left(r\right)+K_{H_2}c_{H_2}\left(r\right)\right)^2}r^2dr}{\dfrac{kK_AK_{H_2}c_A{}^sc_{H_2}{}^s}{\left(1+K_Ac_A{}^s+K_Bc_B{}^s+K_{H_2}c_{H_2}{}^s\right)^2}\dfrac{R_p{}^3}{3}} \tag{125}$$

that can be readily derived from Eq. (119). To test the reliability of this method, an nth order irreversible kinetic was considered and the value of the effectiveness factor obtained analytically (Eq. (120)) was compared with the numerical one. Some results are reported for a 2nd order kinetics (preexponential factor A=1e6 m^3/mol·s, activation energy E_a=55 kJ/mol, T=90°C, $c_A{}^s$=6 mol/m^3) in Fig. 32; as it is expected, increasing the size of the particle, the internal mass transfer resistance increases, the profiles become steeper and the working effectiveness of the catalyst declines. We also see that in this case, 41 nodes are

sufficient to obtain an acceptable correspondence between analytical and numerical values of the effectiveness factor. Increasing the number of nodes obviously allows to enhance the accuracy of the numerical solution, but strongly affect the calculation time; in the sensitivity analysis that follow, we used N=51 to solve the mass balances in the catalyst.

The algorithm outlined before for the calculation of effectiveness factor receives the set of bulk concentrations, generates the profiles, calculate and return the effectiveness factor, as represented in Fig. 31. In this way, η is used to correct reaction rate expressions in the mass balances in the liquid phase.

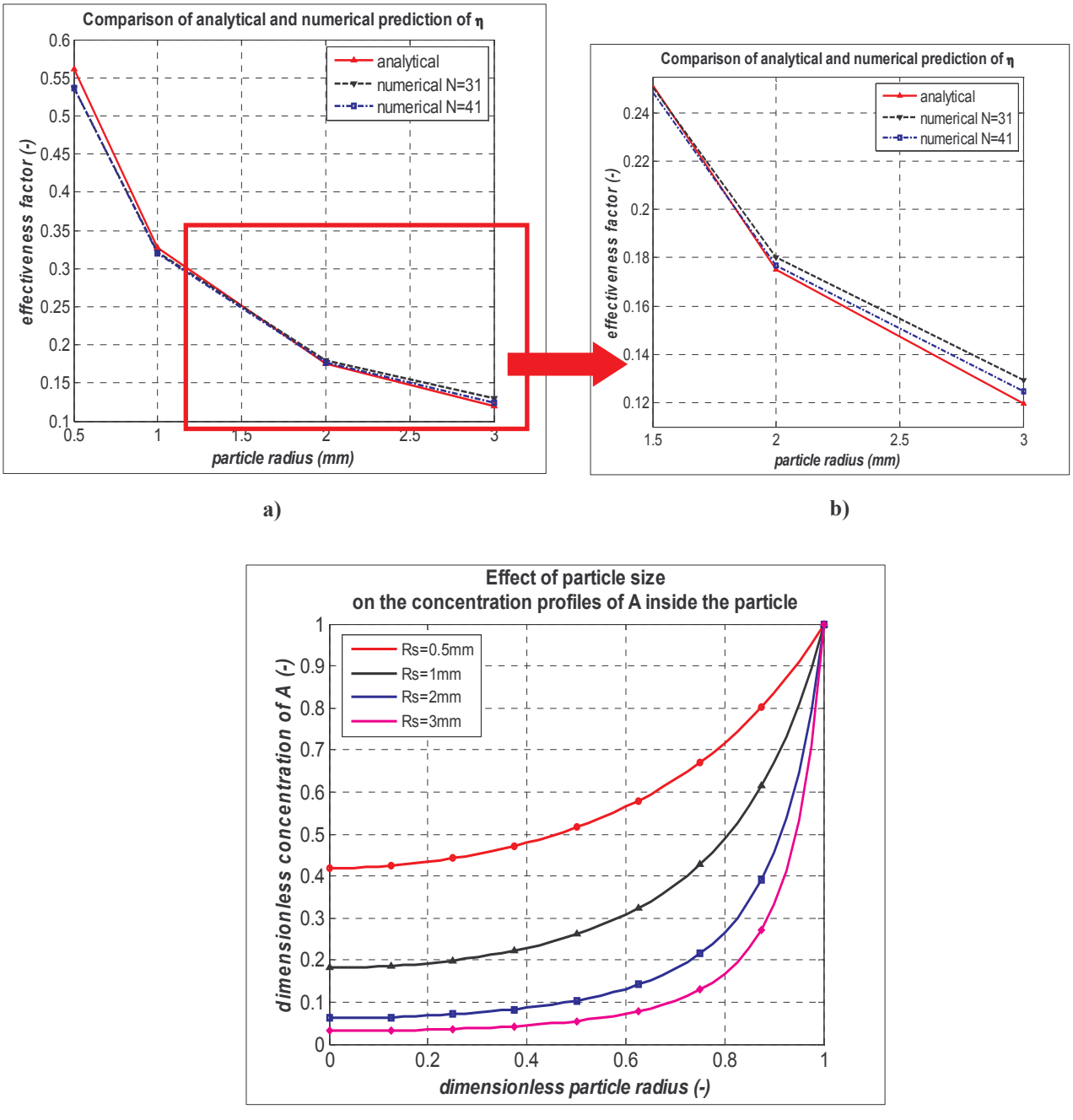

Fig. 32. a) Comparison of analytical and numerical effectiveness factors for different number of nodes *N*, b) particular of a), c) concentration profiles of A inside the catalyst for different particle sizes.

The mass balances in the liquid phase reported previously in Section 4.3.1 must be corrected multiplying the reaction rate term by the effectiveness factor.

Studying the effect of the particle size on the working efficiency of our catalyst (0.7%wt Ru on activated carbon), we obtained the results shown in Fig. 33, using, in absence of better characterization, typical values for τ and $\varepsilon_{particle}$ such as 5 and 0.5 respectively; the simulation refers to a temperature T=100°C and the concentrations of H_2, A and B at the surface have been derived from Fig. 27a at z=0.5. It is evident that catalysts of commercial size (≥ 1mm) create strong diffusion limitations, with catalyst effectiveness factors as low as 0.20. Crushing the catalytic particles to 200μm, the working efficiency of the particle increases significantly to 0.75; therefore it is not strictly necessary to model internal mass transfer resistance when using crushed catalyst of less than 200 μm (as reported also in Sifontes et al. (2010)), while it is important to take into account this further transport resistance when using commercial size catalysts.

Conducting simulations at different temperatures by using 1mm catalytic particles, we obtained the results shown in Fig. 34, where as expected the incidence of intraparticle transport on the performance is significant (operation conditions used are reported in Tab. 15 Section 4.3.1). The gap in performance increases with T, because the effectiveness factor of catalyst decrease with T; this is because while D_i, the molecular diffusion coefficient of species i, has a power law dependence on T, the kinetic constant k increases exponentially, making the internal mass transfer limitation more severe. From the profiles of η along the bed, it's clear that an average effectiveness factor could be used for each case, thus reducing noticeably the computational effort.

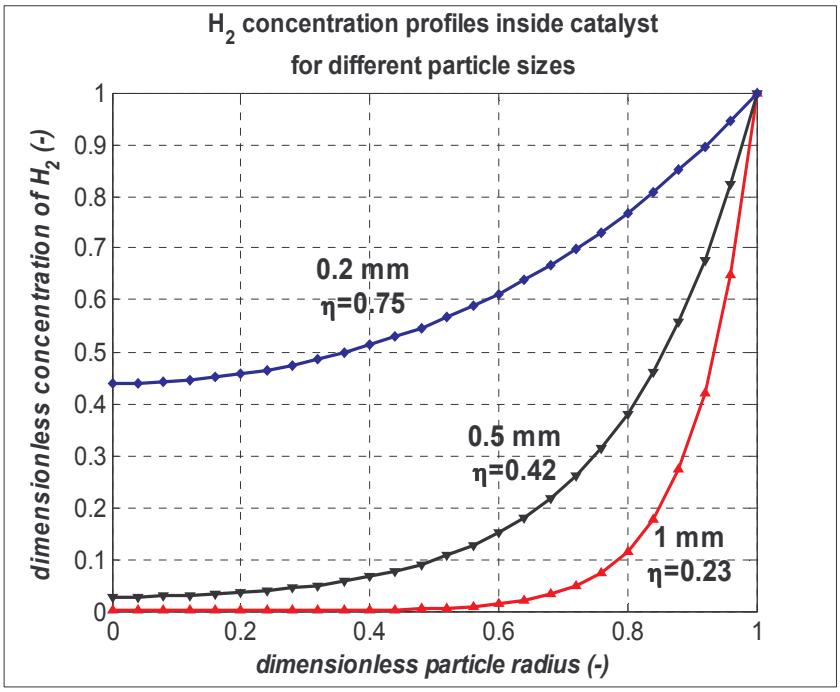

Fig. 33. Concentration profiles of H_2 inside the catalytic particles for different particle sizes.

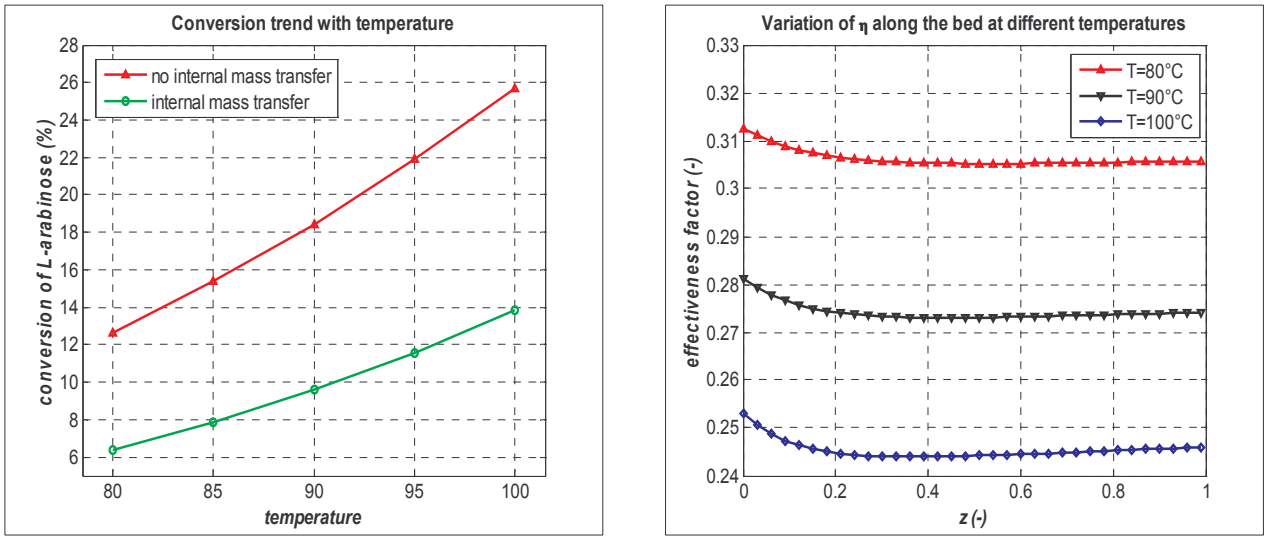

Fig. 34. a) Trend of the sugar conversion with the temperature and b) values of effectiveness factor along the bed.

In Fig. 35 conversion is plotted against the liquid velocity. The gap in performance tends to enlarge with u_L, but the effectiveness factors calculated do not change appreciably (they are always around 0.20-0.25). Instinctively, we may think that for larger u_L, we should have lower η; in fact, larger u_L boost gas-to-liquid mass transfer, thus increasing H_2 concentration in the liquid phase and so forth inside the catalytic particles. Intrinsic reaction rate is therefore enhanced, obtaining lower η since, as shown in Fig. 33, we are under internal mass transfer control. But at the same time, we have a larger production of L-arabitol at the catalyst surface, as a result of the stronger reaction rate, which competes with H_2 and A for active sites (see kinetic mechanism in Section 4.1), inhibiting in someway the reaction and so limiting the decrease in η. This can somehow explains why η remains practically invariant.

Looking at the concentration profiles of H_2 in the liquid phase in Fig. 35b, we might say that, in presence of the internal mass transfer limitations, increasing u_L the reactor shifts from a regime controlled mainly by G/L mass transfer to a diffusion limited regime, even though both transport steps have an important impact on the overall performance of the reactor.

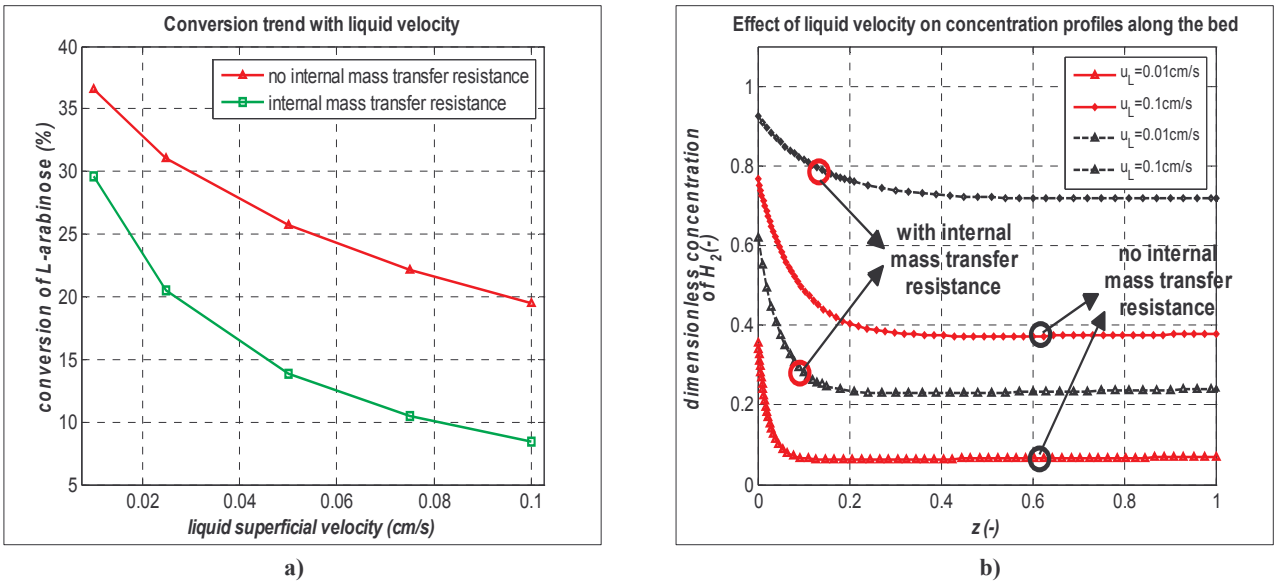

Fig. 35. a) Trend of the sugar conversion with the liquid superficial velocity and b) concentration profiles along the bed for different liquid superficial velocities.

4.4 Isothermal models with L/S mass transfer resistance

We briefly describe the model that takes into account the resistance to the transport of the species from bulk liquid to the liquid at the surface of the catalyst, where production and consumption of species occur; the reactor is always assumed to be isothermal and its characteristics are the same as described previously in Section 4.1. Some results from the sensitivity analysis are presented.

The transport resistance of the species from the bulk liquid to the surface of the catalyst can generate a concentration profile inside the liquid phase; the weaker the transport, the more pronounced the profile. Fig. 36 show how the situation at a certain section of the reactor can be described by means of the film-theory mentioned in Section 2.6 and 2.7.

In this case, the mass balances both on the bulk liquid and at the surface of the solid are solved, and the liquid-solid (L/S) mass transfer term has to be considered in order to supply species from the liquid to the surface of the catalyst. The correlation of Lakota and Levec (1990) was used to predict the L/S mass transfer parameter $k_{LS}a$. We report below the dynamic equations that constitute the 1-D axial dispersion model, listing in order mass balances in bulk liquid and at the surface of catalyst for H_2, then for A and B:

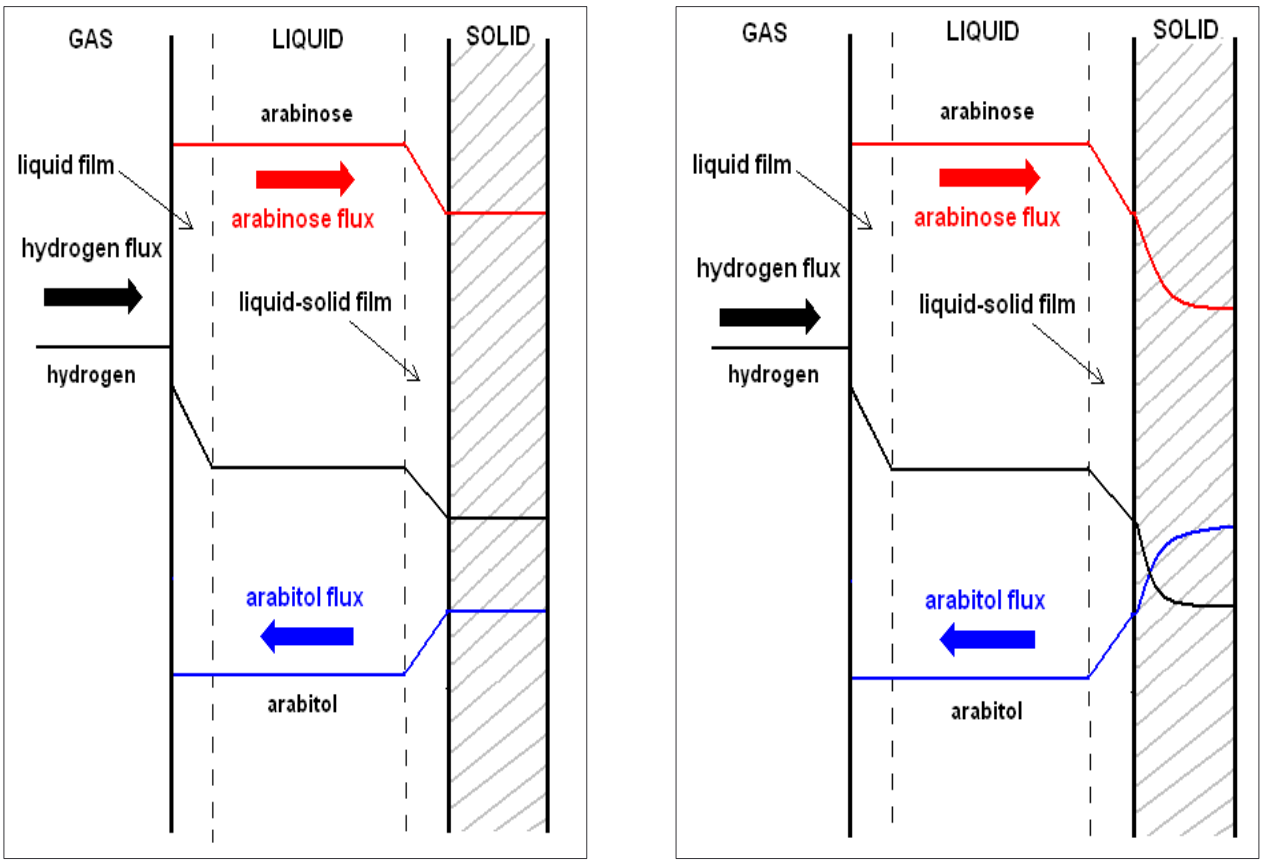

Fig. 36. Concentration profiles in the gas, liquid and solid phase
(a) no intraparticle mass transfer resistance, b) with intraparticle mass transfer resistance).

$$
\begin{aligned}
\varepsilon_L \frac{\partial c_{H_2,L}}{\partial t} &= D_{ax} \frac{\partial^2 c_{H_2,L}}{\partial x^2} - u_L \frac{\partial c_{H_2,L}}{\partial x} + k_{GL} a \left(c_{H_2,L}{}^{*} - c_{H_2,L} \right) - k_{H_2,LS} a \left(c_{H_2,L} - c_{H_2,L} \right) \\
\left(1-\varepsilon_B\right) \frac{\partial c_{H_2,S}}{\partial t} &= k_{H_2,LS} a \left(c_{H_2,L} - c_{H_2,S} \right) - \frac{k K_A K_{H_2} c_{A,S} c_{H_2,S}}{\left(1 + K_{H_2} c_{H_2,S} + K_A c_{A,S} + K_B c_{B,S}\right)^2} \\
\varepsilon_L \frac{\partial c_{A,L}}{\partial t} &= D_{ax} \frac{\partial^2 c_{A,L}}{\partial x^2} - u_L \frac{\partial c_{A,L}}{\partial x} - k_{A,LS} a \left(c_{A,L} - c_{A,S} \right) \\
\left(1-\varepsilon_B\right) \frac{\partial c_{A,S}}{\partial t} &= k_{A,LS} a \left(c_{A,L} - c_{A,S} \right) - \frac{k K_A K_{H_2} c_{A,S} c_{H_2,S}}{\left(1 + K_{H_2} c_{H_2,S} + K_A c_{A,S} + K_B c_{B,S}\right)^2} \\
\varepsilon_L \frac{\partial c_{B,L}}{\partial t} &= D_{ax} \frac{\partial^2 c_{B,L}}{\partial x^2} - u_L \frac{\partial c_{B,L}}{\partial x} - k_{B,LS} a \left(c_{B,L} - c_{B,S} \right) \\
\left(1-\varepsilon_B\right) \frac{\partial c_{B,S}}{\partial t} &= k_{B,LS} a \left(c_{B,L} - c_{B,S} \right) + \frac{k K_A K_{H_2} c_{A,S} c_{H_2,S}}{\left(1 + K_{H_2} c_{H_2,S} + K_A c_{A,S} + K_B c_{B,S}\right)^2}
\end{aligned}
\qquad (126)
$$

with the following boundary conditions:

$$
\begin{aligned}
\frac{\partial c_{i,L}}{\partial x}(0,t) &= \frac{u_L}{D_{ax}} \left(c_{i,L}(0,t) - c_{i,L}{}^{IN} \right) \\
\frac{\partial c_{i,L}}{\partial x}(L_B,t) &= 0
\end{aligned}
\qquad (127)
$$

where the subscript *L* refers to the bulk liquid phase and the *S* to the liquid at the surface of the catalyst.

In Fig. 37 we observe that the conversions achieved considering the L/S transport resistance are lower respect to the case without it, because adding a further transport resistance, the overall reaction rate decreases everywhere in the bed, reducing the overall performance of the reactor. Anyway, the decrease is not significant, meaning that the L/S mass transfer in these conditions is far more effective than the G/L mass transfer, which remains the slowest step.

Fig. 38a reports concentration profiles of H_2 and L-arabinose along the bed at 100°C (other operation conditions are specified in Tab. 15), while Fig. 38b shows more clearly that concentration differences between bulk liquid and liquid at the surface of the catalyst are larger in the first 10-15% of bed length due to stronger intrinsic reaction, for the higher H_2 concentration in the liquid solution. For the rest of the bed, L/S mass transfer and intrinsic reaction are balancing.

The larger concentration difference for H_2 than A that appears in Fig. 38a must not confuse, in fact the former concentration has been divided for $c_{H2,L}^{*}$ while the latter for $c_{A,L}^{IN}$, which is about 25 times larger than $c_{H2,L}^{*}$. Physically, the difference in c_A between bulk liquid and liquid at the surface of catalyst is larger than for c_{H2} (as Fig. 38b shows), because diffusion in the liquid of larger molecules such as sugars is much more difficult than for small molecules as H_2. Comparing diffusion coefficients for H_2 determined from the method of Wilke and Chang and for the sugar arabinose estimated from Noriko et al. (2007), we obtain that the latter is 5 times smaller than the former.

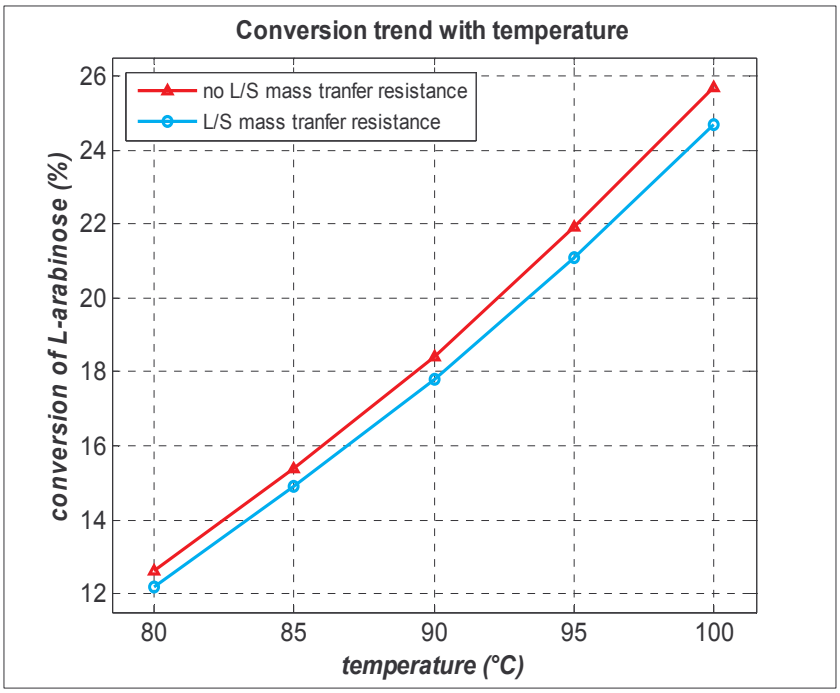

Fig. 37. Trend of the sugar conversion with the temperature for the axial dispersion TBR model.

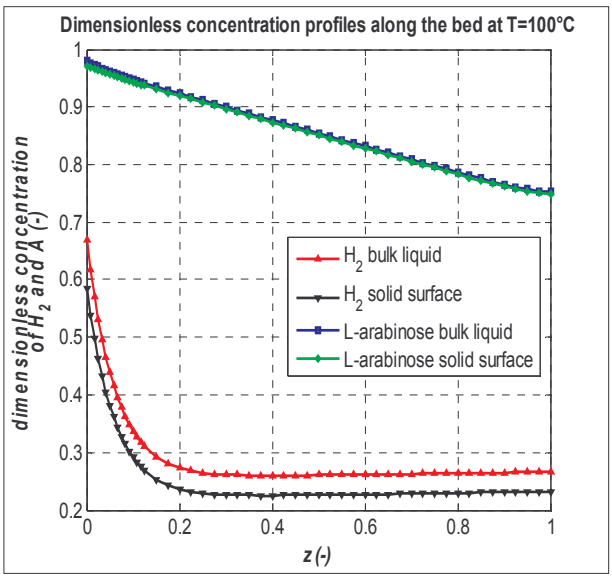

a)

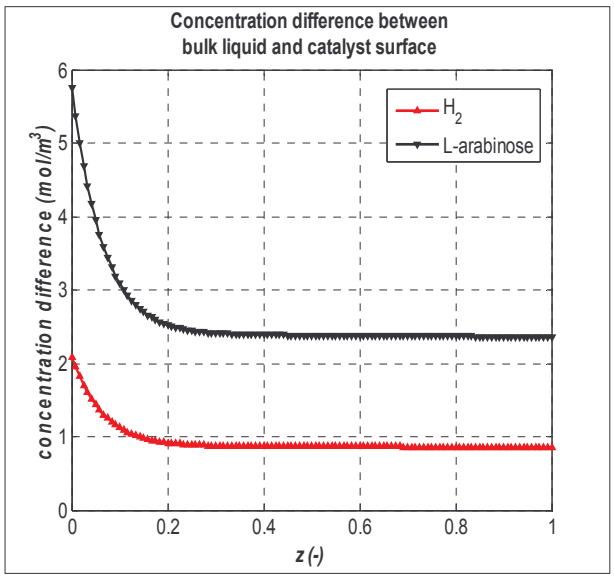

b)

Fig. 38. a) Concentration profiles of H_2 and L-arabinose along the bed at 100°C and b) concentration differences for H_2 and L-arabinose between bulk liquid and liquid at the surface of catalyst.

The trends of L-arabinose conversion with liquid velocity reported in Fig. 39 confirms what we said above, that is the L/S mass transfer resistance is practically negligible for our system in the conditions tested.

We do not report graphical results obtained from the simulation of the heterogeneous TBR model including internal mass transfer resistance for sake of shortness and because the effect of this transport resistance on the reactor performance has already been treated in Section 4.3.2.

From our analysis on the hydrogenation of L-arabinose in a small-scale trickle-bed reactor using as catalyst activated carbon with 0.7%wt ruthenium, we can derive the following conclusions:

- when using catalytic particles of commercial size (equivalent spherical diameter larger than 1mm), in order to get representative kinetics taking into account possible internal mass transfer limitations, the modeling of the trickle-bed reactor must consider both the gas-to-liquid mass transfer resistance and the diffusive transport resistance inside catalytic particles. Which of the two transport resistances prevails along the bed depends on the operation conditions, mainly temperature and liquid and gas velocities; L/S mass transfer is not particularly limiting;
- it is better to use a low liquid superficial velocity (less than 0.05 cm/s) in order to ensure an adequate residence time, while to boost the gas-to-liquid mass transfer one can operate

with higher gas velocity (5 cm/s or even more), since there's no risk of flooding in the reactor due to the cocurrent configuration; a possible disadvantage from using low u_L, can be the worsening of the hydrodynamics conditions in the bed, but this can be offset by increasing the pressure (up to 50/60 bar) and the u_G;

- wetting of the catalyst is almost always adequate and axial dispersion limited only if the bed is diluted with inert fines, based on criteria reported in literature. Furthermore, this aspect strongly simplifies the modeling of the reactor, making easier to perform a kinetic study; it also makes the hydrodynamics of the small-scale TBR similar to that of a large scale unit;
- if catalyst is crushed to an average size of less than 200 μm, than the internal mass transfer resistance can be neglected, making possible to reach large conversion of L-arabinose with higher liquid velocity; this is a favourable condition also for the hydrodynamics in the bed, and a great simplification from the numerical point of view;
- the pressure drop in the bed is always less than 1% of the total incoming pressure (for the conditions tested) and the molar rate of H_2 which absorbs is about 0.1% of the total incoming molar rate of gaseous H_2, thus pressure in the reactor can be reasonably assumed uniform.

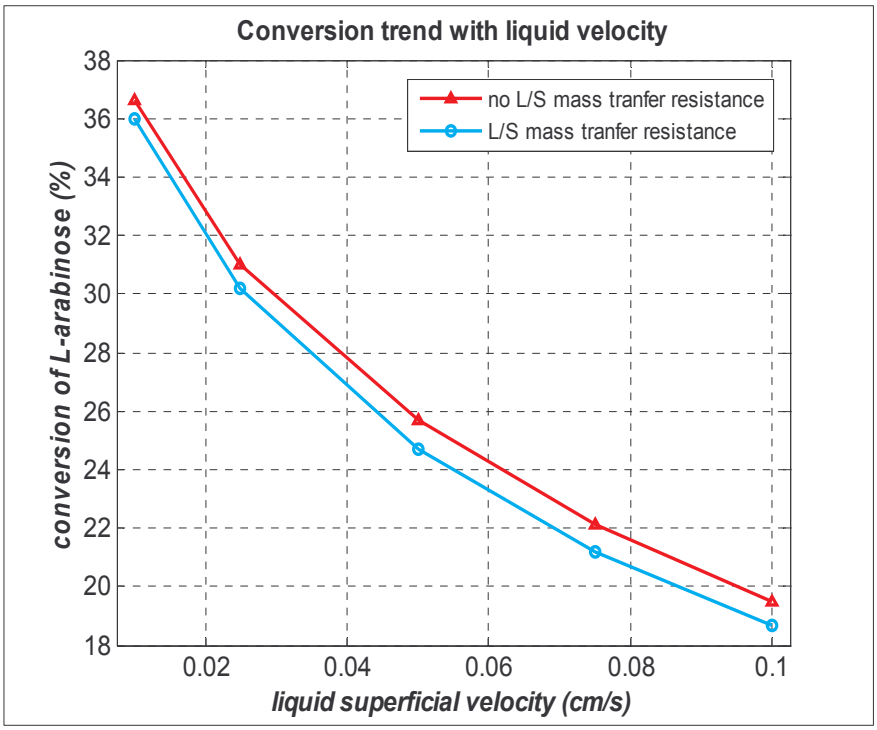

Fig. 39. Trend of the sugar conversion with the liquid superficial velocity for the axial dispersion TBR model.

4.5 Modeling of TBR with deactivating catalyst and comparison with experimental data

The stability, together with the activity and the selectivity, is one of the three main aspects of concern when preparing and using a catalyst. For "stability" we mean the ability of the catalyst to maintain its initial activity and selectivity in the time; the time scale of deactivation can vary significantly depending on the process in which the catalyst is involved. Tab. 20, adapted from Moulijn et al. (2001), gives us an idea of the variety of deactivation time scale in catalytic industrial processes. As we see, the time scale of the deactivation has strong influence on the design of the process unit and on its operation modes.
The five main causes of deactivation (Moulijn et al., 2001; Murzin and Salmi, 2005) are poisoning, fouling, sintering (thermal degradation), mechanical damage and corrosion or leaching by reaction mixture. Each of these phenomena is represented schematically in Fig. 40 (Moulijn et al., 2001).

Tab. 20. Time scale of deactivation in heterogeneous catalytic processes (adapted from Moulijn et al., 2001).

Process	Catalyst	Main deactivation mechanism	Time scale of deactivation	Regeneration	Consequences for process
FCC	Zeolite	Coke	Seconds	Coke combustion	Recirculation of catalyst between reactor and regenerator
Catalytic reforming	Pt/Al_2O_3-γ	Coke	Months	Coke combustion	Fixed bed – swing operation or moving bed
Hydrotreating	$Co/Mo/S/Al_2O_3$	Coke Metal sulfides	Months Days	Coke combustion	TBR, 3phase fluidized bed reactor, slurry
Water gas shift	$Cu/ZnO/Al_2O_3$	Poisoning (S, Cl)	Years	/	Feed purification
Steam reforming	Ni/Al_2O_3	Coke	/	Combustion	Excess steam

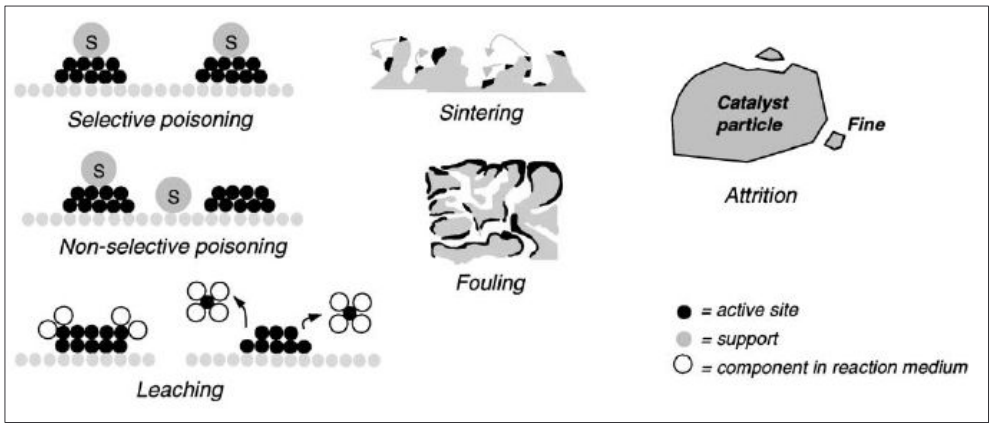

Fig. 40. Different types of catalyst deactivation (Moulijn et al., 2001).

The first approach to include the catalyst deactivation in the reactor model is to use a mechanistic model of deactivation, as outlined by Murzin and Salmi (2005). To obtain mathematical expressions for deactivation, we simply consider deactivation reactions as part of the whole reaction network; we thus consider the reaction mechanism proposed by Sifontes et al. (2010) and add a parallel reaction in which the reactant A forms a carbon deposit C* on the active site, that stays adsorbed:

$$\begin{aligned} &H_2 + \sigma \xrightleftharpoons{K_{H_2}} H_2^* \\ &A + \sigma \xrightleftharpoons{K_A} A^* \\ &A^* + H_2^* \xrightarrow{k_1} B^* + \sigma \\ &B^* \xrightleftharpoons{K_B} B + \sigma \\ &A^* \xrightarrow{k_2} C^* \end{aligned} \tag{128}$$

where notation * means "adsorbed" and σ is an active site. Treating this mechanism with the usual hypotheses of the LHHW kinetics, we assume that reactions at the surface (hydrogenation and formation of deposit) are rate determining steps, while adsorption and desorption steps are assumed to be rapid and so at equilibrium; moreover we use the active sites balance at the surface to explicit the fraction of free active sites (see App. B). The final reaction rate expressions for both hydrogenation and formation of the deposit are:

$$\begin{aligned} R_1 &= k_1 \frac{K_A K_{H_2} c_A c_{H_2}}{\left(1 + K_A c_A + K_B c_B + K_{H_2} c_{H_2}\right)^2} \left(1 - \theta_c\right)^2 \\ R_2 &= k_2 \frac{K_A c_A}{1 + K_A c_A + K_B c_B + K_{H_2} c_{H_2}} \left(1 - \theta_c\right) \\ \alpha &= 1 - \theta_c \end{aligned} \tag{129}$$

where R_1 (mol/m^{3}s) is hydrogenation rate, R_2 (mol/m^{3}s) is coking or formation of carbon deposit rate, θ_c (-) is the fraction of active sites occupied by deposit, k_2 (mol/m^{3}s) is the kinetic constant of the reaction of coking and α (-) is the fraction of active sites not occupied by deposit and so available to reaction. The mass balance for the adsorbed C* on the surface will be:

$$\frac{d\theta_c}{dt} = -\frac{d\alpha}{dt} = k_2' \frac{K_A c_A}{1 + K_A c_A + K_B c_B + K_{H_2} c_{H_2}} \left(1 - \theta_c\right) \tag{130}$$

where k_2' (-) is the appropriate kinetic constant in order to match the units of measure of right-hand-side and left-hand-side of the expression. Typical initial conditions for Eq. (130) could be $\alpha(0) = 1$, i.e. completely active catalyst.

This equation tells us how the fraction of available sites varies with time-on-stream; the effect of the catalyst deactivation due to the deposition of C is taken into account via the reduction of α in the time and leads also to a reduction in selectivity. Combining Eq. (130) with reactor dynamic mass balances for A, B and H_2, we are able to include the deactivation mechanism in the reactor model.

A simpler approach is based on the concept of separable kinetics. It is applicable when the real physical reason for the deactivation is unknown, when the deactivation reaction is much slower than the main reaction rate or the deactivation does not affect the selectivity of the reaction system (in the previous approach, A is consumed to produce C^*, therefore the deactivation modifies selectivity).

Assuming that pseudo-steady state conditions prevails in the fluid phase, we can consider the concentrations of reactants and products appearing at the right-hand-side of Eq. (130) as constants, thus it reduces to

$$\frac{d\alpha}{dt} = -k'\alpha \tag{131}$$

Integration with the same initial conditions gives

$$\alpha = \exp(-k't) \tag{132}$$

which is one of the possible empirical expressions to account for the decay of activity α in the time (Murzin and Salmi (2005)); Eq. (132) must then be multiplied with the reaction rate expression in the reactor model. A more general expression, whose derivation we omit and which is an extension of Eq. (132), is:

$$\alpha(t) = \alpha^* + (\alpha_0 - \alpha^*)\exp(-k't) \tag{133}$$

where α_0 (-) is the initial value of the activity function, normally set to 1, α^* (-) is the asymptotic value of activity, i.e. the value of activity when $t \to \infty$, and k' (1/s) the deactivation constant.

Some experiments on the hydrogenation of L-arabinose in a small-scale laboratory TBR has been conducted in the Laboratory of Industrial Chemistry and Reaction Engineering in Åbo Akademi; results showed a strong deactivation of the catalyst, an aspect that required to include the deactivation in the reactor model. A sensitivity study on the effect of α^* and k' was made to investigate the capability of a simple reactor model to represent these trends.

Activated carbon extrudates of cylindrical shape, both of commercial size (length=3 mm – diameter=1 mm) and crushed to a size of about 200μm, with 0.7%wt content of dispersed ruthenium were used as catalysts. Knowing the exact mass of catalyst used (in all experiments was less than 1g), its bulk density (approx. 0.4 g/cm^3) and the diameter of the reactor, it was possible to estimate the length of the active catalyst bed to be used in the simulation. The bed was diluted with silicon carbide inert of 250 microns, to improve the hydrodynamics, i.e. reduce axial dispersion, and improve catalyst wetting.

The initial concentration of L-arabinose was always around 10%wt, so that the correlation of Rivero (2009) for H_2 solubility in the sugar solution could be applied. The concentration of sugar and sugar alcohol with time-on-stream were measured for different operation conditions.

In Tab. 21 operation conditions and characteristic of the catalyst bed used in two of these experiments are reported. The very small size of both catalytic particles and inerts used allowed both criteria for negligible axial dispersion and adequate wetting of the catalyst to be fulfilled.

Tab. 21. Operation conditions and bed characteristics for two experimental sets (a) experimental set 1, b) experimental set 2).

a)

Operation conditions and bed characteristics	Values
T (°C)	130
p (bar)	20
u_L (cm/s)	0.026
u_G (cm/s)	4.2
m_{cat} (g)	0.98
d_P (mm)	≥0.18
d_R (mm)	10
approx. L_B (mm)	30

b)

Operation conditions and bed characteristics	Values
T (°C)	130
p (bar)	30
u_L (cm/s)	0.017
u_G (cm/s)	4.2
m_{cat} (g)	0.90
d_P (mm)	$0.125 \leq d_P \leq 0.250$
d_R (mm)	10
approx. L_B (mm)	30

In both cases, both the Fukushima and Kusaka (1977) and Larachi et al. (1993) criterions predict that the reactor was operating in the trickle flow regime, which can be expected for the low values of the liquid superficial velocity used. To calculate the solubility of H_2 in the liquid solution, Henry's law was used in this case, since Eq. (106) is valid in the range of pressure 30 bar $\leq p \leq$ 60 bar; Rivero (2009) proposed values of Henry's constants for this system for three different temperatures, 90°C-110°C-130°C. Henry's law and correspondent value of Henry's constant at 130°C are reported below:

$$c_{H_2,L}{}^{*}\left(\frac{mol}{L}\right)=\frac{p_{H_2}}{H}$$
$$H=1262.056\frac{L\cdot atm}{mol} \qquad (134)$$

Extrapolation was unavoidable using Eq. (105) to determine viscosity of the liquid phase at 130°C.

A simple isothermal axial dispersion model with effective liquid-to-solid and internal mass transfer was used to describe the TBR; we roughly assess its capability to represent experimental trends obtained with crushed catalyst, the only sets in which temperature was kept constant. We chose this model based on the fact that L/S mass transfer was predicted not to be a limiting step of the overall reaction rate from the simulations reported in Section 4.4, and the mass transfer resistance inside crushed catalyst has been shown to be negligible in Section 4.3.2.

The empirical expression (133) for the activity function was used to take into account the catalyst deactivation, that was evident in the experimental data. The objective function studied in the sensitivity to find the best range of deactivation parameters k' and α^* to describe the experimental trends was defined as the sum of squared residuals between experimental and calculated conversion of arabinose. The gas-to-liquid mass transfer coefficients were predicted from the correlation of Ellman (1988), but then adjusted to obtain a better prediction of the experimental trends. It resulted that suitable values of k_La were between 40%-60% of k_La predicted from Ellman (1988).

Fig. 41a shows a contour plot of the objective function against the asymptotic activity α^* and the deactivation constant k'; it shows the existence a minimum and the high sensitivity of the model to variation in k' and α^*. By using values of k' and α^* that minimize the objective function, $1.2 \cdot 10^{-3} s^{-1}$ and 0.03 respectively, the fitting obtained is rather acceptable, as reported in Fig. 42. We note that the asymptotic activity is almost zero, which confirms the strong deactivation occurring.

Clearly, to make a thorough validation of the model, a more complete set of experimental data is needed, together with experimental data for the determination of G/L mass transfer coefficient on this small-scale TBR, whose predictions from correlations has been proved to be problematic.

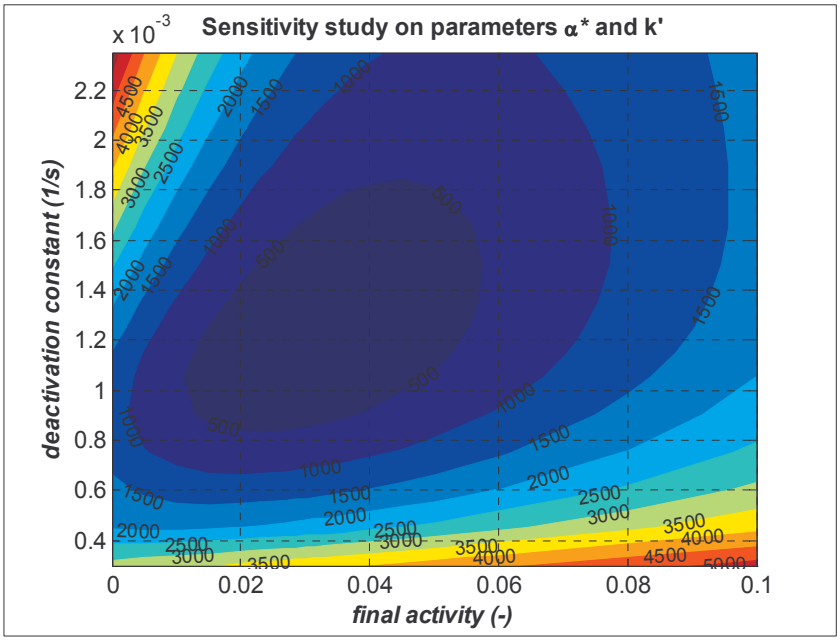

a)

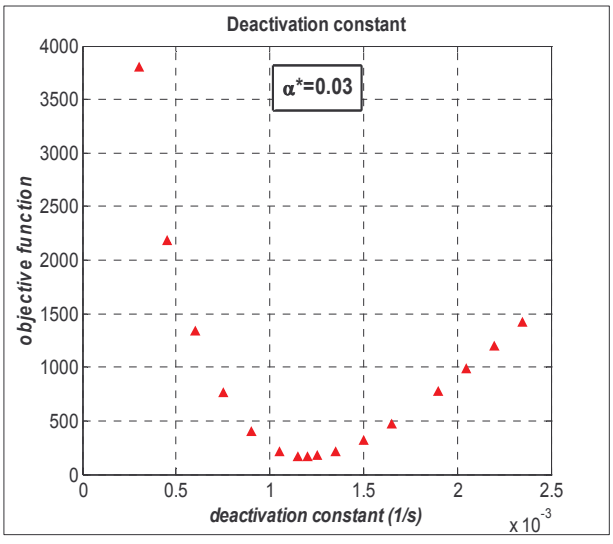

b)

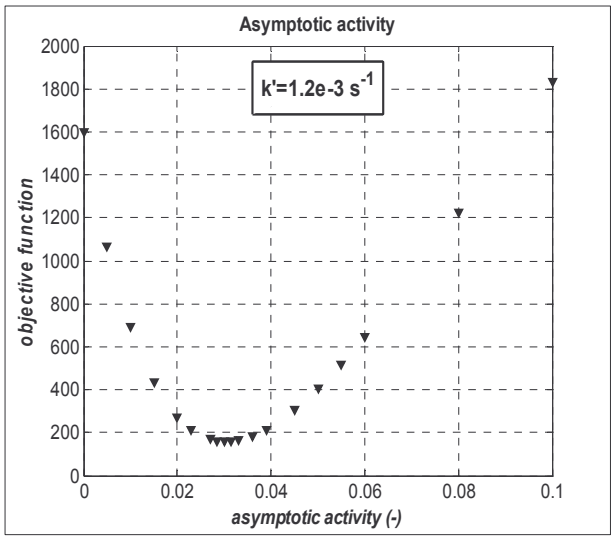

c)

Fig. 41. a) Contour plot of the objective function, b) objective function against deactivation constant and c) objective function against asymptotic activity.

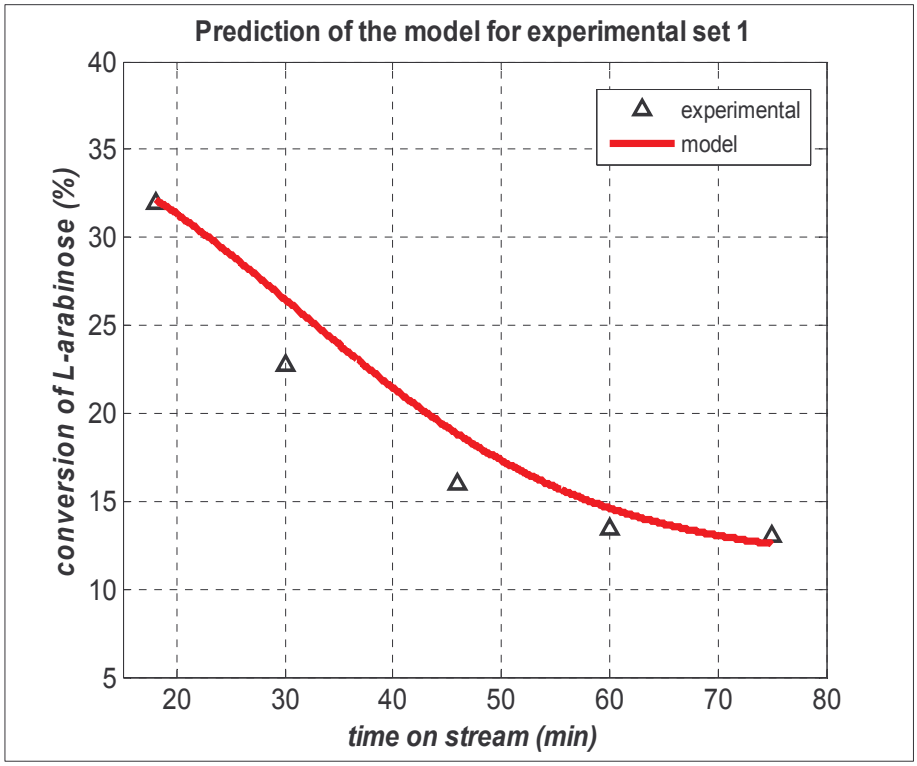

a)

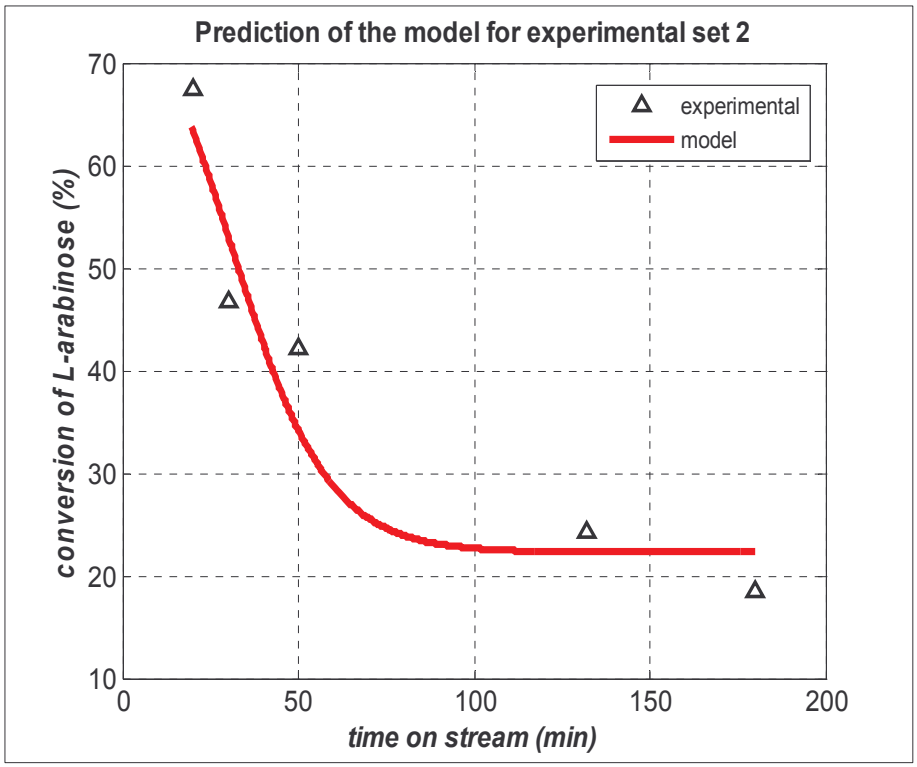

b)

Fig. 42. Model predictions and experimental trends of conversion (a) experimental set 1, b) experimental set 2).

4.6 Adiabatic model with effective L/S and internal mass transfer

Up to now we only considered isothermal models, but a hydrogenation reaction is always exothermic since it leads to thermodynamically more stable products.

To ensure the isothermicity in a small-scale laboratory TBR, Mary et al. (2009) propose three ways, dilution of the bed with small size conducting inert particles, such as silicon carbide, reduce reactor diameter or exchanging heat at the wall, using circulating water or electrical heating. By the way, they also point out that few reliable correlations can be found to estimate heat transfer coefficients and bed conductivity.

To assess the impact of the release of heat by reaction, a simple adiabatic reactor model has been proposed based on the information extracted from literature (Ramachandran and Chaudhari, 1983; Shah and Paraskos, 1975; Toppinen et al., 1996; Cussler, 1997). The following assumptions have been made in the development:

- no mass and heat transfer resistance in the transport of species and heat from the liquid at the surface of catalyst particles to the bulk liquid; this seems quite a reasonable assumption for the particular system considered, where liquid-to-solid transport is not the limiting step;
- the small reactor is assumed to operate adiabatically, therefore no heat transfer is assumed to occur between liquid and reactor wall;
- gas-to-liquid mass and heat transfer steps are considered;
- radial temperature gradients are neglected, i.e. the thermal conductivity of the bed is considered very effective;
- liquid and gas phase are described by means of the axial dispersion model, with high Pe numbers, due to the bed dilution with fines;
- evaporation of the solvent is negligible. As discussed earlier in Section 4.2, the high pressures used for this reaction somehow justify this assumption; however, a more valid proof should be obtained solving the energy balances and studying the increase of temperature obtained;
- complete wetting of the catalyst;
- the Chilton-Colburn analogy was used to estimate the G/L heat transfer coefficient from the G/L one, predicted by the correlation of Ellman (1977). This procedure has been followed also by Toppinen et al. (1996); the Chilton -Colburn analogy is defined as:

$$j_D = j_H$$

$$j_D = \frac{k_{GL}a}{u_L}\left(\frac{\nu_L}{D_L}\right)^{2/3} \qquad (135)$$

$$j_H = \frac{h_{GL}a}{\rho_L c_{P,L} u_L}\left(\frac{\nu_L \rho_L c_{P,L}}{k^T{}_L}\right)^{2/3}$$

where v_L (m^2/s) is the kinematic viscosity, $c_{P,L}$ (J/kg·K) the specific heat of liquid, k^T_L (W/m·K) the thermal conductivity and $h_{GL}a$ (W/m^3K) is the heat transfer coefficient in the gas or liquid phase. We evaluated separately gas-side and liquid-side heat transfer coefficients and compared them, since, as noticed in the work of Roininen et al. (2009), faint gas-side mass transfer resistance does not mean faint heat transfer resistance as well. On the contrary, for our particular system and conditions gas-side heat transfer coefficient h_Ga is always lower than h_La, thus the limiting step in the transport of heat is located in the gas film;

- the specific heat of liquid solution was approximated to that of pure water and calculated from the correlation proposed in Perry and Green (1997), valid for 273K < T < 533K, reported below:

$$c_{P,L}\left(\frac{J}{kmol\cdot K}\right) = C_1 + C_2\cdot T + C_3\cdot T^2 + C_4\cdot T^3 + C_5\cdot T^4$$

$$\begin{cases} C_1 = 2.7637\cdot 10^5 \\ C_2 = -2.0901\cdot 10^3 \\ C_3 = 8.1250 \\ C_4 = -1.411\cdot 10^{-2} \\ C_5 = 9.3701\cdot 10^{-6} \end{cases} \quad (136)$$

- the specific heat at constant pressure for H_2 was calculated from the correlation reported in Perry and Green (1997), valid for 273K < T < 2500K, and with a declared uncertainty of 2%:

$$c_{P,G}\left(\frac{cal}{mol\cdot °C}\right) = 6.62 + 0.00081\cdot T \quad (137)$$

- the thermal conductivity k^T_L of the liquid phase was estimated by means of a polynomial correlation developed based on literature data of k^T_L for water (Incropera et al., 2006; NIST Chemistry WebBook) in the range 273 K ≤ T ≤ 433 K; the fitting was conducted using *MatLab* function *polyfit* and is shown in Fig. 43a. The average percent relative error given by the correlation respect to the literature data is 0.3%:

$$k^T_L\left(\frac{W}{m\cdot K}\right) = a\cdot T^2 + b\cdot T + c$$

$$\begin{cases} a = \text{-}7.496\cdot 10^{-6} \\ b = 6.002\cdot 10^{-3} \\ c = \text{-}5.140\cdot 10^{-1} \end{cases} \quad (138)$$

- thermal conductivity k^T_G of the pure H_2 phase was estimated by means of a polynomial correlation derived based on literature data (NIST Chemistry WebBook) of k^T_G for H_2 for temperatures from 350 K to 450 K and pressure of 25 bar, intermediate between 20 and 30 bar, the two extreme temperatures considered in the experimental sets presented in Section 4.5. Poling et al. (2004) report for low to moderate pressures, that k^T_G increases of 1% for every bar

of increase; for the aim of our calculations, we neglected pressure dependence. Correlation is given below and the average percent relative error is about 0.05%; Fig. 43b reports the fitting results.

$$k^{T}{}_{G}\left(\frac{W}{m\cdot K}\right)=a\cdot T+b$$
$$\begin{cases}a=4.594\cdot 10^{-4}\\ b=5.153\cdot 10^{-2}\end{cases} \tag{139}$$

- the physical properties of both liquid and gas phase H_2, such as density, specific heat and viscosity, were considered uniform along the reactor; while this assumption seems acceptable for the liquid phase, for H_2 a check has been made to assess the sensibility of such properties to temperature. By using the correlation (137) for c_P and tables in NIST Chemistry WebBook for density and viscosity, we obtain that, for variation of about 20°C from an initial temperature of 130°C and pressure of 20 bar, density showed the largest variation, about 5% of the initial value; the assumption is therefore valid also for the gas phase, provided that the increase in temperature along the reactor does not overcome 20°C;
- the adsorption constants in the kinetic rate expression are assumed independent of the temperature;
- standard enthalpy of reaction $\Delta H_R^{\circ 298}$ (J/mol) for hydrogenation of L-arabinose was not found in the literature, therefore we decided to use the correspondent $\Delta H_R^{\circ 298}$ of the hydrogenation of glucose to its sugar alcohol sorbitol, found in Déchamp et al. (1995) ($\Delta H_R^{\circ 298}$=58.5 kJ/mol), since molecule of glucose differs from that of arabinose being an hexose, monosaccharide with six carbon atoms, rather than a pentose, but in both case the group being hydrogenated is an aldehyde functional group; however given the possible uncertainty in $\Delta H_R^{\circ 298}$, the increase in temperature in liquid phase has been determined for values of $\Delta H_R^{\circ 298}$ calculated as -20% and +20% of the reference value.

Mass balances in liquid phase are the same reported in Eq. (110), while energy balances for the gas and liquid phases are:

$$\begin{aligned}&\varepsilon_L\rho_L c_{P,L}\frac{dT_L}{dt}=D_{ax,H,L}\frac{d^2T_L}{dx^2}-\rho_L u_L c_{P,L}\frac{dT_L}{dx}-h_{GL}a\left(T_L-T_G\right)+\ldots\\ &\ldots+\frac{kK_AK_{H_2}c_{A,L}c_{H_2,L}}{\left(1+K_{H_2}c_{H_2,L}+K_Ac_{A,L}+K_Bc_{B,L}\right)^2}\left(-\Delta H_R\right)\\ &\left(\varepsilon_B-\varepsilon_L\right)\rho_G c_{P,G}\frac{dT_G}{dt}=D_{ax,H,G}\frac{d^2T_G}{dx^2}-\rho_G u_G c_{P,G}\frac{dT_G}{dx}+h_{GL}a\left(T_L-T_G\right)\end{aligned} \tag{140}$$

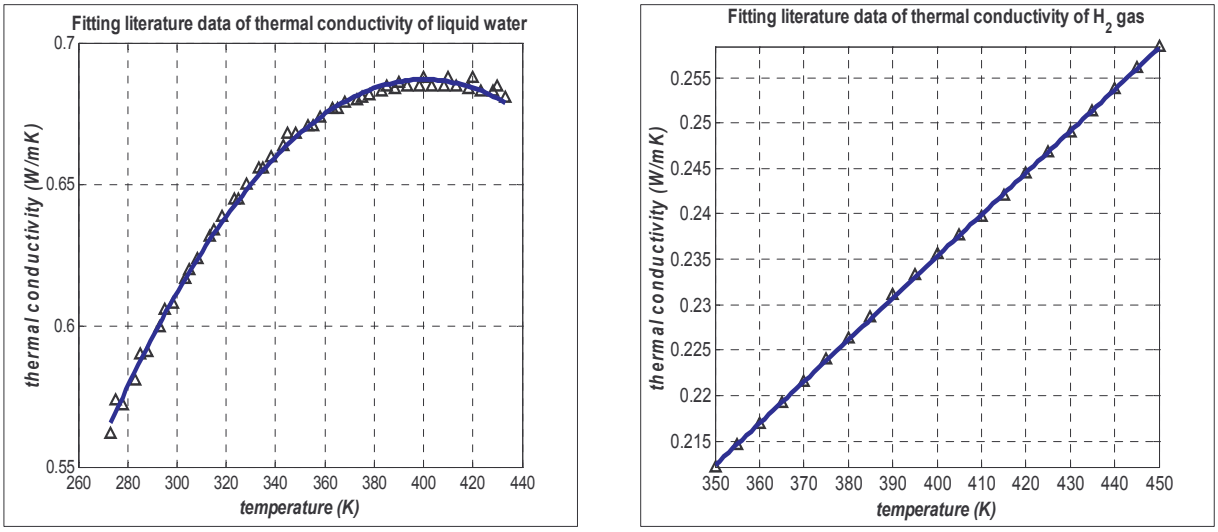

a) b)

Fig. 43. Fitting of literature data on thermal conductivity of liquid water and gaseous H_2.

where $D_{ax,H,L}$ and $D_{ax,H,G}$ (kg·m/s^{3}K) are the axial thermal dispersion coefficients of the liquid and gas phases, which can also be dissociated as $D_{ax,H,L(G)} = \rho_{L(G)} \cdot c_{P,L(G)} \cdot D'_{ax,H,L(G)}$ where $D'_{ax,H}$ has the traditional units of measure of mass dispersion coefficient $D_{ax,L(G)}$ (m^2/s), and ΔH_R (J/mol) is the heat of reaction; the boundary conditions at the inlet and outlet of the reactor are reported only for the liquid-phase energy balance since they are identical:

$$\begin{aligned} &\frac{dT_L}{dx}(0,t) = \frac{u_L}{D'_{ax,H,L}}\left(T_L(0,t) - T_L^{IN}\right) \\ &\frac{dT_L}{dx}(L_B,t) = 0 \end{aligned} \tag{141}$$

where T_L^{IN} (K) is temperature of liquid phase at the reactor entrance. Obviously, since the dependent variables in Eqs. (140) are T_L and T_G (K), kinetic constant k (mol/m^{3}s) has to be explicit through the Arrhenius law.

In Shah and Paraskos (1979), the authors assume $D'_{ax,H,L(G)} = D'_{ax,L(G)}$, based on experimental evidence, thus, if the energy balances in (140) are solved in dimensionless form, $Pe_{H,L(G)} = Pe_{L(G)}$. Moreover, they report that backmixing in the gas phase is usually much lower than in liquid phase, thus a higher Pe_G should be used in the simulations. Trials have shown that for Pe_G higher than 50, results does not change, meaning that we are approaching plug-flow limit; therefore Pe_G has been fixed equal to 50. We also considered valid the assumption of Shah and Paraskos (1979). The liquid-side mass transfer parameter (the dominant one) has been defined as 0.5 x k_La from Ellman (1988), based on what we showed in Section 4.5.

The increase in liquid-phase temperature is lower than 5°C even in the case of the largest value of ΔH_R, as we can see from Fig. 44; therefore, despite the several approximations used in the modeling of the reactor, the results of the simulations are in agreement with the experimental findings, that describe nearly isothermal behaviour. The limited temperature increase is due to the scarcely effective mass transfer (low u_L and u_G and high T) that limits the reaction rate and therefore heat release, to the high specific heat of aqueous solution and to the small mass of catalyst used. The assumption of uniform liquid and gas properties along the bed is fully acceptable in these conditions.

Tab. 22. Operation conditions and parameters used for simulate adiabatic reaction in laboratory TBR.

operation condition / parameter	value
T (°C)	130
p (bar)	20
u_L (cm/s)	0.025
u_G (cm/s)	4
d_P *cat.* (mm)	0.2
d_P *inert* (mm)	0.25
fs (-)	1
ΔH_R (kcal/mol)	-14 +/- 20%
Pe_L (-)	20
Pe_G (-)	50

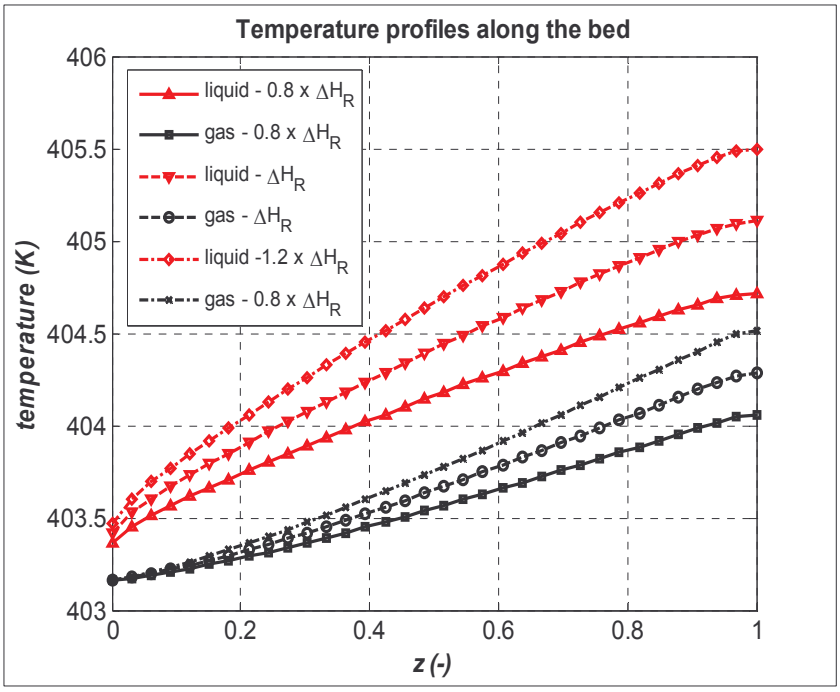

Fig. 44. Temperature profiles in the gas and liquid phases for different estimations of ΔH_R.

Conclusions

A literature review of the principal hydrodynamics and mass transfer parameters for trickle-bed reactors has been carried on; some of the most cited G/L mass transfer coefficient correlations have been tested for our small-scale trickle-bed reactor diluted with inert fines, revealing a large degree of disagreement among predictions. This result could be due to the very low liquid and gas superficial velocities used in this work, which are typical for small-scale trickle-bed reactors. Similar conclusions were also drawn by a recent work of Metaxas and Papayannakos (2006) concerning modelization of laboratory scale trickle-bed reactor for benzene hydrogenation.

Several mathematical models of different complexity describing the behavior of laboratory reactor were developed, particularly focusing on the several mass transfer steps that may considerably limit the performance of such a reactor; gas-to-liquid interfacial mass transfer responsible for the transport of H_2 to the liquid phase, liquid-to-solid and internal mass transfer for catalytic particles of different diameters were included as transport resistances.

The reaction of catalytic hydrogenation of the monosaccharide L-arabinose to its sugar alcohol L-arabitol in aqueous solution using supported Ru/C catalyst was taken as model reaction and the original kinetic expression by Sifontes et al. (2010) was modified in order to have a more proper expression to use in mass and energy balances. Results from the new fitting are satisfactory.

Own codes based on the Numerical Method of Lines were developed to solve numerically the initial boundary values PDE problems arising from dynamical resolution of mass and energy balances. Dynamic resolution make more robust the solution procedure. Algorithms for the solution of boundary value problems and for dynamic grid adaptation were also successfully included, the latters were particularly useful to describe large spatial gradients.

Numerical simulations of the laboratory reactor have been conducted, unveiling the strong gas-to-liquid mass transfer limitations, especially at low liquid velocity and high temperatures. Moreover, using commercial size catalyst strong internal mass transfer

limitations arise as well, with effectiveness factors as low as 0.20 for particles of 1mm diameter; these seem to be the principal limiting steps of the overall reaction rate of hydrogenation in the trickle-bed reactor, while liquid-to-solid mass transfer appears not to affect considerably the reaction. More experimental investigation is needed in order to reach an accurate estimation of the gas-to-liquid mass transfer coefficient.

Experiments led in the Laboratory of Industrial Chemistry and Reaction Engineering on a small-scale trickle-bed reactor with bed diluted with inert fines unveiled a rapid deactivation of the catalyst; this phenomenon was modeled with an empirical model. An attempt of comparison of model predictions and experimental trends was made and results were satisfactory. However, a thorough experimental investigation is necessary to study the mechanism of the deactivation of catalyst, in order to derive a more accurate mechanistic model, to obtain a better characterization of the parameters of the packed bed diluted with fines and to derive more accurate estimations of gas-to-liquid mass transfer coefficient.

A simplified energy balance on the reactor was also solved, making a sensitivity on the ΔH_R since the effective value for L-arabinose hydrogenation was not found in the literature and therefore the one of glucose hydrogenation was taken as reference. Glucose differs from arabinose having one more carbon linked to hydroxyl group, but hydrogenation in both case involves an aldehyde group. Gas-to-liquid heat transfer coefficient was determined from the mass transfer one by means of the Chilton-Colburn analogy. Heat effects are very limited, with temperature increase in liquid phase of less than 5°C; this is due to the low concentration of sugar, high specific heat of solvent water and small mass of catalyst used.

Nomenclature

A	=	preexponential factor, variable units of measure depending on the kinetic expression
a_p	=	external surface of particle per unit volume (1/m)
A_p	=	external surface of particle (m^2)
A_R	=	reactor section (m^2)
c	=	molar concentration (mol/m^3)
c_P	=	specific heat (J/kg·K)
D	=	molecular diffusion coefficient (m^2/s)
D_{ax}	=	axial dispersion coefficient (m^2/s)
D_{eff}	=	effective diffusion coefficient (m^2/s)
d_k	=	Krischer-Kast diameter (m)
dp	=	particle diameter (m)
d_R	=	reactor diameter (m)
Ea	=	activation energy (J/mol)
fs	=	ratio between H_2 concentration in liquid phase and its saturation concentration at the same T and p (-)
g	=	gravitational acceleration (m^2/s)
G	=	gas mass flux ($kg/m^2 \cdot s$)
H	=	Henry's constant (L·atm/mol)
$h_{GL}a$	=	gas-to-liquid heat transfer coefficient (W/m^3K)
k	=	kinetic constant, variable units of measure depending on the kinetic expression
k'	=	deactivation constant of an empirical deactivation model (1/s)
K_i	=	adsorption constant species i (L/mol)
k_Ga	=	gas-side mass transfer coefficient (1/s)
k_La	=	liquid-side mass transfer coefficient (1/s)
$k_{GL}a$	=	gas-to-liquid mass transfer coefficient (1/s)

$k_{LS}a$ = liquid-to-solid mass transfer coefficient (1/s)

k^T = thermal conductivity (W/m·K)

L = liquid mass flux (kg/m^2·s)

L_B = bed length (m)

m_{cat} = mass of catalyst (g)

MW = molecular weight (g/mol)

N_i = diffusive molar flux of species i (mol/m^{2}s)

p = pressure (Pa)

p_c = critical pressure (Pa)

r = radial coordinate (m)

R_G = universal gas constant (J/mol·K)

R_p = particle radius (m)

S_p = particle geometrical surface (m^2)

SV = space velocity (h^{-1})

t = time coordinate (s)

T = temperature (K)

T_c = critical temperature (K)

u = superficial velocity (m/s)

V_p = particle volume (m^3)

w_A = L-arabinose mass fraction (-)

x = axial coordinate (m)

X_A = L-arabinose conversion (%)

Dimensionless numbers

f_{2P} = two-phase friction factor (-)

Ga = Galileo number (-)

Pe = Peclè number (-)

Re = Reynolds number (-)

Sc = Schmidt number (-)

Sh = Sherwood number (-)

W = wetting number (-)

We = Weber number (-)

X_G = modified Lockhart-Martinelli parameter (-)

χ = Lockhart-Martinelli parameter (-)

Φ	=	Thiele modulus (-)

Greek letters

α^*	=	asymptotic activity of a deactivating catalyst (-)
ΔH_R	=	enthalpy of reaction (J/mol)
Δp	=	pressure drop (Pa)
$\Delta p/z$	=	pressure drop per unit length (Pa/m)
Δt	=	time interval (s)
ε_B	=	fixed bed porosity (-)
ε_L	=	total liquid hold up (-)
$\varepsilon_{L,d}$	=	dynamic liquid hold up (-)
ε_p	=	particle internal porosity (-)
η	=	effectiveness factor of catalyst (-)
η_{CE}	=	wetting efficiency of catalyst (-)
θ_i	=	fraction of catalyst active sites occupied by species i (-)
μ	=	dynamic viscosity (Pa·s)
v	=	kinematic viscosity (m^2/s)
ρ	=	mass density (kg/m^3)
σ	=	surface tension (N/m)
τ	=	residence time (s)
τ_p	=	particle tortuosity factor (-)
ϕ_s	=	surface shape factor (-)

Notations

*	=	saturation concentration
°	=	atmospheric pressure
IN	=	inlet
OUT	=	outlet
s	=	liquid at the surface of catalyst

Subscripts

a	=	air
A	=	reactant L-arabinose
B	=	product L-arabitol
cat	=	catalyst
G	=	gas phase
GL	=	gas-to-liquid
L	=	liquid phase
LS	=	liquid-to-solid
s	=	solvent
S	=	solid phase
w	=	water
2P	=	two-phase

References

Al-Dahhan, M.H. and M.P. Dudukovic. *Catalyst bed dilution for improving catalyst wetting in laboratory trickle bed reactors,* AIChE Journal 1996, 42-9, 2594-2606.

Al-Dahhan, M.H. and M.P. Dudukovic. *Catalyst wetting efficiency in trickle bed reactors at high pressure,* Chem. Eng. Science 1995, 50-15, 2377-2389.

Al-Dahhan, M.H., F. Larachi, M.P. Dudukovic and A. Laurent. *High pressure trickle-bed reactors: A review*, Ind. Eng. Chem. Res. 1997, 36, 3292-3314.

Aydin, B. and F. Larachi. *Trickle bed hydrodynamics and flow regime transition at elevated temperature for a Newtonian and a non-Newtonian liquid,* Chem. Eng. Science 2005, 60, 6687-6701.

Cussler, E.L.. *Diffusion, mass transfer in fluid systems,* Cambridge University Press, 1997.

Déchamp, N., A. Gamez, A. Perrard and P. Gallezot. *Kinetics of glucose hydrogenation in a trickle-bed reactor,* Catalysis today 1995, 24-1/2, 29-34.

Dharwadkar, A. and N.D. Sylvester. *Liquid-solid mass transfer in trickle beds,* AIChe Journal 1977, 23-3, 376-378.

Ellman, M.J.. *Characteristiques des reacteurs triphasiques a lit fixe functionnant a cocuorant vers le bas*, Thèse de Doctorat 1988a, INPL, Nancy (F).

Fornberg, B. *Generation of finite difference formulas on arbitrarily spaced grids*, Mathematics of computation 1988, 51-184, 699-706.

Fukushima, S. and K. Kusaka. *Interfacial area and boundary of hydrodynamic flow region in packed column with cocurrent downward flow*, Journal of Chem. Eng. Japan 1977, 10-6, 461-467

Fukushima, S. and K. Kusaka. *Liquid-phase volumetric and mass transfer coefficient and boundary of hydrodynamic flow region in packed column with cocurrent downward flow*, Journal of Chem. Eng. Japan 1977, 10-6, 468-474.

Gianetto, A. and P.L. Silveston. *Multiphase chemical reactors: theory, design, scale-up,* Hemisphere Publishing Corp./ Springer-Verlag 1986.

Gianetto, A. and V. Specchia. *Trickle-bed reactors: state of art and perspectives,* Chem. Eng. Science 1992, 47-13/14,3197-3213.

Goto, S. and J.M. Smith. *Trickle-bed reactor performance. Part I: holdup and mass transfer effects,* AIChe Journal 1975, 21-4, 706-713.

Highfill, W. and M.H. Al-Dahhan. *Liquid-solid mass transfer coefficient in high pressure trickle bed reactors*, Trans IChemE, 2001, 79, Part A.

Holub, R.A., M.P. Dudukovic and P.A. Ramachandran. *A phenomenological model for pressure drop, liquid hold-up and flow regime transition in gas-liquid trickle flow*. Chem. Eng. Science 1992, 47-9, 2343-2348.

Hoyos, B., J.G. Cadavid and H. Rangel.. *Formulation and numeric calculation of non-isothermal effectiveness factor for finite cylindrical catalysts with bidimensional diffusion,* Latin America Applied Research 2004, 34, 17-22.

Iliuta, I., F. Larachi, B.P.A. Grandjean and G. Wild. *Gas-liquid interfacial mass transfer in trickle-bed reactors: state-of-the-art correlations,* Chem. Eng. Science 1999, 54, 5633-5645.

Incropera, F.P., D.P. DeWitt, T.L. Bergman and A.S. Lavine. *Fundamentals of heat and mass transfer – 6th Ed.,* Wiley 2006.

Joubert, R.. *Solid-liquid mass transfer in trickle bed reactors,* Dissertation for Master of Engineering (Chemical Engineering) 2009, Faculty of Engineering, the Build Environment and Information Technology, University of Pretoria.

Lakota, A. and J. Levec. *Solid-liquid mass transfer in packed beds with cocurrent downward two-phase flow,* AIChe Journal 1990, 36-9, 1444-1448.

Lange, R., M. Schubert, W. Dietrich and M. Grünewald. *Unsteady-state operation of trickle-bed reactors,* Chem. Eng. Science 2004, 59, 5355-5361.

Larachi, F., A. Laurent, N. Midoux and G. Wild. *Experimental study of a trickle-bed reactor operating at high pressure: two-phase pressure drop and liquid saturation,* Chem. Eng. Science 1991, 46-5/6, 1233-1246.

Larachi, F., A. Laurent, G. Wild and N. Midoux. *Effect of pressure on the trickle-pulsed transition in irrigated fized bed catalytic reactors,* Can. J. Chem. Eng. 1993, 71, 319.

Larachi, F., M. Cassanello and A. Laurent. *Gas-liquid interfacial mass transfer in trickle-bed reactors at elevated pressures,* Ind. Eng. Chem. Res. 1998, 37, 718-733.

Larkins, R.P., R.R. White and D.W. Jeffrey. *Two-phase concurrent flow in packed beds,* AIChe Journal 1961, 7, 231.

Mahajani, V. and M.M. Sharma. *Effective interfacial area and liquid side mass transfer coefficient in trickle bed reactors*, Chem. Eng. Science 1979, 34, 1425-1428.

Mary, G., J. Chaouki and F. Luck. *Trickle-bed laboratory reactors for kinetic studies,* International Journal of Chemical Reactor Engineering 2009, 7.

Meille, V., de Bellefon, C. And D. Schweich. *Kinetics of α-metilstyrene hydrogenation on Pd/Al2O3*, Ind. Eng. Chem. Res, 2002, 41, 1711-1715.

Metaxas, K.C. and N.G. Papayannakos. *Kinetics and mass transfer of benzene hydrogenation in a trickle-bed reactor*, Ind. Eng. Chem. Res. 2006, 45, 7110-7119.

Metaxas, K.C. and N.G. Papayannakos. *Gas-liquid mass transfer in a bench-scale trickle bed reactor used for benzene hydrogenation,* Chem. Eng. Technology 2008, 31-10, 1410-1417.

Midoux, N., M. Favier and J.C. Charpentier. *Flow pattern, pressure loss and liquid hold-up in gas-liquid downflow packed beds with foaming and non-foaming hydrocarbons,* J. Chem. Eng. Japan 1976, 9, 350..

Missen, R.W., C.A. Mims and B.A. Saville. *Introduction to chemical reaction engineering and kinetics,* John Wiley and Sons, Inc. 1999.

Møller, L. B., C. Halken, J.A. Hansen and J. Bartholdy. *Liquid and gas distribution in trickle-bed reactors,* Ind. Eng. Chem. Res. 1996, 35, 926-930.

Moulijn, J.A., A.E. van Diepen and F. Kapteijn. *Catalyst deactivation: is it predictable? What to do?*, Applied Catalysis A: General 2001, 212, 3-16.

Murzin, D. and T. Salmi. *Catalytic kinetics,* Elsevier 2005.

NIST Chemistry WebBook, *NIST Standard Reference Database Number 69,* 2008.

Perry, R.H. and D.W. Green. *Perry's Chemical Engineers'Handbook – 7th Ed.,* McGraw-Hill 1997.

Poling, B.E., J.M. Prausnitz and J.P. O'Connell.. *The Properties of gases and liquids – 5th Ed.,* McGraw-Hill 2004.

Puranik, S.S. and A. Vogelpohl. *Effective interfacial area in irrigated packed columns.* Chem. Eng. Science 1970, 48, 162.

Rajashekharam, M.V., R. Jaganathan and R.V. Chaudhari. *A trickle-bed reactor model for hydrogenation of 2,4-dinitrotoluene: experimental verification,* Chem. Eng. Science 1998, 53-4, 787-805.

Ramachandran, P.A. and R.V. Chaudhari. *Three-phase catalytic reactors,* Gordon and Breach Science Publishers 1983.

Rao, V.G. and A.A.H. Drinkenburg. *Solid-liquid mass transfer in packed beds with cocurrent gas-liquid downflow,* AIChe Journal 1985, 31-7, 1059-1068.

Rivero Mendoza, D.R.. *Physical properties of sugar solutions and hydrogenation reactions of sugars over Ru/C monolithic catalysts,* Master's Thesis 2009, Faculty of Technology, Åbo Akademi.

Roininen, J., V. Alopaeus, S. Toppinen and J. Aittamaa. *Modeling and simulation of an industrial trickle-bed reactor for benzene hydrogenation: model validation against plant data,* Ind. Eng. Chem. Res. 2009, 48, 1866-1872.

Salmi, T., J.P. Mikkola and J.P. Wärnå. *Chemical reaction engineering and reactor technology,* CRC Press, 2010.

Sastri, S.R. and K.K. Rao: Chem. Eng. J. 1995, 59, 181.

Sato, Y., T. Hirose, F. Takahashi, M. Toda and Y. Hashiguchi. *Pressure loss and liquid hold-up in packed bed reactor with concurrent gas-liquid downflow.* J. Chem. Eng. Japan 1973a, 6, 147.

Schiesser, W.E. *The Numerical Method Of Lines: Integration of Partial Differential Equations,* Academic Press, Inc. 1991.

Shah, Y.T.. *Gas-liquid-solid reactor design,* McGraw-Hill Inc. 1979.

Shah, Y.T. and J.A. Paraskos. *Criteria for axial dispersion effects in adiabatic trickle bed hydroprocessing reactors,* Chem. Eng. Science 1975, 30, 1169-1176.

Sie, S.T.. *Scale effects in Laboratory and Pilot Plant reactors for trickle flow processes,* Rev. Inst. Franc. Du Petrole 1991, 46, 501-515.

Sie, S.T, and R. Krishna. *Process development and scale-up: III. Scale-up and scale-down of trickle bed processes,* Reviews in Chemical Engineering 1998, 14-3, 203-252.

Sifontes, V.A., D. Rivero, J.P. Wärnå, J.P. Mikkola and T. Salmi. *Sugar hydrogenation over supported Ru/C – kinetics and physical properties,* Topics in Catalysis 2010, 53, 1278-1281.

Sifontes, V.A., O. Oladele, K. Kordás, K. Eränen, J.P. Mikkola, D.Y. Murzin and T. Salmi. *Sugar hydrogenation over a Ru/C catalyst,* J. Chem. Technol. Biotechnol. 2011, doi: 10.1002/jctb.2565.

Specchia, V. and G. Baldi. *Pressure drop and liquid holdup for two phase concurrent flow in packed beds,* Chem. Eng. Science 1977, 32, 515-523.

Toppinen, S., J. Aittamaa and T. Salmi. *Interfacial mass transfer in trickle-bed reactor modelling,* Chem. Eng. Science 1996, 51-18, 4335-4345

Turek, F. and R. Lange. *Mass transfer in trickle-bed reactors at low Reynolds number,* Chem. Eng. Science 1981, 36, 569-579.

Turpin, J.L. R.L. Huntington. *Prediction of pressure drop for two-phase, two-component cocurrent flow in packed beds.* AIChE Journal 1967, 13, 1196.

van der Merwe, Werner. *Trickle flow hydrodynamic multiplicity,* Dissertation for degree of Ph.D. of Engineering (Chemical Engineering) 2007, Faculty of Engineering, the Build Environment and Information Technology, University of Pretoria.

van Krevelen, D.W. and J.T.C. Krekels. *Rate of dissolution of solid substances. Part I: physical dissolution*, Rev. Trav. Chim. Pays Bas 1948, 67, 512.

Vande Wouwer, A., P. Saucez and W.E. Schiesser. *Simulation of distributed parameter systems using a MatLab-based Method of Lines Toolbox: Chemical Engineering Applications*, Ind. Eng. Chem. Res. 2004, 43, 3469-3477.

Vande Wouwer, A., P. Saucez, W.E. Schiesser and S. Thompson. *A MatLab implementation of upwind finite differences and adaptive grids in the method of lines,* Journal of Computational and Applied Math. 2005, 183, 245-258.

Wagner, W. and A. Pruss. *The IAPWS formulation 1995 for the thermodynamics properties of ordinary water substance for general and scientific purpose,* J. Phys. Chem. Ref. Data 2002, 31, 2, 387-535.

Wild, G., F. Larachi and J.C. Charpentier. *Heat and mass transfer in gas-liquid-solid fixed bed reactors*, in *Heat and mass transfer in porous media*; Quintard, M. and M. Todorovic, Eds, Elsevier, Amsterdam (NL), 1992, 616.

Yaichi, W., A. Laurent, N. Midoux and J.C. Charpentier. *Determination of gas-side mass transfer coefficients in trickle-bed reactors in the presence of an acqueous or an organic liquid phase*, Int. Chem. Eng. 1988, 28, 299.

Appendix A

Experimental data sets used in kinetic parameters regression

Experimental set 1

t (min)	$c_{arabinose}$ (mol/L)	$c_{arabitol}$ (mol/L)	$c_{hydrogen}$ (mol/L)	T (°C)	p (bar)	$m_{catalyst}$ (g)	V_{liquid} (L)
5	2.43	0.14	0.02	90	40	0.505	0.12
10	2.47	0.21					
20	2.19	0.33					
30	2.17	0.50					
60	1.85	0.81					
90	1.48	1.20					
120	1.18	1.52					
150	0.83	1.87					
180	0.54	2.13					

Experimental set 2

t (min)	$c_{arabinose}$ (mol/L)	$c_{arabitol}$ (mol/L)	$c_{hydrogen}$ (mol/L)	T (°C)	p (bar)	$m_{catalyst}$ (g)	V_{liquid} (L)
5	0.65	0.13	0.03	90	60	0.126	0.12
10	0.68	0.16					
20	0.59	0.25					
30	0.54	0.29					
60	0.40	0.43					
90	0.30	0.54					
120	0.21	0.64					
150	0.12	0.71					
180	0.06	0.78					

Experimental set 3

t (min)	$c_{arabinose}$ (mol/L)	$c_{arabitol}$ (mol/L)	$c_{hydrogen}$ (mol/L)	T (°C)	p (bar)	$m_{catalyst}$ (g)	V_{liquid} (L)
5	0.57	0.12	0.03	130	40	0.100	0.12
10	0.47	0.25					
20	0.27	0.42					
30	0.12	0.60					
60	0.02	0.65					
90	0	0.69					
120	0	0.72					
150	0	0.74					
180	0	0.72					

Experimental set 4

t (min)	$c_{arabinose}$ (mol/L)	$c_{arabitol}$ (mol/L)	$c_{hydrogen}$ (mol/L)	T (°C)	p (bar)	$m_{catalyst}$ (g)	V_{liquid} (L)
5	0.60	0.09	0.05	130	60	0.100	0.12
10	0.46	0.25					
20	0.22	0.48					
30	0.08	0.63					
60	0.01	0.72					
90	0	0.69					
120	0	0.68					
150	0	0.72					
180	0	0.69					

Experimental set 5

t (min)	$c_{arabinose}$ (mol/L)	$c_{arabitol}$ (mol/L)	$c_{hydrogen}$ (mol/L)	T (°C)	p (bar)	$m_{catalyst}$ (g)	V_{liquid} (L)
5	0.60	0.05	0.03	120	40	0.113	0.12
10	0.53	0.17					
20	0.40	0.29					
30	0.25	0.44					
60	0.05	0.61					
90	0	0.69					
120	0	0.70					
150	0	0.70					
180	0	0.71					

Experimental set 6

t (min)	$c_{arabinose}$ (mol/L)	$c_{arabitol}$ (mol/L)	$c_{hydrogen}$ (mol/L)	T (°C)	p (bar)	$m_{catalyst}$ (g)	V_{liquid} (L)
5	0.60	0.06	0.03	105	40	0.112	0.12
10	0.57	0.11					
20	0.48	0.20					
30	0.40	0.28					
60	0.22	0.46					
90	0.09	0.60					
120	0.02	0.64					
150	0	0.69					
180	0	0.68					

Experimental set 7

t (min)	$c_{arabinose}$ (mol/L)	$c_{arabitol}$ (mol/L)	$c_{hydrogen}$ (mol/L)	T (°C)	p (bar)	$m_{catalyst}$ (g)	V_{liquid} (L)
5	0.61	0.08	0.04	120	60	0.113	0.12
10	0.41	0.28					
20	0.22	0.52					
30	0.07	0.67					
60	0.01	0.67					
90	0	0.69					
120	0	0.67					
150	0	0.69					
180	0	0.68					

Experimental set 8

t (min)	$c_{arabinose}$ (mol/L)	$c_{arabitol}$ (mol/L)	$c_{hydrogen}$ (mol/L)	T (°C)	p (bar)	$m_{catalyst}$ (g)	V_{liquid} (L)
5	0.62	0.05	0.03	105	50	0.113	0.12
10	0.55	0.15					
20	0.46	0.25					
30	0.35	0.34					
60	0.16	0.52					
90	0.04	0.66					
120	0.01	0.70					
150	0	0.70					
180	0	0.69					

Experimental set 9

t (min)	$c_{arabinose}$ (mol/L)	$c_{arabitol}$ (mol/L)	$c_{hydrogen}$ (mol/L)	T (°C)	p (bar)	$m_{catalyst}$ (g)	V_{liquid} (L)
5	0.61	0.08	0.04	120	50	0.113	0.12
10	0.46	0.24					
20	0.27	0.41					
30	0.13	0.56					
60	0.01	0.68					
90	0	0.69					
120	0	0.68					
150	0	0.71					
180	0	0.69					

Experimental set 10

t (min)	$c_{arabinose}$ (mol/L)	$c_{arabitol}$ (mol/L)	$c_{hydrogen}$ (mol/L)	T (°C)	p (bar)	$m_{catalyst}$ (g)	V_{liquid} (L)
5	0.61	0.07	0.04	105	60	0.112	0.12
10	0.54	0.15					
20	0.44	0.28					
30	0.36	0.38					
60	0.13	0.55					
90	0.02	0.68					
120	0	0.68					
150	0	0.72					
180	0	0.68					

Experimental set 11

t (min)	$c_{arabinose}$ (mol/L)	$c_{arabitol}$ (mol/L)	$c_{hydrogen}$ (mol/L)	T (°C)	p (bar)	$m_{catalyst}$ (g)	V_{liquid} (L)
5	0.68	0.05	0.03	90	50	0.113	0.12
10	0.66	0.08					
20	0.56	0.15					
30	0.50	0.22					
60	0.34	0.37					
90	0.20	0.48					
120	0.09	0.61					
150	0.03	0.66					
180	0	0.69					

Appendix B

Derivation of reaction rate expressions of hydrogenation and coking

Detailed treatment of the derivation of reaction rate expressions of hydrogenation and formation of carbon deposit.

1) Mechanism:

$$H_2 + \sigma \overset{K_{H_2}}{\rightleftarrows} H_2^* \qquad \left.\begin{array}{l} \\ \\ \\ \\ \end{array}\right\} \text{HYDROGENATION}$$

$$A + \sigma \overset{K_A}{\rightleftarrows} A^*$$

$$A^* + H_2^* \xrightarrow{k} B^* + \sigma$$

$$B^* \overset{K_B}{\rightleftarrows} B + \sigma$$

$$A^* \xrightarrow{k'} C^* \qquad \left.\begin{array}{l} \\ \end{array}\right\} \text{COKING FORMATION}$$

2) Adsorption and desorption steps are treated as they are at equilibrium, thus the fraction of sites occupied by A, B, H_2 and C can be expressed as:

$$\begin{aligned} \theta_{H_2} &= K_{H_2} c_{H_2} \theta_v \\ \theta_A &= K_A c_A \theta_v \\ \theta_B &= K_B c_B \theta_v \end{aligned} \tag{142}$$

3) Reactions at the surface are considered rate determining steps:

$$\begin{aligned} R_1 &= k_1 \theta_A \theta_{H_2} = k_1 K_A K_{H_2} c_A c_{H_2} \theta_v^2 \\ R_2 &= k_2 \theta_A = k_1 K_A c_A \theta_v \end{aligned} \tag{143}$$

4) Balance of active sites is needed to have a 4th equation together with Eqs. (142):

$$\theta_v = 1 - \theta_A - \theta_B - \theta_{H_2} - \theta_C \tag{144}$$

5) Using Eqs. (142) and (144) to explicit θ_v as function of concentrations at the surface c_i and of θ_C, the fraction of active sites occupied by the carbon deposit, and substituting it into Eqs. (143), one gets expressions for reaction rates as functions of concentrations at the surface of the catalyst and of θ_C:

$$R_1 = k_1 \frac{K_A K_{H_2} c_A c_{H_2}}{\left(1 + K_{H_2} c_{H_2} + K_A c_A + K_B c_B\right)^2} \left(1 - \theta_C\right)^2$$
$$R_1 = k_2 \frac{K_A c_A}{1 + K_{H_2} c_{H_2} + K_A c_A + K_B c_B} \left(1 - \theta_C\right) \tag{145}$$